Spring 5-2023

Spectra of Atmospheric and Astronomical Molecules

W. D. Cameron
Old Dominion University, dcameronj@icloud.com

SPECTRA OF ATMOSPHERIC AND ASTRONOMICAL MOLECULES

by

W. D. Cameron
B.S. December 1984, University of Maryland
M.S. May 2000, University of South Alabama
M.S. May 2020, Old Dominion University

A Dissertation Submitted to the Faculty of
Old Dominion University in Partial Fulfillment of the
Requirements for the Degree of

DOCTOR OF PHILOSOPHY

PHYSICS

OLD DOMINION UNIVERSITY
May 2023

Approved by:

Peter Bernath (Director)

Craig Bayse (Member)

Charles Sukenik (Member)

Balša Terzić (Member)

Colm Whelan (Member)

ABSTRACT

SPECTRA OF ATMOSPHERIC AND ASTRONOMICAL MOLECULES

W. D. Cameron
Old Dominion University, 2023
Director: Dr. Peter Bernath

Spectroscopy techniques are focused on spectra of molecules of interest to the Earth's atmosphere and/or astronomy and astrophysics. Laboratory spectroscopy as well as remote satellite sensing are applied. Using the Fourier transform spectrometer aboard the Atmospheric Chemistry Experiment (ACE) satellite to measure the absorption spectra of the Earth's atmosphere through solar occultation limb observation demonstrates that volcanic eruption plumes can be located and tracked through their SO_2 content. The presence of those plumes is corroborated by overlaying infrared atmospheric aerosol extinction observed by the 1 μm imager on the same satellite. Tracking atmospheric aerosol movement with the ACE imager is also shown to provide key insights into the impact of the unique January 2022 Hunga Tonga-Hunga Ha'apai volcanic eruption on Earth's atmosphere. ACE satellite data analysis has also been used to better understand seasonal fractionation patterns of NO_2 and HNO_3 in the stratosphere. Rotational analysis of previously recorded laboratory spectra of the TiO molecule is used to generate new line lists and spectroscopic constants for the $E^3\Pi - X^3\Delta$ and $B^3\Pi - X^3\Delta$ electron transitions as well as the $A^3\Phi - X^3\Delta$ electron transitions of all four minor TiO isotopologues. New laboratory spectra collected using a Fourier transform infrared spectrometer is shown to improve the known infrared cross sections of cyclohexane.

TABLE OF CONTENTS

Chapter Page

Chapter Page

LIST OF TABLES

Table Page

LIST OF FIGURES

Figure Page

Figure Page

Figure Page

CHAPTER 1

INTRODUCTION

Spectroscopy is the study of the interaction of light and matter [1]. Matter can abosorb photons from light and achieve a higher energy state, leaving a tell tale measurable loss of light passing through the matter at the specific wavelength at which the photons are absorbed, which is the basis of absorption spectroscopy. Matter in an excited state can transition to a lower energy state by emitting photons, also at a measurable wavelength, which is the basis of emission spectroscopy. There are basically four ways a molecule can change its energy level through interaction with light: it can change its translational energy, rotational energy, vibrational energy, and/or electrons can change orbitals. In general, the absorbed or emitted photons from rotational transitions are in the microwave region, vibrational transitions are in the infrared region and electron transitions are in the visible/ultraviolet region.

Each atom, molecule and aerosol has a unique spectrum based on its chemical composition. A substance's spectrum can often be determined in the laboratory under controlled conditions, and once it is known the spectrum becomes a powerful reference tool of exploration. Spectroscopy can remotely detect the presence and abundance of a substance, and can be used to determine ambient thermodynamic properties such as pressure and temperature. A frequency shift in an otherwise known spectrum reveals velocity by Doppler shift. This dissertation focuses on remote observations of the Earth's atmosphere as well as research to enhance remote observations of celestial objects such as stars, exoplanets and nebulae.

All species on Earth are dependent on the climate for survival. Few issues regarding the Earth's atmosphere currently garner as much attention as climate change. Central to attempts to understand climate change are climate models. These models are dependent upon knowing the three dimensional location and abundance of all the various molecules that comprise the atmosphere and how they change over time. The warming properties of atmospheric CO_2 typically make it the center of attention. This dissertation will highlight stratospheric SO_2, which makes sulfate aerososols that have a cooling effect on the Earth's surface. The essential data for climate models is often obtained from spectroscopic analysis; much of it is done by satellite remote sensing. Prior to the focus on climate change, there was much public concern regarding the damage being done to the Earth's critical stratospheric

ozone layer. The ozone layer protects the surface of the earth by absorbing harmful ultraviolet rays from the Sun; an advantageous feature regarding the spectrum of ozone. Multiple satellites were launched into orbit whose primary mission was to monitor the ozone layer through remote sensing spectroscopy. The flexibility of molecular spectroscopy has enabled those same satellites, to include the Atmospheric Chemistry Experiment (ACE) satellite, which is central to this paper, to be used in new ways and study aspects of the Earth's atmosphere beyond the scope of the original mission of the spacecraft.

Molecular spectroscopy has long been a key component of astronomy and astrophysics. In 1907 Fowler [2] noted the spectral lines of TiO, the primary molecular spectrum studied in this paper, in Antarian stars (meaning stars like Antares, which is an M-class star). The Morgan Keenan (MK) classification system [3] for stars uses the spectrum of molecules such as TiO to define its various letter designated classes (O, B, A, F, G, K, M). As astronomy and astrophysics have delved into the exploration of exoplanets molecular spectroscopy remains essential. Nugroho et al. [4] have shown that TiO in the atmospheres of hot Jupiter exoplanets can cause the formation of stratospheres. TiO is used as an example not only because it is one of the molecules highlighted in this paper, but to show that despite its spectrum being used in astronomy for over 100 years, there is still room for improvement in its spectral data.

In order to advance atmospheric study, astronomy and astrophysics through molecular spectroscopy, progress begins with laboratory spectroscopy and spectral analysis. These efforts ultimately result in published spectroscopic data and line lists to be used as ready references for exploration.

This research encompasses the use of remote satellite sensing spectroscopy to study the Earth's atmosphere, the analysis of existing laboratory spectroscopic spectra to advance astronomy and astrophysics and new laboratory spectroscopy to improve the existing body of knowledge.

CHAPTER 2

MOLECULAR SPECTROSCOPY

2.1 OVERVIEW

This chapter presents a discussion of aspects of molecular spectroscopy pertinent to analysis and findings to follow. The source of the discussion is Bernath's *Spectra of Atoms and Molecules* [1] unless otherwise cited. The spectrum of a molecule is obtained by measuring the frequency and intensity of photons absorbed, causing a transition to a higher energy state, or measuring the frequency and intensity of photons emitted by a substance as it transitions to a lower energy state. In a traditional graphic depiction of a spectrum, frequency or wavelength is along the x-axis, and intensity is on the y-axis. The frequency is a measure of the the change in energy associated with the transition, the intensity is a measure of how many photons at that frequency were absorbed or emitted. While individual features are referred to as lines, if viewed with high enough resolution, the lines actually have width and shape, referred to as lineshape, brought about by factors such as pressure and temperature. Frequency and wavelength are often seen in spectroscopy with SI units; also commonly used in infrared (IR) spectroscopy is the wavenumber, a measure of the reciprocal wavelength, in cm^{-1}.

The energy of a photon is well known to be

$$E = h\nu = \frac{hc}{\lambda}, \tag{1}$$

where h is Planck's constant, ν is frequency, c is the speed of light in a vacuum and λ is wavelength. The energy state of a system is increased by the absorption of a photon. If the energy increases from E_0 to E_1, then $E_1 - E_0 = h\nu_{10}$ where ν_{10} is the frequency at which the spectral line appears. It is the convention in spectroscopic variables and subscripts to show the lower energy state second. There are two ways the energy state of a system is decreased, collisions and the emission of photons. There are two ways photons can be emitted: spontaneous emission and stimulated emission. Both result in the emission of a photon. Spontaneous emission is essentially the opposite of absorption. In stimulated emission a photon is absorbed resulting in the release of two photons. In both types of

emission the net result is the emission of one photon, and the energy change remains $E_1 - E_0 = h\nu_{10}$.

The intensity of a line is a measure of how many photons are released per unit time, which requires a discussion of Einstein A and B coefficients. The shape of a line is driven by factors other than energy levels, and requires a discussion of lineshape functions. Those two topics are discussed in the following two sections.

2.2 EINSTEIN COEFFICIENTS

From the study of theoretical blackbody radiation comes the concept of a blackbody emitter having a radiation density ρ in units of energy/vol, distributed over a range of frequencies such that

$$\rho = \int_0^\infty \rho_\nu d\nu, \tag{2}$$

where ν is frequency and ρ_ν is the Planck function:

$$\rho_\nu(T) = \frac{8\pi h\nu^3}{c^3} \frac{1}{e^{h\nu/kT} - 1}, \tag{3}$$

where T is temperature and k is the Boltzmann constant.

Returning to the two levels from the Overview with energy E_0 and E_1 and adding that the number of individual systems (atoms, molecules, particles, etc.) at each energy level are N_0 and N_1 respectively, given that the two levels are at thermal equilibrium and non-degenerate, they are subject to the Boltzmann expression:

$$\frac{N_1}{N_0} = e^{-h\nu_{10}/kT}. \tag{4}$$

We define the Einstein absorption coefficient, otherwise known as the Einstein B coefficient, as the rate constant $B_{1\leftarrow 0}$ in the expression regarding the transition from the ground state E_0 to the excited state E_1:

$$\frac{dN_1}{dt} = B_{1\leftarrow 0}\rho_\nu(\nu_{10})N_0. \tag{5}$$

A different Einstein B coefficient is used in the expression describing the transition by stimulated emission from the excited state to the ground state:

$$\frac{dN_1}{dt} = -B_{1\rightarrow 0}\rho_\nu(\nu_{10})N_1. \tag{6}$$

Note the arrow in equation (6) has flipped direction to indicate a transition from the excited state to the ground state; $B_{1\rightarrow 0}$ is the stimulated emission coefficient. Any confusion between the two will be dispelled in short order as they will be shown to be equal.

For spontaneous emission the Einstein A coefficient is used:

$$\frac{dN_1}{dt} = -A_{1\to 0}N_1. \tag{7}$$

Recall it was stipulated that the entire system is at equilibrium. Therefore the rate of depopulation of the excited state must be the same as the population rate. Gathering equations (5), (6) and (7):

$$B_{1\leftarrow 0}\rho_\nu(\nu_{10})N_0 = B_{1\to 0}\rho_\nu(\nu_{10})N_1 + A_{1\to 0}N_1, \tag{8}$$

solving for $\frac{N_1}{N_0}$:

$$\frac{N_1}{N_0} = \frac{B_{1\leftarrow 0}\rho_\nu(\nu_{10})}{B_{1\to 0}\rho_\nu(\nu_{10}) + A_{1\to 0}}, \tag{9}$$

applying the Boltzmann expression, equation (4):

$$e^{-h\nu_{10}/kT} = \frac{B_{1\leftarrow 0}\rho_\nu(\nu_{10})}{B_{1\to 0}\rho_\nu(\nu_{10}) + A_{1\to 0}}, \tag{10}$$

solving for $\rho_\nu(\nu_{10})$:

$$\rho_\nu(\nu_{10}) = \frac{A_{1\to 0}}{B_{1\leftarrow 0}e^{-h\nu_{10}/kT-} - B_{1\to 0}}, \tag{11}$$

and finally substituting in the expression for the Planck function (equation 3):

$$\frac{8\pi h\nu_{10}^3}{c^3}\frac{1}{e^{h\nu/kT}-1} = \frac{A_{1\to 0}}{B_{1\leftarrow 0}e^{-h\nu_{10}/kT-} - B_{1\to 0}}. \tag{12}$$

From equation (12) it can be seen that:

$$B_{1\leftarrow 0} = B_{1\to 0}, \tag{13}$$

and:

$$A_{1\to 0} = \frac{8\pi h\nu_{10}^3}{c^3}B_{1\leftarrow 0}. \tag{14}$$

So the absorption coefficient for absorption and stimulated emission are equal, and they are linked to the coefficient for spontaneous emission by a function in which the frequency that characterizes the difference between the two energy levels is the only variable.

2.3 TRANSITION DIPOLE MOMENTS

There are other methods to analyze the transition between energy levels. The system being discussed with two energy levels, for the purposes of this work, is a molecule composed

of nuclei and electrons, each with position $\overrightarrow{r_i}$ and charge q_i. The system has a total dipole moment:

$$\vec{\mu} = \sum q_i \vec{r}_i. \tag{15}$$

The radiation acting on the molecules is an electromagnetic wave:

$$\vec{E}(r,t) = \vec{E}_0 \cos(\vec{k} \cdot \vec{r} - \omega t). \tag{16}$$

The effect of the radiation acting on the system and the resultant transition probability can be modeled with perturbation theory and the time dependent Schrödinger equation:

$$i\hbar \frac{\partial \Psi}{\partial t} = (\hat{H} + \hat{H}')\Psi, \tag{17}$$

where

$$\hat{H}'(t) = -\vec{\mu} \cdot \vec{E}. \tag{18}$$

With no perturbation the general form of the time dependent solutions is the familiar

$$\Psi_0(t) = \psi_0 e^{-i\omega_0 t},$$

$$\Psi_1(t) = \psi_1 e^{-i\omega_1 t}.$$

Solving the equation is lengthy and leads into directions beyond the focus of this work. A key term that arises in that analysis is $\langle \psi_0 | \mu | \psi_1 \rangle$, a quantity in molecular spectroscopy known as the transition dipole moment, sometimes shown as M_{01} and sometimes shown as μ_{01}. Chackerian et al. (1992) [5] states "The important quantity for evaluation of the absolute line intensities is the squared matrix of the electric dipole moment function..." Bernath [1] shows this by defining the atomic line strength as $S_{J'J''}$:

$$S_{J'J''} \equiv \sum_{M'} \sum_{M''} |\langle J'M' | \vec{\mu} | J''M'' \rangle|^2, \tag{19}$$

where J is the total angular momentum quantum number $\hat{J} = \hat{L} + \hat{S}$, L is angular momentum, S is spin, M is the state of J; the capital letters indicate multiple electrons. The double prime indicates the lower state, the single prime indicates the upper state.

The discussion of transitions between energy states in this section indicate a relationship between the Einstein coefficients and the transition dipole moment must exist. That relationship is also given by Bernath [1]:

$$A_{J' \to J''} = \frac{16\pi^3 \nu^3 S_{J'J''}}{3\epsilon_0 h c^3 (2J'+1)}, \tag{20}$$

where ϵ_0 is the permittivity of free space.

There is an additional quantity somewhat similar to line strength known as oscillator strength, f, of an energy transition. Oscillator strength $f_{J' \leftarrow J''}$ compares the transition to the radiation emitted by an oscillating electron [1]:

$$f_{J' \leftarrow J''} = \frac{8\pi^2 m_e \nu}{3he^2} \frac{S_{J'J''}}{2J''+1}, \tag{21}$$

where m_e is the electron mass and e is the elementary charge. The oscillator strength is sometimes used by astronomers, and given that much of the work presented here supports astronomy, the data tables given as results of research that have the potential to be used by astronomers include it.

2.4 LINESHAPE

The spectrum of a molecule is made of many individual energy transitions, each one a line in the spectrum. These energy transitions can be composed of a combination of changes in electron orbitals, changes in the rotation J quantum number and/or changes in the vibration v number. Each individual transition is referred to as a line, and at a sufficiently coarse resolution they appear to be lines. Zooming in to higher resolution reveals each line to have shape, generally broader at the bottom and coming to a rounded peak at the top.

All lineshape functions result in a broadened line, meaning the line now has width. A useful measurement for spectroscopy is the full width at half maximum (FWHM), also shown in equations as $\Delta\nu_{1/2}$ when using frequencies and $\Delta\tilde{\nu}_{1/2}$ when using wavenumbers. As the name implies, FWHM is the line width at one half the maximum value of the line. See Figure 1. There are two basic types of lineshape functions, homogeneous and inhomogeneous. Homogenous lineshape functions are those in which every molecule in the system has the same lineshape. Inhomogeneous lineshape functions are those in which individual molecules may experience a different environment resulting in differing absorption spectra between molecules. Homogeneous lineshapes are Lorentzian; inhomogeneous lineshape functions are Gaussian. See Figure 2. Pressure broadening is the prime example of homogenious lineshape functions. Doppler broadening is the prime example of inhomogeneous lineshape functions. Both are discussed below as well as other types of broadening. Regardless of whether the lineshape function is Lorentzian or Gaussian, its symbol in equations is typically $g(\nu - \nu_{10})$.

Natural lifetime broadening or natural line width is brought about by spontaneous emission from the upper energy state, the rate of which is given by the Einstein A coefficient. The lifetime Δt of the upper state ends with spontaneous emission, $\tau_{sp} = \frac{1}{A}$. The resultant lineshape is Lorentzian in nature. The time-energy version of the Heisenberg uncertainty principle, $\Delta E \Delta t \geq \hbar$, setting $\Delta t = \tau_{sp}$ drives the FWHM estimate for natural lifetime broadening [7]:

$$\Delta\nu \approx \frac{1}{2\pi\tau_{sp}}. \tag{22}$$

Pressure or collision broadening, caused by collisions of molecules, is the major influence when studying gas under pressure in the microwave region. Van Vleck and Weisskopf [8] developed a term for pressure broadening, $\Delta\nu = \frac{1}{2\pi\tau}$ where τ is the time between collisions. The time between collisions is inversely proportional to pressure, making use of that information, a more useful term for estimating FWHM is provided by Bernath [1]:

$$\Delta\nu_{1/2} = bp, \tag{23}$$

where p is the pressure and b is the pressure broadening coefficient. The pressure broadening coefficient can be estimated for experimental purposes to be about 10 MHz per Torr.

Doppler broadening is caused by molecules having velocity relative to the device measuring the frequency at which the molecules emit radiation, resulting in a Doppler shift of the measured frequency. It is a Gaussian lineshape function, inhomogeneous due to molecules having various velocities. A Maxwell-Boltzmann distribution is used to model the velocity

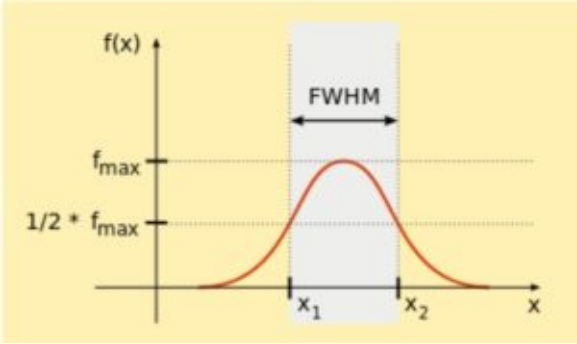

FIG. 1: Full width at half maximum (FWHM) [6].

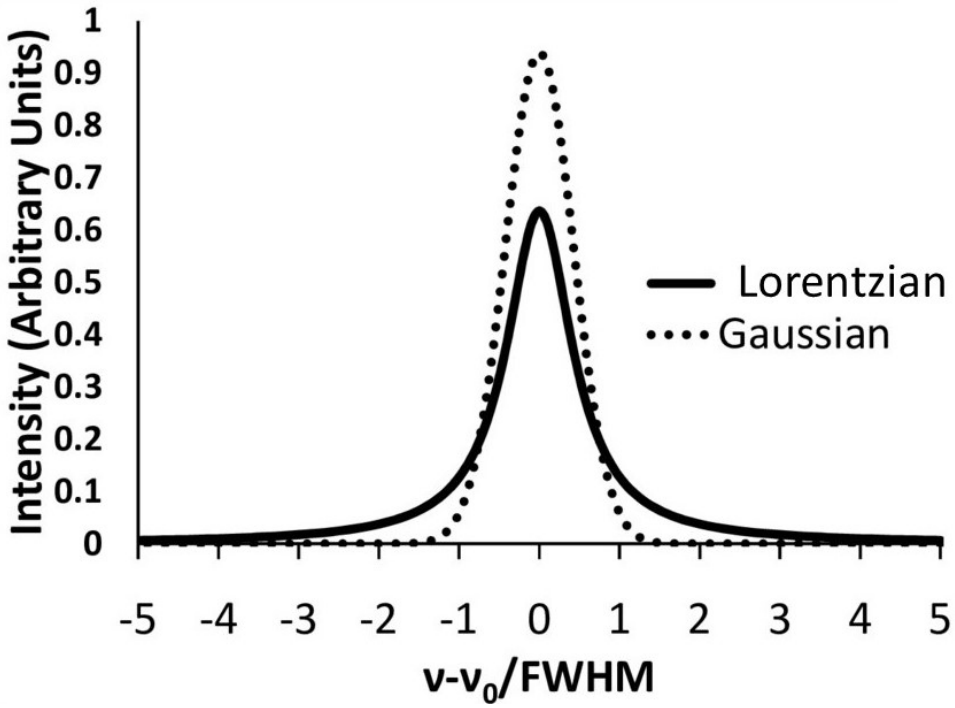

FIG. 2: Gaussian and Lorentzian lineshapes [9].

distribution of the molecules resulting in a FWHM of [7]:

$$\Delta\nu = \frac{2\nu}{c}\left(\frac{2N_A kT\ln(2)}{M}\right)^{1/2} = 7.15\times10^{-7}\left(\frac{T}{M}\right)^{1/2}\nu, \tag{24}$$

where N_A is Avagadro's number, k is the Boltzmann constant, T is the temperature in K, and M is the mass in amu.

A Voigt lineshape function is a composite function with both Gaussian and Lorentzian components. Voigt lineshapes are often used in satellite remote sensing, to include the Atmospheric Chemistry Experiment (ACE), on which a large portion of this work is based. Further discussion regarding satellite remote sensing and the ACE satellite is provided in the Satellite Remote Sensing Chapter.

Transit time broadening involves the use of lasers in molecular spectroscopy. If a laser beam of width d crosses a beam of molecules moving at velocity v, the molecules only interact with the laser for a time $\tau = d/v$. This interaction causes transit time broadening, which can be estimated for experimental purposes to be $\Delta v_{1/2} = 0.89/\tau$ [1].

2.5 BEER-LAMBERT LAW

The Einstein A and B coefficients, $A_{1\to 0}$ and $B_{1\leftarrow 0}$ were introduced and shown in equations (5)-(7) and equations (13)-(14). In the same section the transition dipole moment μ_{10} was introduced. Bernath [1] derives expressions for the Einstein A and B coefficients using the transition dipole moment:

$$B_{1\leftarrow 0} = \frac{1}{6\epsilon_0 \hbar^2}\mu_{10}^2 = \frac{2\pi^2}{3\epsilon_0 h^2}\mu_{10}^2, \tag{25}$$

and then using equation (14):

$$A_{1\to 0} = \frac{16\pi^3\nu^3}{3\epsilon_0 hc^3}\mu_{10}^2. \tag{26}$$

Now including the lineshape function the equations become:

$$(B_{1\leftarrow 0})_\nu = \frac{2\pi^2}{3\epsilon_0 h^2}\mu_{10}^2 g(\nu-\nu_{10}), \tag{27}$$

and:

$$(A_{1\to 0})_\nu = \frac{16\pi^3\nu^3}{3\epsilon_0 hc^3}\mu_{10}^2 g(\nu-\nu_{10}). \tag{28}$$

Returning to the previously discussed two-level system, with N_0 molecules in the lower/ground state and N_1 molecules in the upper/excited state, the system is now irradiated with photons. Define the flux of photons as F_0 where $F_0 = I_0/h\nu$ in units $\frac{\text{photons}}{\text{m}^2\text{s}}$ and the radiation density $\rho = I/c = h\nu F/c$. The sought after unknown in this scenario is the the intensity of radiation I after the incident radiation intensity I_0 has travelled a distance l through the two level system of molecules.

Taking into consideration energy transitions caused by the incident radiation, namely absorption and stimulated emission and using the definition of the Einstein B coefficients:

$$\frac{dN_1}{dt} = -B_{1\to 0}\rho N_1 + B_{1\leftarrow 0}\rho N_0, \tag{29}$$

and making use of equation (26):

$$\frac{dN_1}{dt} = -\frac{2\pi^2\mu_{10}^2}{3\epsilon_0 h^2}g(\nu-\nu_{10})\rho N_1 + \frac{2\pi^2\mu_{10}^2}{3\epsilon_0 h^2}g(\nu-\nu_{10})\rho N_0, \tag{30}$$

reorganizing:

$$\frac{dN_1}{dt} = \frac{2\pi^2\mu_{10}^2}{3\epsilon_0 h^2}g(\nu-\nu_{10})(N_0-N_1)\rho, \tag{31}$$

using $\rho = h\nu F/c$:

$$\frac{dN_1}{dt} = \sigma F(N_0 - N_1), \tag{32}$$

where the absorption cross section σ is defined as:

$$\sigma = \frac{2\pi^2 \mu_{10}^2}{3\epsilon_0 hc} \nu g(\nu - \nu_{10}). \tag{33}$$

Let the flux F be incident on a small thickness dx of the system with unit cross sectional area, the resultant change in flux due to passing through a small portion of the system is:

$$dF = -\sigma F(N_0 - N_1)dx. \tag{34}$$

Integrating over the path as x goes from 0 to l and F diminishes from F_0 to F:

$$\int_{F_0}^{F} \frac{dF}{F} = -\sigma(N_0 - N_1) \int_0^l dx \tag{35}$$

$$\ln \frac{F}{F_0} = \ln \frac{I/h\nu}{I_0/h\nu} = \ln \frac{I}{I_0} = -\sigma(N_0 - N_1)l, \tag{36}$$

which yields the Beer-Lambert law:

$$I = I_0 e^{-\sigma(N_0 - N_1)l}. \tag{37}$$

The Beer-Lambert law, in addition to mathematical utility, concisely describes absorption spectroscopy: a source of known radiation is incident on a system of a known quantity of molecules over a known path length, the radiation that passes through the system is measured, and the absorption cross section of the molecule is calculated. While this description fits laboratory absorption spectroscopy, clearly there are multiple other scenarios in which other quantities are the unknown. Some of these other scenarios can be seen by the variations of the Beer-Lambert law. The absorption coefficient is defined as $\alpha = \sigma(N_0 - N_1)$ combining two potential unknowns into one:

$$I = I_0 e^{-\alpha l}. \tag{38}$$

In a similar manner the column density is defined as $x = (N_0 - N_1)l$ resulting in:

$$I = I_0 e^{-\sigma x}. \tag{39}$$

2.6 BORN-OPPENHEIMER APPROXIMATION

The Born-Oppenheimer Approximation is essential to molecular spectroscopy; the basic concept is that the motion of the nuclei and electrons can be addressed separately. The non-relativistic Hamiltonian for a molecule is:

$$\hat{H} = \hat{T}_N + \hat{T}_e + \hat{V}_{NN} + \hat{V}_{eN} + \hat{V}_{ee}. \tag{40}$$

The individual operators are defined below.

$\hat{T}_N$ is the nuclear kinetic energy, where M_α are the nuclear masses:

$$\hat{T}_N = \frac{-\hbar^2}{2} \sum_\alpha \frac{\nabla_\alpha^2}{M_\alpha}. \tag{41}$$

$\hat{T}_e$ is the electronic kinetic energy, where m_e is the electron mass:

$$\hat{T}_e = \frac{-\hbar^2}{2m_e} \sum_i \nabla_i^2. \tag{42}$$

$\hat{V}_{NN}$ is the Coulomb potential due to repulsion between nuclei, $Z_\alpha e$ and $Z_\beta e$ are the nuclear charges:

$$\hat{V}_{NN} = \sum_\alpha \sum_{\beta>\alpha} \frac{Z_\alpha Z_\beta e^2}{4\pi\epsilon_0 r_{\alpha\beta}}. \tag{43}$$

$\hat{V}_{eN}$ is the Coulomb potential due to attraction between nuclei and electrons, e is the electron charge:

$$\hat{V}_{eN} = -\sum_\alpha \sum_i \frac{Z_\alpha e^2}{4\pi\epsilon_0 r_{i\alpha}}. \tag{44}$$

$\hat{V}_{ee}$ is the Coulomb potential due to repulsion between electrons:

$$\hat{V}_{ee} = \sum_i \sum_{j>i} \frac{e^2}{4\pi\epsilon_0 r_{ij}}. \tag{45}$$

As can be seen by the Coulomb potential operators, the forces acting on the nuclei and electrons are similar in magnitude. Due to electrons having much smaller mass than the nuclei, their velocities are significantly greater, justifying making the approximation that the nuclei are not moving relative to the electrons and then solving Schrödinger's equation for the electron alone:

$$\hat{H}_{el}\psi_{el} = E_{el}\psi_{el}. \tag{46}$$

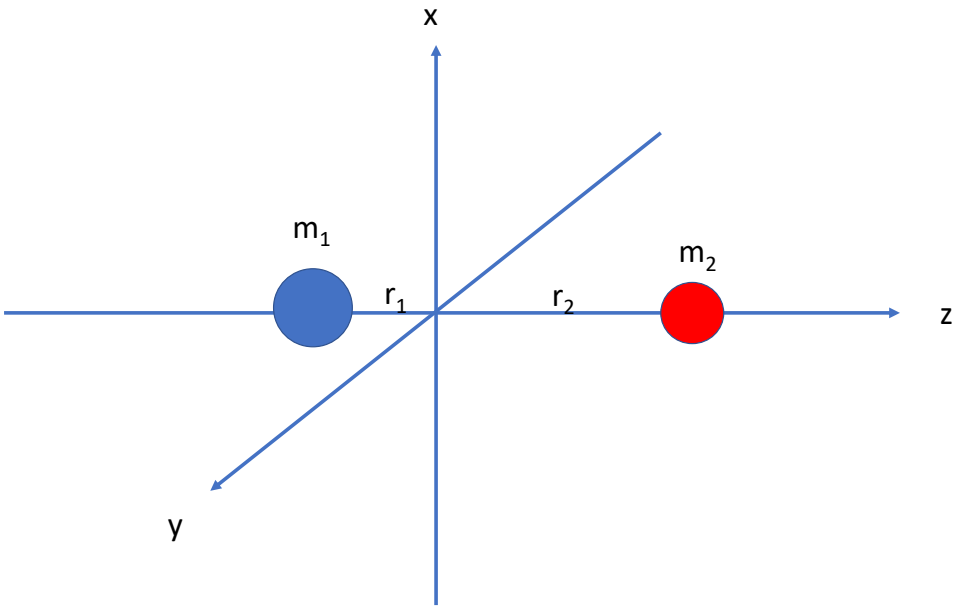

FIG. 3: Diatomic rigid body.

In addition, independent of the Born-Oppenheimer Approximation, it is assumed that the rotational and vibrational motion of a molecule can be separated.

2.7 ROTATIONAL SPECTROSCOPY

The discussion of rotational spectroscopy is focused on diatomic molecules, given that all the rotational analysis shown was carried out on diatomic molecules. The same principles apply to more complex molecules, but clearly diatomic molecules are the simplest case.

Rotational spectroscopy begins with modelling the molecule as a rotating rigid body. The equations for angular momentum and rotational energy of the rotating rigid body use the moment of inertia, I:

$$I_x = \sum_\alpha m_\alpha r_{x,\perp}^2, \tag{47}$$

where the x-axis is shown as an example, m_α are the masses in the system, in this case the atoms in the molecule, and $r_{x,\perp}$ is the perpendicular distance from the mass to the desired axis. As can be seen in Figure 3, in the case of a diatomic molecule, $I_x = I_y$ and $I_z = 0$.

From classical mechanics, the angular momentum L is:

$$L = I\omega, \tag{48}$$

where ω is the angular velocity, and the rotational kinetic energy is:

$$T = \frac{1}{2} I\omega^2. \tag{49}$$

Here molecular spectroscopy departs from conventional rigid body classical mechanics. Instead of angular momentum L, J is used to represent the total angular momentum, excluding nuclear spin. So the rotational energy is represented as:

$$E_R = \frac{J^2}{2I}. \tag{50}$$

Transitioning to quantum mechanics, the Hamiltonian operator is:

$$\hat{H} = \frac{\hat{J}^2}{2I}, \tag{51}$$

and Schrödinger's equation becomes:

$$\hat{H}\psi = \frac{\hat{J}^2\psi}{2I} = \frac{J(J+1)\hbar^2\psi}{2I} = BJ(J+1)\psi = E\psi, \tag{52}$$

where the rotational constant B is defined as:

$$B = \frac{\hbar^2}{2I}, \tag{53}$$

and the energy eigen value $F(J)$ is:

$$F(J) = BJ(J+1). \tag{54}$$

In molecular spectroscopy $F(J)$ is referred to as the rotational energy equation. As discussed in the Line Intensity section, the intensity of the rotational transition is dependent upon the dipole moment. Analysis of the transition dipole moment shows that there is a selection rule for rotational transitions, specifically that the value of J can only change by 1, or $\Delta J = \pm 1$. There are ways to break the selection rule for J, for example, if there are additional angular momentum sources, such as vibrational angular momentum, then $\Delta J = 0$ is possible. Rotational transitions are possible in which the value of J changes by more than 1; but one photon, electric dipole allowed transitions are limited to $\Delta J = 0, \pm 1$. Transitions in which the J value changes by more than 1 are produced by factors such as multi-photon transitions, electric quadrupole transitions and the Raman effect; none of the research included in this

work focused on those areas of rotational spectroscopy. Rotational spectra are organized into branches based on the value of the J transition; $\Delta J = 0$ transitions are Q branches, $\Delta J = -1$ transitions are P branches and $\Delta J = +1$ branches are R branches. R branches often increase in energy with increasing J values and then reach a peak value and begin to decrease in energy as J continues to increase; the reversal of directions is referred to as a band head. In changing the value J by one to produce rotational transitions, the energy change associated with the transition is:

$$F(J') - F(J'') = B(J+1)(J+2) - B(J)(J+1) = 2B(J+1). \tag{55}$$

In other words, the spacing between the rotational lines increases as J increases.

In the line intensity section it was shown the intensity of the transition is a function of the transition dipole moment. There is a second factor, namely, the difference in the population of molecules at the two levels involved in the transition. Given a total population of molecules N, from statistical mechanics the population at a given quantum number, N_J is [1]:

$$N_J = N(2J+1)\frac{e^{-BJ(J+1)/kT}}{q_r}, \tag{56}$$

where q_r is the partition function, (assuming $kT \gg B$):

$$q_r = \sum_J (2J+1)e^{-BJ(J+1)/kT}. \tag{57}$$

This section began with modelling the diatomic molecule as a rigid rotating body. The bond between the atoms is more like a spring; as the molecule rotates the bond stretches, a phenomenon called centrifugal distortion. There are other distortion effects as well; the rotational energy expression is actually a power series:

$$F(J) = BJ(J+1) - D(J(J+1))^2 + H(J(J+1))^3 + L(J(J+1))^4 + ... \tag{58}$$

where D is the centrifugal distortion constant. As practical matter, the rotational analysis in this work did not determine any constants beyond H.

Before transitioning to the next section, vibrational spectroscopy, it is important to note that the rotational and distortion constants in equation (58) are not constant throughout the spectrum of the molecule. Each of these constants varies with the vibrational quantum number, and can be expressed as a power series of the vibrational quantum number v. For the rotational constant B:

$$B_v = B_e - \alpha_e(v + \frac{1}{2}) + \gamma_e(v + \frac{1}{2})^2..., \tag{59}$$

and the centrifugal distortion constant D:

$$D_v = D_e - \beta_e(v + \frac{1}{2}) + ..., \tag{60}$$

where the the constants with subscript e in the power series are referred to as the equilibrium constants, while the rotation and distortion constants are referred to as the spectroscopic or molecular constants. A completely successful rotational analysis of a molecule will determine both sets of constants.

2.8 VIBRATIONAL SPECTROSCOPY

Similar to the discussion regarding rotational spectroscopy, the discussion of vibrational spectroscopy in this section is focused on diatomic molecules. Now the rigid diatomic molecule depicted in Figure 3 has the two atoms connected by a spring, whose rest length is $r_1 + r_2 = R_e$, the equilibrium length of the spring. If the spring length is changed to some new length R, the spring displacement from equilibrium is $q = R - R_e$. If the spring constant is k, then the potential energy stored in the displaced spring is $V = \frac{1}{2}kq^2$. The reduced mass of the system is $\mu = \frac{m_1 m_2}{m_1 + m_2}$. If the spring is released and set in motion, the resultant kinetic energy from the motion of the two masses is $T = \frac{p^2}{2\mu}$, where p is the momentum of the system. Putting it all together, the energy of the vibrating system is:

$$E_{vib} = \frac{p^2}{2\mu} + \frac{1}{2}kq^2. \tag{61}$$

Transitioning from classical mechanics to quantum mechanics, Schrödinger's equation is:

$$-\frac{\hbar^2}{2\mu}\frac{d^2\psi_v}{dq^2} + \frac{1}{2}kq^2\psi_v = E_v\psi_v, \tag{62}$$

where ψ_v is the vibrational waveform and E_v is the energy eigen value. E_v is known to be:

$$E_v = (v + \frac{1}{2})\hbar\omega. \tag{63}$$

Just as a rotating molecule is not actually rigid, the shape of the potential function is not actually a harmonic oscillator.

A better model for the potential function is the Morse potential:

$$V(q) = D(1 - e^{-\beta q})^2, \tag{64}$$

where the function asymptotically approaches the the dissociation limit D as q increases. The resultant form of Schrödinger's equation can be solved analytically:

$$E = \omega_e\left(v + \frac{1}{2}\right) - \omega_e x_e\left(v + \frac{1}{2}\right)^2 + B_e J(J+1) - D_e(J(J+1))^2 - \alpha_e\left(v + \frac{1}{2}\right)J(J+1). \tag{65}$$

Looking at equations (59) and (60) this can be rewritten:

$$E = \omega_e \left(v + \frac{1}{2}\right) - \omega_e x_e \left(v + \frac{1}{2}\right)^2 + B_v J(J+1) - D_v (J(J+1))^2, \tag{66}$$

or

$$E = \omega_e \left(v + \frac{1}{2}\right) - \omega_e x_e \left(v + \frac{1}{2}\right)^2 + F(J). \tag{67}$$

What emerges is the previous rotational energy equation, $F(J)$ and a new vibrational energy equation $G(v)$:

$$G(v) = \omega_e \left(v + \frac{1}{2}\right) - \omega_e x_e \left(v + \frac{1}{2}\right)^2. \tag{68}$$

The solution to the Morse oscillator only has two terms; it is not a power series such as $F(J)$ was shown to be.

A more general form the oscillator is the Dunham[10] potential, which does result in a power series for $G(v)$. The Dunham potential is generated by a Taylor series expansion of the potential function V of a rotating, vibrating diatomic molecule. The result is a power series of the form:

$$V(\xi) = a_0 \xi^2 (1 + a_1 \xi + a_2 \xi^2 + ...), \tag{69}$$

where $\xi - \frac{r - r_e}{r_e}$, r is the distance between the molecules, r_e is its equilibrium position and $a_0 = \frac{\omega_e^2}{4B_e}$. The energy levels are:

$$E_{vJ} = F_v(J) + G(v) = \sum_{jk} Y_{jk} (v + \frac{1}{2})^j (J(J+1))^k. \tag{70}$$

The Y_{jk} parameters match up with the equilibrium constants. Of the equilibrium constants already shown, $Y_{01} \approx B_e$, $Y_{02} \approx -De$, $Y_{10} \approx \omega_e$, $Y_{11} \approx -\alpha_e$, $Y_{12} \approx -\beta_e$, $Y_{20} \approx -\omega_e x_e$ and $Y_{21} \approx \gamma_e$. Equally important, the relationship between the Y_{jk} parameters and the reduced mass of the molecule μ can be seen, allowing the conversion of the equilibrium constants of any isotopologue to the equilibrium constants of of its other isotopologues:

$$Y_{jk} \propto \mu^{-(j+2k)/2}. \tag{71}$$

The vibrational energy levels of a molecule can be pictured as energy levels within the potential energy curve. A transition from one vibrational level to another is referred to as a band in spectroscopy. Transitioning from $v = 0$ to $v = 1$ is the fundamental band. Going from $v = 0$ to higher v values are overtones. Beginning at a level other than $v = 0$ and moving to a higher v number is a hot band. See Figure 4.

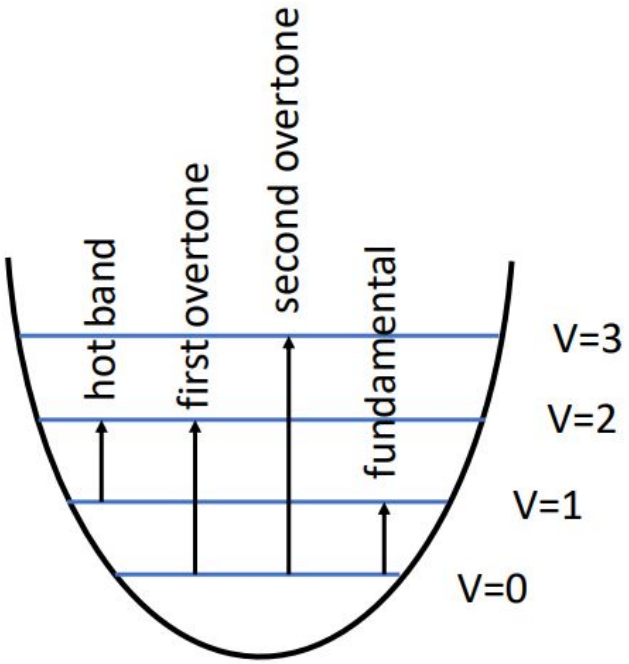

FIG. 4: Vibrational transitions.

2.9 ELECTRONIC SPECTROSCOPY

Molecular orbital theory is based on the assumption that molecular orbitals are the result of linear combinations of atomic orbitals. Electrons of the s atomic orbitals of the two atoms making up a diatomic molecule combine to make $s\sigma$ molecular orbitals; if they interact in phase, they form a bonding orbital, denoted as a σ_g or sometimes shown in diagrams as simply a σ orbital. If the atomic s orbitals are out of phase, they from an antibonding orbital, denoted as a σ_u^* molecular orbital. The letters g and u in the subscripts stand for gerade and ungerade, the German words for even and odd, respectively. The atomic p orbitals form $p\sigma$ or $p\pi$ molecular orbitals in diatomic molecules based on the axis of the p oribital. If the internuclear axis is taken as the z axis, then the p_z orbitals form a bonding σ_g or antibonding σ_u^* molecular orbital. The atomic p_x and p_y orbitals are oriented perpendicular to the internuclear axis, and form bonding π_u or antibonding π_g^* molecular orbitals. Similarly, atomic d orbitals form molecular $d\sigma, d\pi$ and $d\delta$ molecular oribitals while atomic f oribitals

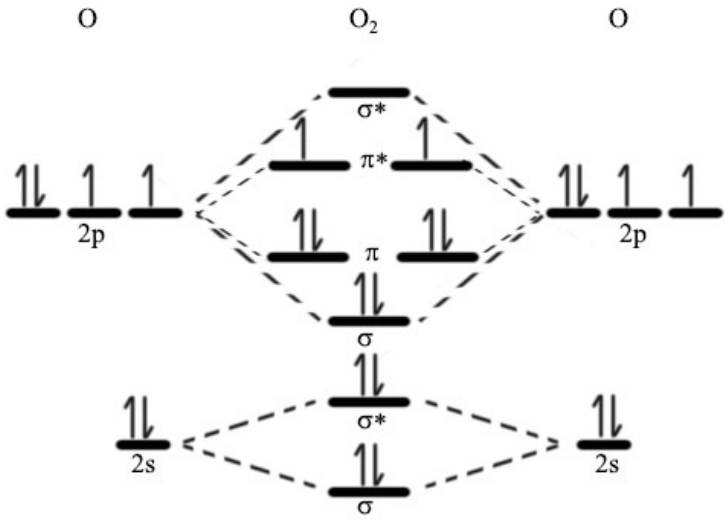

FIG. 5: O_2 Molecular orbital diagram [11].

form molecular $f\sigma, f\pi, f\delta$ and $f\phi$ orbitals. See Figure 5.

The notation used to designate the electron states for diatomic molecules parallels the notation used in atomic term symbols, ${}^{2S+1}L_J$, where S, L and J are the familiar quantum numbers. The equivalent molecular form is ${}^{2S+1}\Lambda_\Omega$. The Ω subscript is not always shown. See the diagram of a fictitious diatomic molecule AB in Figure 6 for an explanation of the relationship between conventional quantum numbers and the Greek letters used in diatomic molecular symbology. Capital Greek letters indicate multi-electron labels; lower case indicates single electron labels.

Note in Figure 6 that a two-fold degeneracy is possible based on the orientation of Λ. The reader can visualize the degeneracy by imagining the electron circulation being in the opposite direction. This degeneracy is known as Λ-doubling and it is possible in the particular angular momenta orientation configuration shown in Figure 6, which is known as Hund's case (a).

There are several different Hund's cases possible for diatomic molecules, cases (a) though (e). As noted by Brown and Carrington, "...Hund's coupling cases are idealised situations which help us to understand the pattern of rotational levels and the resulting spectra [7]." The only research presented in this work in which the Hund's case is influential is the spectrum of TiO, which falls under Hund's case (a). The key requirement for Hund's case(a)

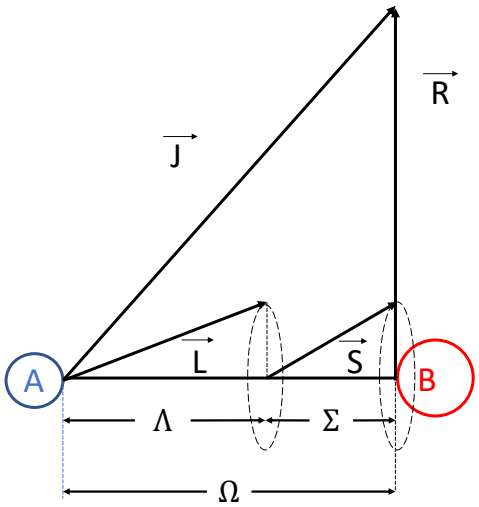

FIG. 6: Angular momenta in a diatomic molecule (Hund's case(a)) [1].

is $A\Lambda \gg BJ$, where A is the spin-orbit coupling constant and B is the previously introduced rotational constant. In addition to the potential for Λ-doubling, the other hallmark of Hund's case (a) diatomic spectra is $2S + 1$ fine structure states. Each fine structure state has its own pattern of rotational levels.

A molecule can transition to alternative electron orbital structures, the different possible electron states for a molecule are given labels. Each electron state has a letter, placed in front of the ${}^{2S+1}\Lambda_{\Omega}$ symbology. The letter X is reserved for the ground state. The other states with the same $(2S + 1)$ muliplicity as the ground state are given the letters A, B, C etc., in order of increasing energy. States with a $(2S + 1)$ multiplicity different than the ground state are given lower case letter designations, also in order of increasing energy. The comprehensive line list for the spectrum of the TiO molecule, McKemmish et al. (2019) [12], provides a diagram of the molecular orbital structure of TiO. See Figure 7.

A molecular energy transition typically involves a transition from one electron state to another, with each the two electron states each having multiple vibrational levels. Conducting a spectroscopic rotational analysis entails knowing which electron states are involved, which vibrational bands are involved, which rotational branches are involved, and then which J transitions are within each rotational branch. A handy way to picture diatomic transitions is to plot the potential energy curves of the two electron states involved with energy levels

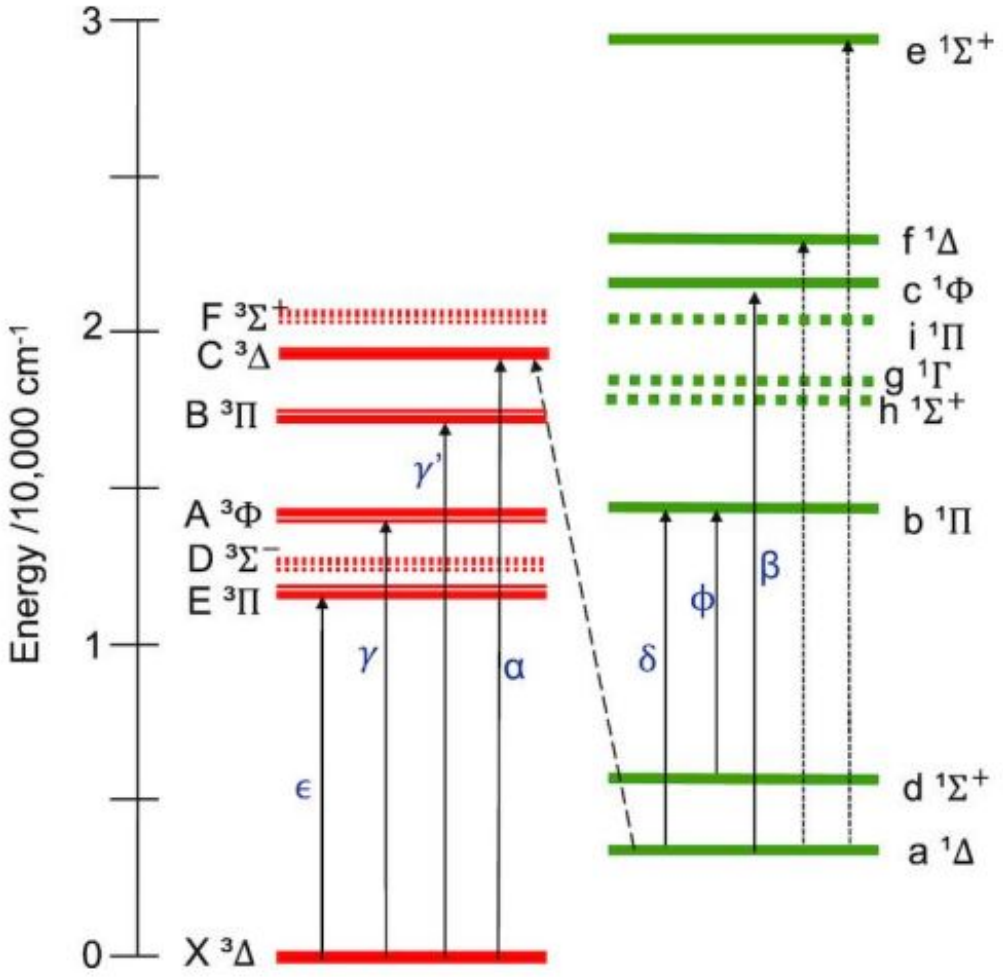

FIG. 7: Molecular orbital structure of TiO [12].

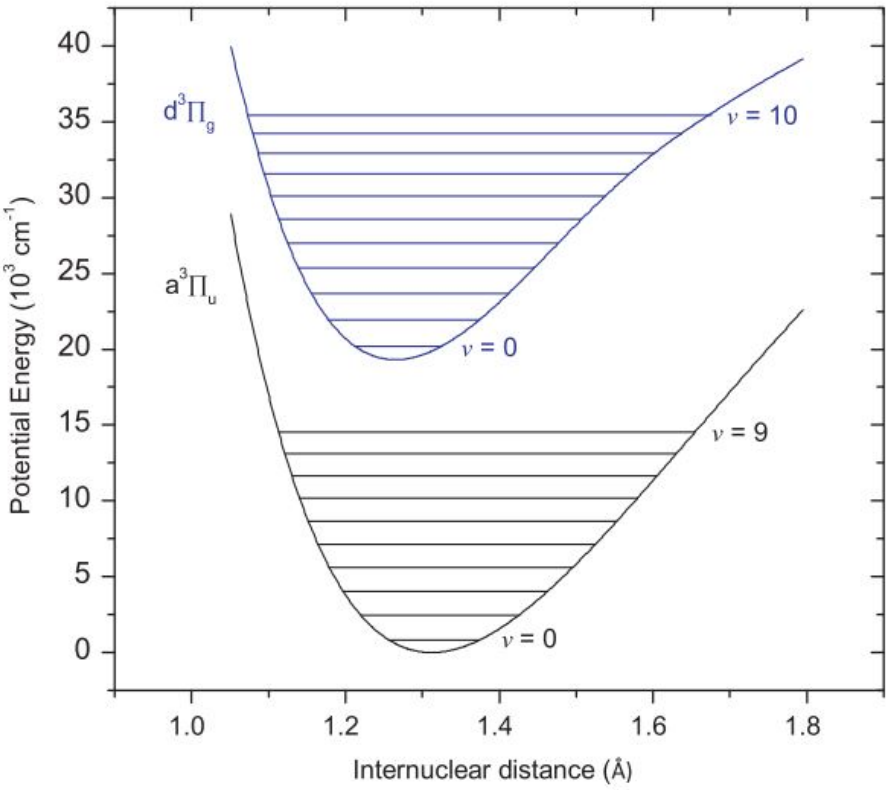

FIG. 8: C_2 $d^3\Pi_g - a^3\Pi_u$ system [13].

on the y axis and internuclear distance on the x axis; individual vibrational energy levels are plotted within each potential energy curve. Figure 8 shows such a plot for the $d^3\Pi_g - a^3\Pi_u$ transition of the C_2 molecule.

Looking at the $v = 0$ lines in both potential energy curves of Figure 8, the two $v = 0$ lines are roughly 19000 cm^{-1} apart. So the rotational lines for the C_2 $d^3\Pi_g - a^3\Pi_u$ $(0, 0)$ band should be in the area of 19000 cm^{-1}. Figure 8 was taken from Brooke et al. (2013)[13], a paper investigating this C_2 transition. The same paper provides a graphic sample of P and R Branch lines from the $(0, 0)$ transition, with the lines being in the 19,000 cm^{-1} region, as expected. See Figure 9.

2.10 FRANCK-CONDON FACTOR

The Franck-Condon principle is based on the concept that electrons transitions occur

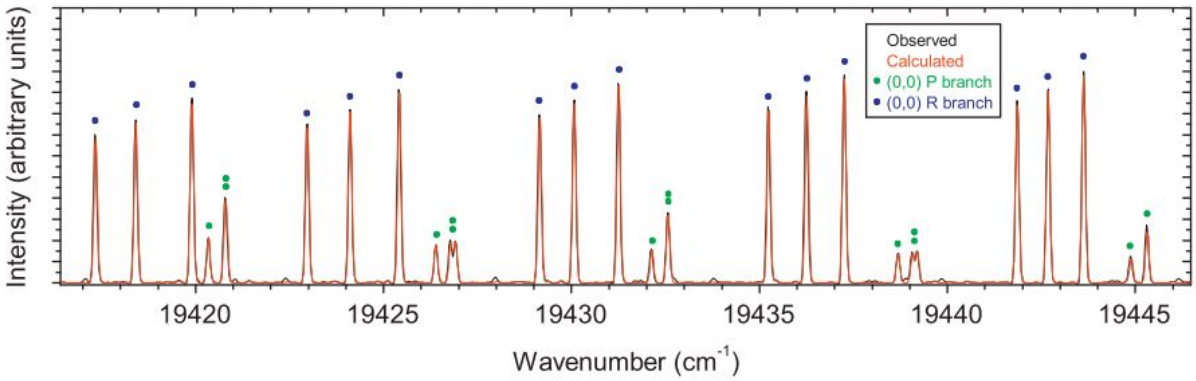

FIG. 9: Portion of the C_2 $d^3\Pi_g - a^3\Pi_u$ $(0-0)$ band; P branch: $J'' = 36-41$, R branch: $J'' = 7-13$ [13].

quickly, the nuclei do not have time to move, so vibration, rotation and translation can all assumed to be locked in place for the duration of the electron transition. Looking at a potential energy diagram, such as Figure 8, the transition between electron states can be assumed to to be a vertical line, at a constant internuclear distance. The more overlap between v state horizontal lines in the two electron states, the stronger the vibrational band is likely to be. This overlap is quantified and called the Franck-Condon factor. The vibrational overlap integral is defined as:

$$\langle v'|v''\rangle = \int \psi^*_{v'}\psi_{v''}dr, \tag{72}$$

where ψ_v is the vibrational wave form. The Franck-Condon factor is:

$$q_{v'-v''} = |\langle v'|v''\rangle|^2. \tag{73}$$

The electronic dipole moment (see Section 2.3) is defined as:

$$R_e(r) = \langle \psi'_{el}|\overrightarrow{\mu}|\psi''_{el}\rangle, \tag{74}$$

where ψ_{el} is the electronic waveform. The intensity of the vibronic transition is proportional to the Franck Condon factor and the square of the electronic dipole moment:

$$I_{el'v'el''v''} \propto |R_e|^2 q_{v'-v''}. \tag{75}$$

CHAPTER 3

LABORATORY SPECTROSCOPY

3.1 FOURIER TRANSFORM SPECTROMETERS

The purpose of any spectrometer is to determine how much light is emitted or absorbed at each wavelength of interest. There are a variety of methods by which spectrometers accomplish those tasks. Prisms and diffraction gratings separate light by wavelengths. Monochromators block all light with the exception of the desired wavelength. All of the spectra presented in this work were recorded with Fourier transform spectrometers.

Fourier transform spectrometers process a beam of light containing all of its different wavelengths. Using a Michelson interferometer, the coherent beam is split and then recombined, causing a wave interference pattern to form, known as an interferogram. The interferogram is processed by mathematical/computer methods to produce a spectrum. Figure 10 shows a rudimentary diagram of a Michelson interferometer. The path length difference p for the two paths the light takes after the beamsplitter M is $p = 2d_1 - 2d_2$. Note d_2 is variable and controlled by moving mirror M_1. The compensator lens C is present so both lengths have the same number of passages through a lens (C and M must be of the same thickness).

The detector measures the intensity I as a function of wavenumber $\tilde{\nu}$ and path length p, $I(p, \tilde{\nu})$. The effect of the path length difference on the incoming light, which varies only with $\tilde{\nu}$ is:

$$I(p, \tilde{\nu}) = I(\tilde{\nu})[1 + \cos(2\pi\tilde{\nu}p)], \tag{76}$$

where the desired data is $I(\tilde{\nu})$. Defining $I(p)$ as

$$I(p) = \int_0^\infty I(p, \tilde{\nu})d\tilde{\nu} = \int_0^\infty I(\tilde{\nu})[1 + \cos(2\pi\tilde{\nu}p)]d\tilde{\nu}, \tag{77}$$

noting $I(p)$ is measurable and its equation is a Fourier cosine transform, taking the inverse Fourier cosine transform leaves an integral which can be solved:

$$I(\tilde{\nu}) = 4\int_0^\infty \left[I(p) - \frac{1}{2}I(p = 0)\right]\cos(2\pi\tilde{\nu}p)dp. \tag{78}$$

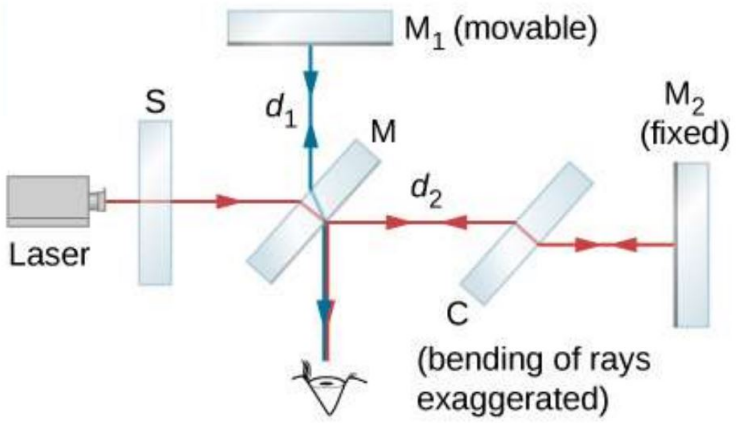

FIG. 10: Michelson interferometer [14].

The Fourier transform infrared spectrometer (FTIR) offers some advantages over scanning monochromator type spectrometers. Fellgett's advantage [15], caused by FTIRs detecting all wavelengths simultaneously, provides an advantage in signal to noise ratio (SNR) on the order of the square root of the number of sample points in the spectrum. This advantage fades in the visible and ultraviolet (UV) wavelengths due to the detectors used by a FTIR, where as a result of shot noise or Poisson noise, which is characteristic of a signal coming from an electric charge, Fellget's advantage is offset.

The Atmospheric Chemistry Laboratory at Old Domininion University was used for this research. The lab contains two Bruker IFS 125 HR FTIR spectrometers. One is set up for absorption spectroscopy, the other for emission spectroscopy. The absorption spectrometer uses an internal gas cell where the molecule to be studied is piped into the cell where it is held at the desired temperature and pressure. The emission spectrometer can use a variety of external emission sources such as a furnace, composite wall hollow cathode or Broida oven.

3.2 BROIDA OVEN

The Broida oven is a flow system used to produce diatomic metal oxides and halides. The metal is vaporized, entrained in an inert gas, and then mixed with an oxidizing agent to produce chemiluminescence, from which an emission spectrum is taken. The design of the apparatus was presented in 1975 by West et al.[16] from UC Santa Barbara and named after

H. P. Broida, a prominent physicist there from 1963-1978. Figure 11 provides a schematic diagram of the internal baseplate of the Broida oven. Various components are noted in the figure: (a) chemiluminescent flame, (b) oxidizing gas ring, (c) tungsten wire basket heating element, (d) inerting gas ring, (e) coolant line, (f) oxidizing gas line, (g) electrical lines for heating element, (h) metal sample, (i) crucible, (j) alumina heat shield. As stated by West et al. [16], the Broida oven offers some specific advantages in molecular spectroscopy: (a) it can handle a large number of reactants, (b) there is little thermal excitation from the reaction, (c) uncluttered spectra, free from undesirable species are produced, and (d) excited electronic states can be produced in the molecules formed that are typically not produced by other means.

The Bernath research group has previously operated the Broida oven. Records in the lab indicate it was last used in 2006. The oven itself was largely disassembled and parts were missing. Blueprint drawings of the device were located, dated 1981. The drawings were key in that they depicted proper assembly, and detailed missing parts to be ordered and in some cases locally manufactured by the Physics Department machine shop. Restoring the oven and conducting research with it was one of my research assignments. A photo of the restored Broida oven is shown in Figure 12. The large canister in the bottom right hand corner of the figure is an air filter to prevent particles from reaching the vacuum pump used to keep the oven at low pressure, typically on the order of 0.05 Torr background pressure. The small round observation window in the center of the photo is aligned with the chemiluminescent flame, item (a) in Figure 11. There is a similar window on the opposite side from which the spectrum is taken, with the signal routed into the FTIR using lenses and mirrors to reach a similarly sized input window for the spectrometer.

Operating the Broida oven has shown that starting with the previously mentioned background pressure of about 0.5 Torr, the inerting gas, typically argon, is injected at about 2-4 Torr. The oxidizing gas typically is injected at about 0.1 Torr. About 30 Amps is required to produce the vaporized metal, with a gradual heating schedule over a period of about an hour. Chemiluminescence is typically sustained for about 2 hours. Figure 13 shows a test run from September 2022.

The top window, in addition to being a viewing port, can be used to inject a laser beam into the reaction region, exciting the molecule to elevated energy levels. Figure 14 shows a test run using laser excitation.

The Broida oven is now fully operational and ready for research. Preliminary results are promising. After methodically screening the spectra of a variety of diatomic metals, the

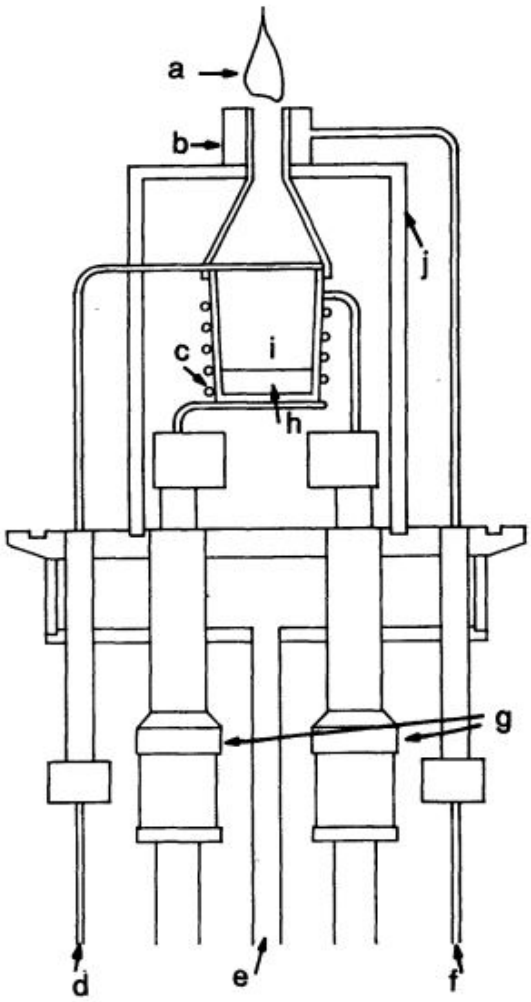

FIG. 11: Broida oven baseplate diagram [17].

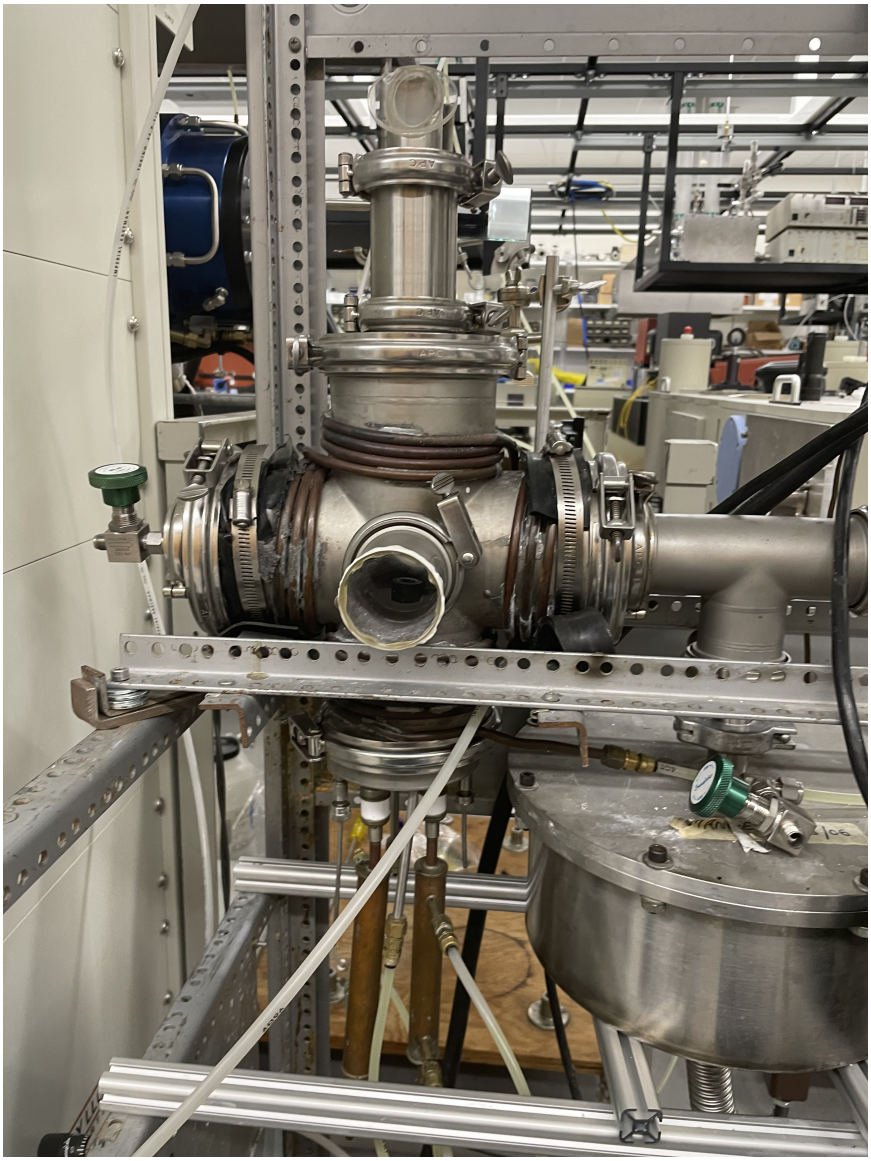

FIG. 12: Broida oven.

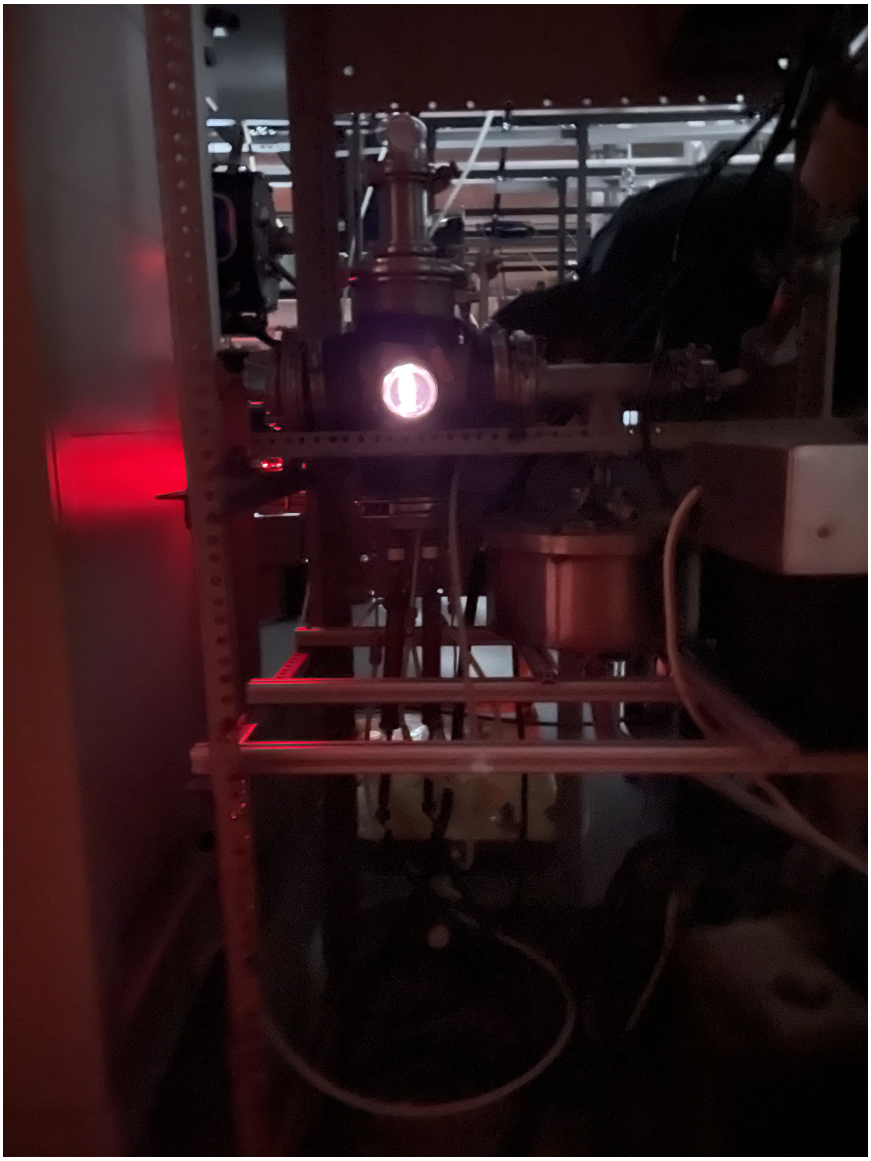

FIG. 13: Broida oven with chemiluminescent flame.

FIG. 14: Broida oven with laser excitation.

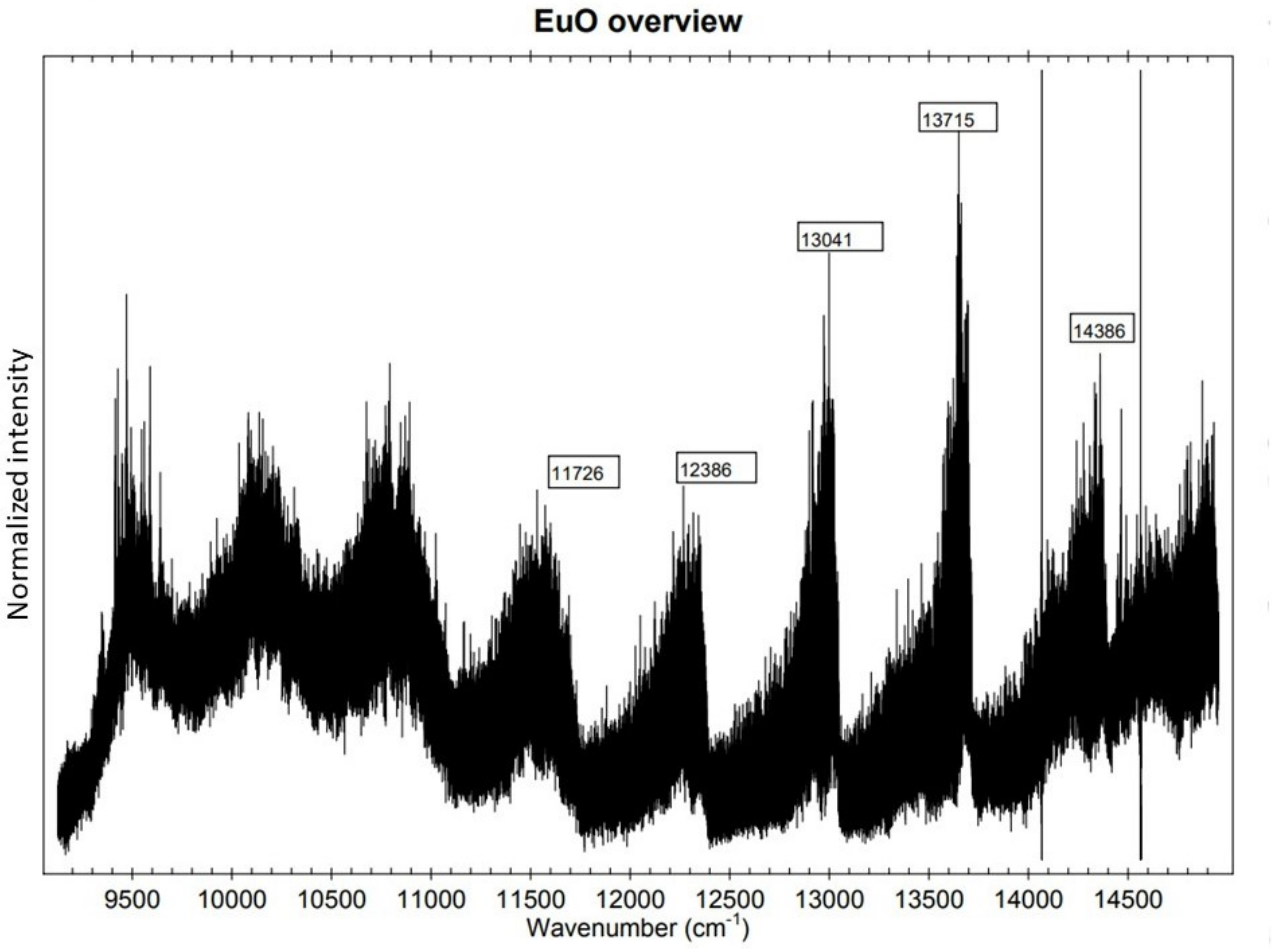

FIG. 15: Previous EuO spectrum.

research is focused on europium oxide (EuO). A previous edition of the Bernath research team recorded a spectrum of EuO, but it was never published or even analyzed. That spectrum is shown in Figure 15.

A similar spectrum was captured using the Broida oven on 14 Dec 2022. See Figure 16. In comparing the two spectra it is important to note that there was no processing of the data. The next section describes analysis of raw spectral data by computer methods. The hope on the recently obtained spectrum was for the appearance of peaks as opposed to random noise in the spectral plot, and agreement of those peak positions with known peak positions of EuO. Note the more recent spectra is at a slightly higher wave number range. The peaks

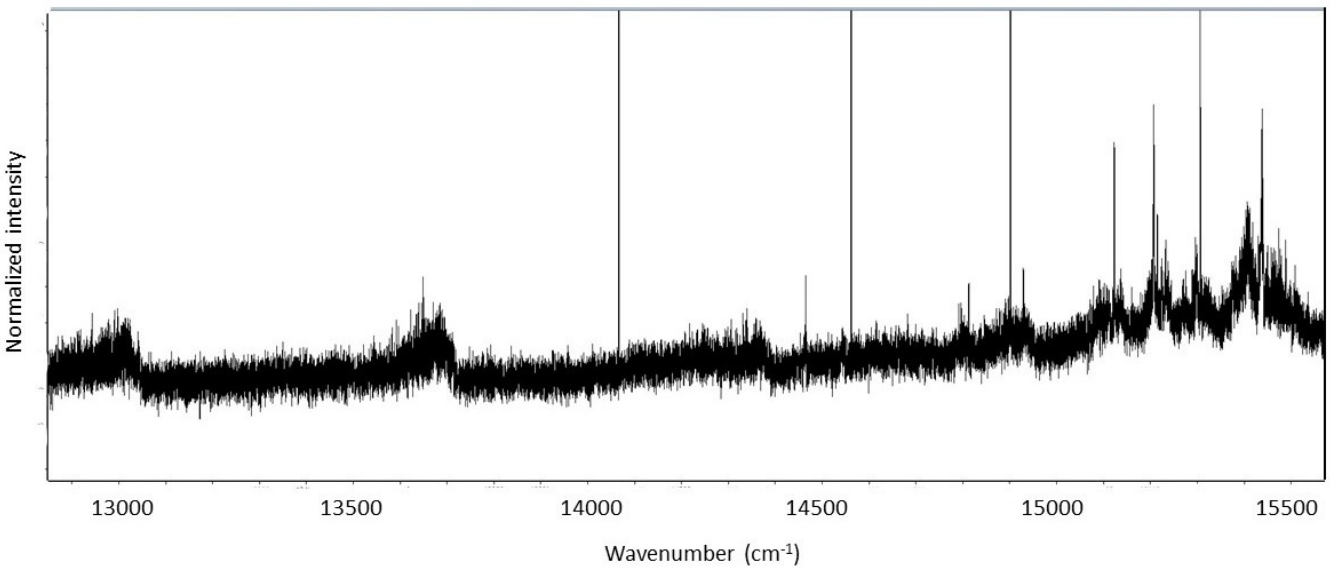

FIG. 16: 14 Dec 2022 EuO spectrum.

between the two spectra match at 13715 cm^{-1} and 14386 cm^{-1}. The more prominent peaks on the recent spectrum are off the scale in a higher wave number region in comparison to the previous work. The sharp, tall individual lines are atomic spectral lines, and the lines at about 14080 cm^{-1} and 14570 cm^{-1} also match up with the older plot. Follow up research is ongoing.

3.3 COMPUTER ANALYSIS OF MOLECULAR SPECTRA

3.3.1 OVERVIEW

Molecular spectra downloaded from a spectrometer typically go through several levels of analysis to obtain the desired data. Such analysis tends to be on a large scale and iterative, both characteristics favor computer analysis techniques. There are multiple options. The discussion here highlights the software used in this research and the underlying principles upon which they operate.

3.3.2 BRUKER OPUS [18]

If the spectrum to be analyzed was taken with a Bruker FTIR spectrometer, then analysis of the spectrum begins with Bruker's OPUS spectroscopy software. OPUS is the operating system for user interface with the spectrometer and includes the ability to set initial parameters such as designating which beam splitter and detector are in use as well as specifying collection parameters such as aperture and resolution.

OPUS also facilitates electronic storage of the spectral data and preliminary data manipulation, mostly in the realm of calibrating the spectrum. After the spectrum has been collected OPUS can flatten the baseline; the bottom of the plotted spectral lines is typically not a flat line on collected spectra as can be seen in Figure 16. This baseline correction is essentially done by hand/eye. The accuracy of line positions can be calibrated by a function known as peak picking, where a known piece of the displayed spectrum is selected, often CO_2 is used since its spectrum is well known to a high degree of accuracy and is typically present in spectra collected in a laboratory. Peaks with known positions are picked and the plot is then scaled to show accurate line positions in the known spectrum as well as throughout the data. The initial recorded spectrum shows the y-axis line intensity in dimensionless I/I_0 units where I is the intensity measured and I_0 is the intensity of an empty test cell. Line intensity is calibrated by referencing the Beer-Lambert law, equations (38)-(40), taking the natural log of plotted y values converts the y values to the more valuable absorption cross section in units cm^2/molecule.

3.3.3 PGOPHER

After a spectrum is calibrated and formatted, a major portion of the research remaining is to assign the individual lines of the spectrum and determine the spectroscopic and equilibrium constants. PGOPHER [19] is an open source program that can be used to simulate and fit molecular spectra; the graphical user interface is particularly useful for fitting rotational structure. Interactions such as electron spin and nuclear spin as well as external electric and magnetic fields can be modeled. In addition to line positions, line intensities and band contours can also be fitted. Perturbations caused by energy levels of other electron states at nearly the same as energy levels of the desired state can be included in the model. The simulation and fitting of the spectrum results in a line list of the modeled transition(s) as well as rotational constants.

The essential function of PGOPHER for this research was the determination of energy

levels. To solve for energy levels, the wave function for a given rovibrational level is expanded as a linear combination of basis states:

$$\Psi_i = \sum_j c_j^i |j\rangle, \tag{79}$$

where $|j\rangle$ is the basis state, generally of the form $|\eta s J K M\rangle$. In the PGOPHER basis state format, the electron and vibrational state are combined into a single variable η, s is spin, J is the total angular momentum, K is the projection of J along the molecular axis and M is the projection of J along a laboratory axis; M is only applicable with external electric or magnetic fields and was not used in this research. The basis state can be expanded to include hyperfine quantum numbers.

After determining the basis state, the Hamiltonian matrix is set up and diagonalized. There are Hamiltonian terms for the various interfaces that effect the energy level; PGOPHER uses the $\hat{N}^2$ Hamiltonian rotational operator term for diatomic molecules:

$$\hat{H}_{rot} = B\hat{N}^2 - D\hat{N}^4 + H\hat{N}^6 + L\hat{N}^8..., \tag{80}$$

which eliminates the problematic $\hat{L}$ term, (note $\hat{N} = \hat{R} + \hat{L}$). The basic Hamiltonian forms for spin-rotation ($\hat{H}_{SR}$), spin-orbit ($\hat{H}_{SO}$) and spin-spin ($\hat{H}_{SS}$) effects are:

$$\hat{H}_{SR} = \gamma \hat{N} \cdot \hat{S}, \tag{81}$$

$$\hat{H}_{SO} = A\hat{L}_z\hat{S}_z, \tag{82}$$

and

$$\hat{H}_{SS} = 2/3\lambda(3\hat{S}_z^2 - \hat{S}^2). \tag{83}$$

The above Hamiltonian terms can all be expanded by adding centrifugal distortion terms. There is also a Λ doubling term for Π electron states:

$$1/2q(\hat{N}_+^2 e^{-2i\phi} + \hat{N}_-^2 e^{+2i\phi}) - 1/2p(\hat{N}_+\hat{S}_+ e^{-2i\phi} + \hat{N}_-\hat{S}_- e^{+2i\phi}) + 1/2o(\hat{S}_+^2 e^{-2i\phi} + \hat{S}_-^2 e^{+2i\phi}). \tag{84}$$

The fitting of spectral lines is accomplished by designating which spectroscopic constants are to be floated (meaning they are changeable by the program) when the user designates the new position of a simulated line, based on a comparison of the simulated spectrum to the experimentally obtained spectrum. The floated spectroscopic constants are modified to accommodate the change in line position the user selected. The fitting of lines continues until the observed minus calculated error average of all fitted lines matches the desired level of accuracy and the floated spectroscopic constants have stabilized with an acceptably small standard deviation.

RKR1

RKR1 [20] is a computer program that uses the Rydberg-Klein-Rees (RKR) procedure to determine the potential energy function of a diatomic molecule. The program is based on the dependence of the vibrational energy G_v and rotational constants B_v on the vibrational quantum number v:

$$G_v = \omega_e \left(v + \frac{1}{2}\right) - \omega_e x_e \left(v + \frac{1}{2}\right)^2 + ... \tag{85}$$

$$B_v = B_e - \alpha_e \left(v + \frac{1}{2}\right) + \gamma_e \left(v + \frac{1}{2}\right)^2 + ... \tag{86}$$

The RKR method is within the first order WKB (Wentzel, Kramers, Brillouin) approximation. The RKR method is based on the Klein integrals:

$$r_2(v) - r_1(v) = 2\sqrt{C_u/\mu} \int_{v_{min}}^{v} \frac{dv'}{[G_v - G_{v'}]^{1/2}} = 2f, \tag{87}$$

and

$$\frac{1}{r_1(v)} - \frac{1}{r_2(v)} = 2\sqrt{\mu/C_u} \int_{v_{min}}^{v} \frac{B_{v'} dv'}{[G_v - G_{v'}]^{1/2}} = 2g, \tag{88}$$

where $r_1(v)$ and $r_2(v)$ are the inner and outer turning points of the potential energy function for vibrational level v with energy G_v and rotational constant B_v. The constant C_u is $\hbar^2/2$ and μ is the reduced mass of the molecule. The lower limit of integration v_{min} is the non-integer effective value of the vibrational quantum number at the potential minimum. The Klein integrals are solved numerically. They can be rearranged to show that:

$$r_1(v) = \sqrt{f^2 + f/g} - f, \tag{89}$$

and

$$r_2(v) = \sqrt{f^2 + f/g} + f. \tag{90}$$

Since the method is semi-classical, the quantum number v is treated as continuous variable as opposed to a quantum number integer, as is v_{min}. The user defines the mesh size on the variable v, using a non-integer, < 1 mesh size yields a more accurate potential energy curve.

3.3.4 LEVEL

LEVEL[21] is a computer program that takes the two potential energy curves of a transition along with the dipole moment (as a function of bond length) and calculates for the user requested vibrational bands the upper and lower energy limits of the band, the Einstein A, the Franck-Condon factor and the transition dipole moment.

The key function of the program is the determination of the discrete eigenvalues and the eigenfunctions of the radial Schrödinger equation:

$$-\frac{\hbar^2}{2\mu}\frac{d^2\Psi_{vJ}(r)}{dr^2} + V_J(r)\Psi_{vJ}(r) = E_{vJ}\Psi_{vJ}(r), \tag{91}$$

where μ is the reduced mass, v is the vibrational quantum number, J is the rotational quantum number, r is the internuclear distance, and $V_J(r)$ is the electronic potential plus a centrifugal term. The eigenvalues and eigenfunctions of the radial Schrödinger equation are obtained with the Cooley-Cashion-Zare routine [22, 23, 24, 25, 26]. The remaining output parameters are essentially calculated using the equations shown in this text.

CHAPTER 4

SATELLITE SPECTROSCOPY

4.1 ATMOSPHERIC SCIENCE AND SATELLITES

A large constellation of satellites from many different nations orbits the Earth. Many of them are studying the Earth's atmosphere. Many of the satellites studying the Earth's atmosphere use sensors that accomplish some form of spectroscopy.

Climate change has been a prominent global concern for decades. In order to understand climate change, an accurate model of the chemistry and physics of the atmosphere is essential. Such models are only as good as their input data. Much of the essential data needed to understand the Earth's climate is best obtained by satellites. But before climate change was a key issue, atmospheric ozone was the big story. Stratospheric ozone protects the Earth from the Sun's ultra violet rays and is essential to life on Earth as we know it. Stratospheric ozone had been studied long before the impact of human activity on the ozone hole over the Antarctic was documented by Farman et al. in 1985 [27]. In response to concerns over ozone depletion, the UN ratified the Montreal Protocol in 1987, one of the most successful environmental treaties ever enacted. Concern over global depletion of ozone led to launching multiple satellites by multiple nations, able to use spectroscopy to monitor stratospheric ozone. The scientists that designed those satellites were forward thinking and installed sensor suites able to monitor much more than ozone. Some of the satellites in use today and making key findings regarding a wide variety of molecules in the Earth's atmosphere were launched with ozone monitoring as their primary mission.

4.2 EARTH'S ATMOSPHERE

Our atmosphere is in distinct layers. See Figure 17 for a diagram of the Earth's atmosphere showing the layers (excluding the outer exosphere) as well as altitudes, temperatures and pressures. Of primary interest to this work are the lower two levels of the atmosphere, the troposphere and the stratosphere. Note the temperature decreases as altitude increases in the troposphere, and then the trend reverses at the tropopause, somewhere around 12 kilometers in altitude, and then the temperature increases as altitude increases in the stratosphere until the trend again reverses a the stratopause. Key to this work is the study of the

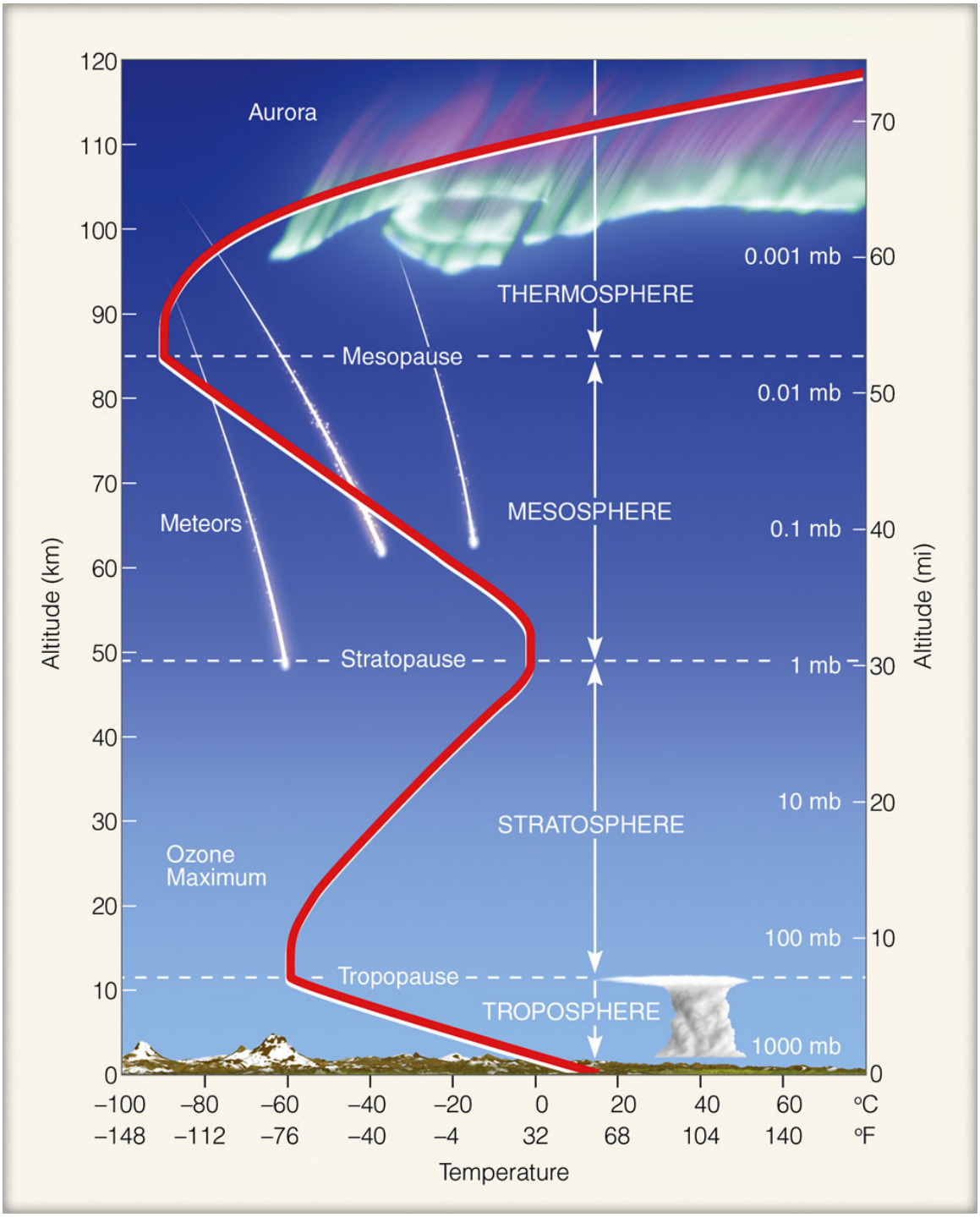

FIG. 17: Earth's atmosphere. Red line is temperature [28].

composition of the stratosphere and the movement of molecules from the troposphere into the stratosphere. The troposphere is turbulent; the stratosphere is stable, molecules reaching the stratosphere tend to stay there for months or years. Air currents in the stratosphere tend to move horizontally; volcanic plumes that reach the stratosphere circle the Earth at roughly the same latitude within a few weeks. There are circulation layers within the atmosphere, see Figure 18 depicting Brewer-Dobson circulation. Note Figure 18 depicts vertical currents rising from the equator into and above the stratosphere and descending at mid latitudes in both hemispheres and at the winter pole.

4.3 SATELLITE REMOTE SENSING

Studying our atmosphere can be done through in situ measurements or remote sensing. In situ measurements are taken by having the instrument taking the measurement at the location where the measurement is taken. For atmospheric science, airplanes and balloons can be launched to the location and altitude of interest and take the measurement, whether that be measuring the pressure or temperature, or actually taking a sample of the atmosphere into the instrument and analyzing it. Airplanes and balloons can reach the stratosphere, but not easily, and typically at significant cost. Remote sensing instruments take measurements without being present at the site the measurement is taken. Telescopes were among the earliest remote sensing scientific instruments. Photography, radar, lidar and in some cases spectroscopy are all methods of remote sensing. Satellites orbiting the Earth use remote sensing instruments to study the atmosphere, with much of the interest focused on the stratosphere. Satellite remote sensors used for atmospheric science typically struggle to reach altitudes well below the tropopause.

Remote sensors from orbit can be broken down into two categories: nadir and limb viewers. Nadir viewing refers to an instrument that looks down, directly toward the Earth's surface. Nadir sensors can effectively cover a wide swath of the atmosphere/Earth's surface, with the instrument sweeping up data along the satellite's path over the Earth. Most Earth viewing satellites have nadir sensors. In general, nadir sensors are poor at vertical resolution. Limb sensors look at a viewing angle allowing a vertical profile of the atmosphere, often described as looking at the edge of the atmosphere. Limb viewing provides much better vertical resolution, but typically with degraded horizontal resolution. See figure 19 for a diagram comparing nadir viewing and limb viewing.

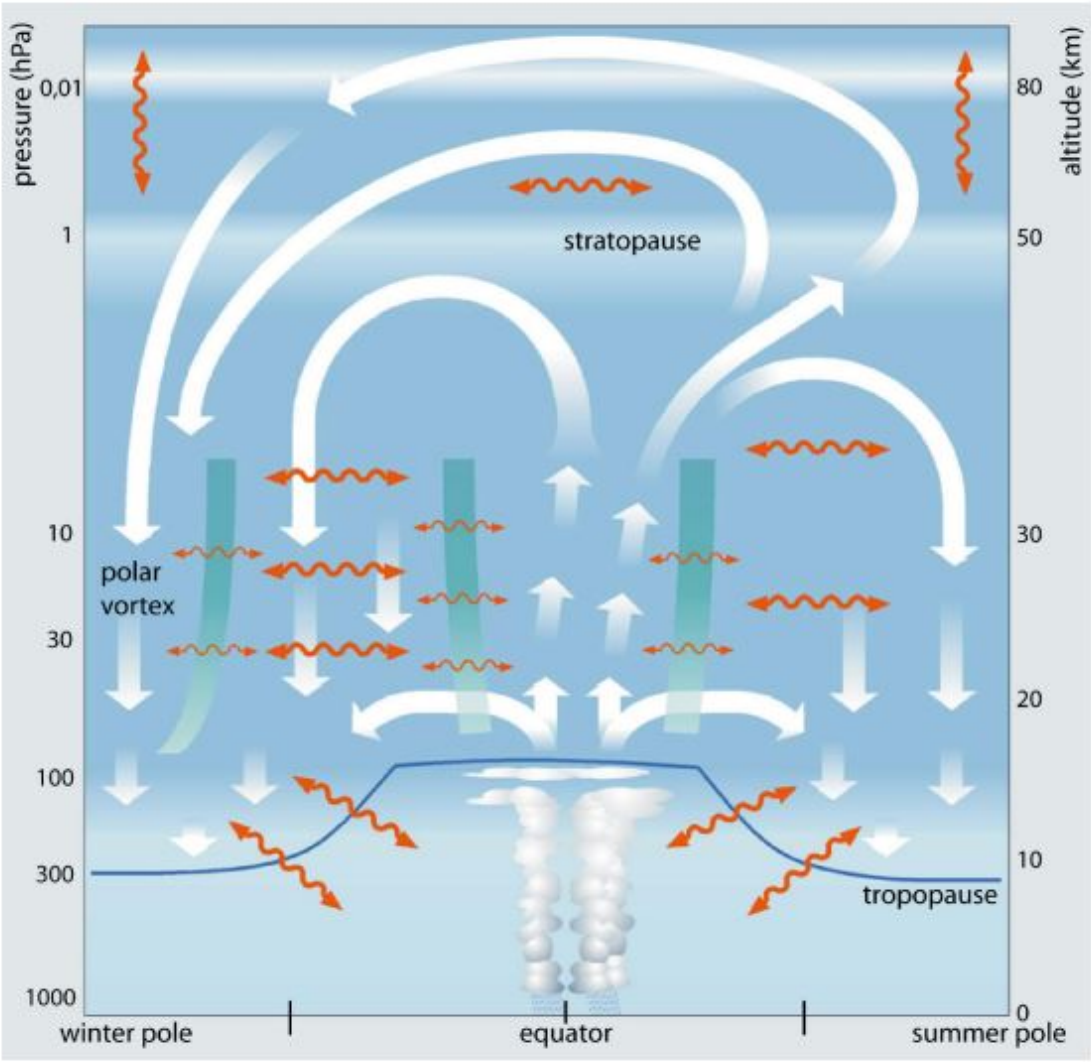

FIG. 18: Brewer-Dobson circulation [29].

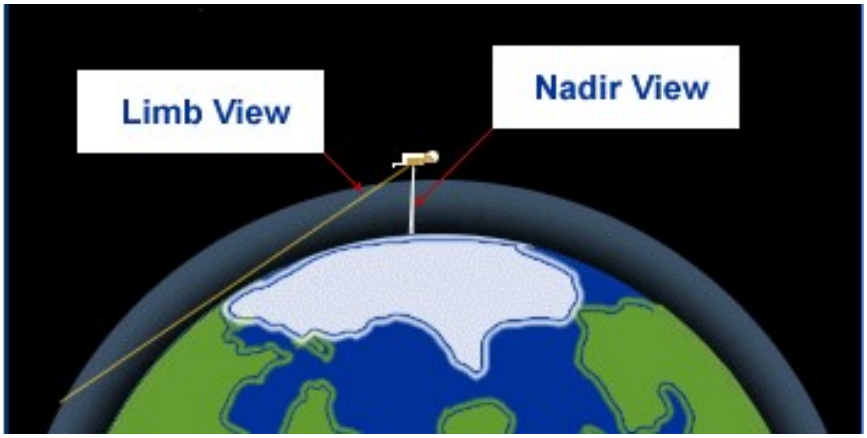

FIG. 19: Nadir vs. Limb viewing [30].

4.4 ACE SATELLITE

All of the data analyzed in this work that was collected by remote satellite sensing is from the Atmospheric Chemistry Experiment (ACE) satellite, also called SCISAT. This section contains an overview of the satellite, focused on the sensor suite. Most of the specifics on the satellite in this section come from Bernath (2017) [31] which provides a detailed description of ACE. Images from the paper are individually cited.

ACE is a Canadian satellite, launched by NASA in August of 2003 and still operating. The orbit is nearly circular, at an altitude of 650 km, inclined 73.9 degrees to the equator. The orbital period is 97.6 minutes. The original primary mission of the satellite was to advance knowledge of the atmospheric chemical and physical processes that impact ozone in the upper troposphere and lower stratosphere (UTLS), with an emphasis on the Arctic region. The instruments make limb observations during solar occultations, meaning the satellite views the limb of the atmosphere with the Sun on the opposite side of Earth providing a known radiation source coming through the atmosphere and into the instruments, essentially looking through the atmosphere into a sunrise or sunset. There are about 30 occultations in a 24 hour period. See Figure 20 for an artist's depiction of an occultation as well as a faithful image of the satellite. The primary instrument on ACE is a Fourier transfrom spectrometer (ACE-FTS). There are also two imagers operating at wavelengths that can find aerosols and clouds by measuring extinction of the solar radiation. The final instrument is a dual optical

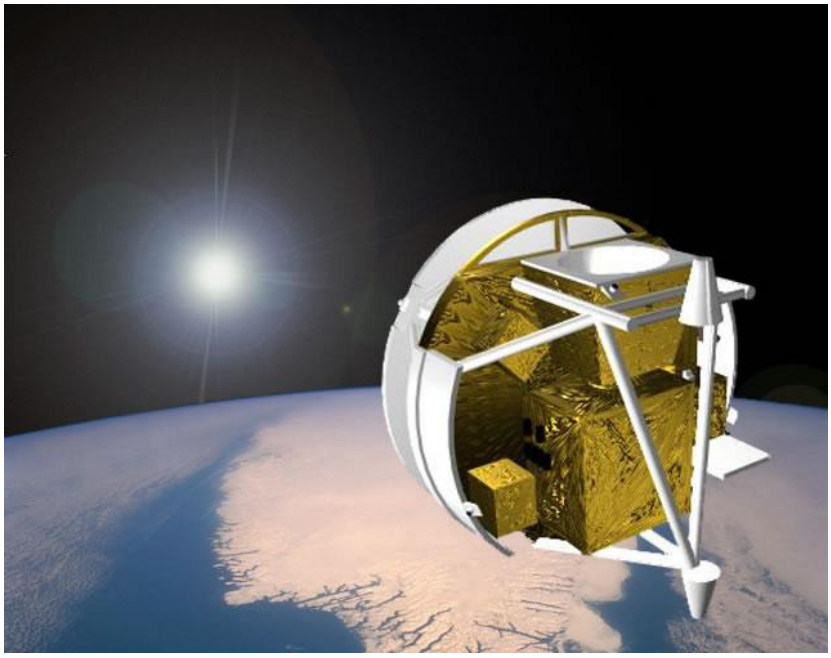

FIG. 20: ACE occultation [32].

spectrophotometer, Measurement of Aerosol Extinction in the Stratosphere and Troposphere Retrieved by Occulation (MAESTRO). MAESTRO data was not used for this research.

The ACE-FTS, the primary instrument on ACE, was designed and built specifically for the spacecraft. See Figure 21 for a schematic diagram of the ACE-FTS Michelson interferometer. Sunlight enters the instrument using a suntracker mirror that points at the center of radiance of the Sun. The radiation is split with a ZnSe beam splitter. To make the instrument more compact, the signal is double passed through the interferometer using the end mirror, then recombined at the beam splitter and passed through a hole in the end mirror to the detector assembly, which has InSb and MCT detectors. The optical path difference is ± 25 cm; the spectral resolution is 0.025 cm^{-1}. The interferograms are sent to Earth using an S-band microwave link and then Fourier transformed. The vertical resolution of the instrument is determined by its field of view, 1.25 mrad, which works out to 3-4 km of the atmosphere. The vertical measurement sampling is determined by three factors: atmospheric refraction, the angle between the orbit plane and the Earth-Sun vector (beta angle), and the 2 seconds of time needed to record a spectrum. When the beta angle is small, the satellite sees nearly vertical Sun motion, as the beta angle increases the Sun's path becomes more

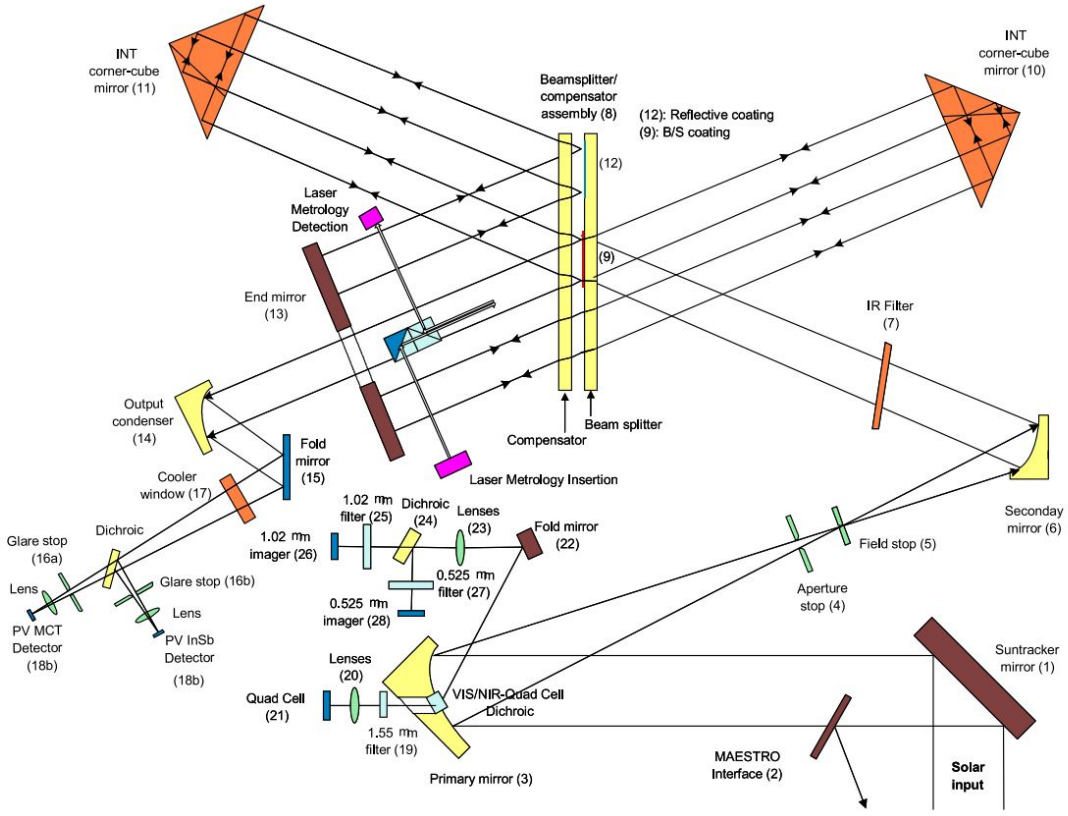

FIG. 21: ACE-FTS Michelson interferometer [31].

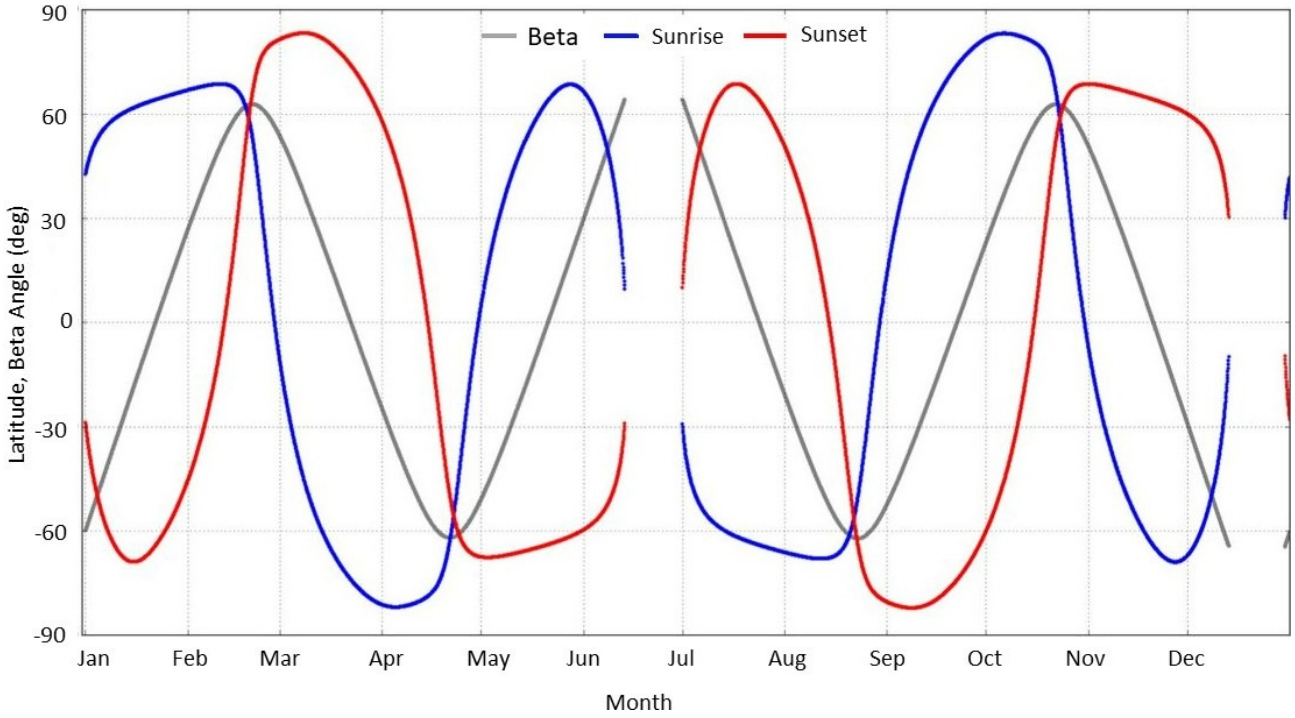

FIG. 22: Latitude and beta angle of ACE occultations over a year [31].

slanted. A small beta angle yields a vertical sampling of about 6 km, a large beta angle (on the order of 55°) results in vertical sampling of about 2 km. Figure 22 shows the latitude of ACE occultations over a one year period as well as the beta angle. The latitude of the orbit repeats annually, the longitude does not.

There are two filtered solar imagers within the ACE-FTS instrument, which are not directly involved in ACE-FTS data processing. One of the imagers operates in the visible range, with its filter centered at a wavelength of 0.525 μm; the other imager operates in the near IR range, with its filter centered at 1.02 μm. In Figure 21 the imagers are shown just above the primary mirror at the bottom of the diagram. The filters support the ACE-FTS by verifying the presence of clouds in the field of view. For this research, the 1.02 μm was used to detect the presence of aerosols.

CHAPTER 5

SULFUR DIOXIDE FROM THE ATMOSPHERIC CHEMISTRY EXPERIMENT (ACE) SATELLITE

The findings and most of the material presented in this section are published in the Journal of Quantitative Spectroscopy & Radiative Transfer (Cameron et al.[33]). The co-authors of the paper are Peter Bernath (Old Dominion University) and Chris Boone (University of Waterloo). Chris Boone is the ACE Project Scientist and Co-Principal Investigator; he performed the data retrievals using University of Waterloo resources and offered some insights into how the data analysis might proceed. Peter Bernath is the ACE Mission Scientist, FTS Principal Investigator and the advisor on this project, to include making edits to the paper. I am the corresponding author, I did the data analysis, generated all the figures and wrote the text of the paper. This work is original and was not published anywhere prior to its publication in the Journal of Quantitative Spectroscopy & Radiative Transfer.

5.1 INTRODUCTION

"Sulfur dioxide is one of the primary gases associated with atmospheric aerosol formation [34]. Sulfate aerosols significantly impact the climate through scattering and absorption of solar radiation, as well as serving as cloud condensation nuclei [35]. The global distribution of SO_2 VMRs, resolved by altitude and latitude, including volcanic activity, helps quantify the role SO_2 plays in the Earth's atmosphere.

There are two primary sources of atmospheric SO_2: human activity and volcanic eruptions, with volcanic eruptions being the primary mechanism for SO_2 injection into the lower stratosphere. Human activity has resulted in notable changes in SO_2 production over the last two decades [36]. SO_2 produced by human activity typically reaches no higher than the tropopause. The potential exists for anthropogenic SO_2 to occasionally reach the stratosphere in conjunction with the monsoon phenomena; however, the contribution to stratospheric SO_2 appears to be minor [37]. Volcanic activity can inject SO_2 into the stratosphere as well as the troposphere; but volcanic eruptions that inject significant amounts of SO_2 into the stratosphere are rare, on the order of five to ten eruptions a year [38]. Yet the volcanic

contribution to the entire atmospheric SO_2 budget is significant; while volcanic emissions may only make up 10% of the global SO_2 source to the atmosphere, due to the longevity of SO_2 and aerosols in the stratosphere they contribute as much as 26% of the SO_2 burden, and are responsible for 14% of the sulfate aerosol burden [39].

In the troposphere, the primary sinks for SO_2 are gas phase oxidation by reaction with OH and aqueous phase oxidation within cloud droplets by reaction with H_2O_2 or O_3 [40]. Ultimately tropospheric SO_2 returns to the surface from the troposphere in a matter of days or weeks in precipitation. In the stratosphere SO_2 eventually oxidizes and ends up in sulfate aerosol, slowly sinking due to gravity with sedimentation velocities on the order of 100 m/month. Stratospheric SO_2 in non-oxidized molecular form is much more persistent than in the troposphere, often remaining confined in latitude bands for one to two months after a volcanic eruption and staying aloft in the stratosphere for several months [41]. A single large volcanic eruption can have a climactic impact lasting 2-3 years [42]." [33]

There have been noteworthy previous efforts to investigate stratospheric SO_2 by remote satellite sensing. This research is distinguished by its scope both in determining background SO_2 levels by altitude and latitude on a global scale and in the number of volcanic plumes studied.

"Nadir viewing sensors can collect data across a wide swath; the Ozone Monitoring Instrument (OMI) on the Aura spacecraft has shown the ability to reliably map anthropogenic SO_2 sources on the Earth's surface that produce 70 kT y^{-1} or more [43] as well as passive (non-erupting) SO_2 flux from volcanoes [44]. The Tropospheric Monitoring Instrument (TROPOMI) aboard the Sentinel 5 Precursor satellite has improved on OMI [45]. In general, nadir sensors are unable to resolve observations by altitude; there are notable exceptions such as Yang et al. [46].

Limb sounders can provide a global distribution of SO_2 concentrations resolved by altitude and location, although the geometry of limb observations requires multiple passes to cover the area that a nadir observer can cover in one pass, and if observations at a specific location at a specific time are desired this may not be possible. The Microwave Limb Sounder (MLS) instrument on the Upper Atmosphere Research Satellite (UARS) made a comprehensive plot of the SO_2 plume from the eruption of Mount Pinatubo in the Phillipines in 1991, including tracking the decay of SO_2 levels for a period of about six months after the eruption [41]. The next MLS generation on the Aura satellite has demonstrated the ability to track volcanic SO_2 plumes with VMRs greater than 400-500 ppt [47]. The Michelson Interferometer for Passive Atmospheric Sounding (MIPAS) [48], a limb sounder on the Envisat satellite, produced an

TABLE 1: Microwindow list for SO_2 [33].

Center Freq (cm^{-1})	Microwindow Width (cm^{-1})	Lower Alt (km)	Upper Alt (km)
1357.44	0.35	9	24
1359.47	0.30	9	18
1361.81	0.45	12	24
1370.18	0.55	10	24
1371.45	0.50	10	24
1376.95	1.30	12	24

SO_2 data product similar to ACE-FTS and direct comparisons have been made. MIPAS ceased operation on 8 April 2012.[33] "

5.2 OBSERVATIONS AND RETRIEVALS

The data analyzed for this research is version 4.0 of ACE-FTS processing, which was the first version to include SO_2 data. There are over 40 molecules and related isotopologues in the dataset. Isotopologues are molecules with the same atomic structure but have at least one atom that is not the same isotope. Specific molecules are located among the data retrieved using microwindows, which are key features in the spectrum of the molecule that uniquely identify it.

"For the data set retrieved for version 4.0 of ACE-FTS processing [49], the SO_2 microwindows are provided in Table 1. Version 4.0, released in March 2019, uses spectroscopic line parameters from the HITRAN 2016 database [50]. Interferers in this microwindow set whose VMR profiles were retrieved simultaneously were the isotopologuees HDO, ^{18}OCO, and $^{13}CH_4$. VMR profiles for all other interferers were fixed to the results of previous retrievals. Version 4.0 SO_2 data are provided between 9.5 and 23.5 km in 1 km increments. The lower altitude is limited by interfering molecules such as water and methane; the upper altitude is limited by signal-to-noise ratio. The ACE-FTS altitude resolution in this range is typically about 2.5 km. Due to high relative statistical errors (SO_2 VMR error/SO_2 VMR) for observations at lower altitudes, the plots shown begin at 11.5 km where typical fractional

errors on the order of 5 sharply drop to about 0.7, gradually increasing to a maximum of about 1.5 at 20.5 km, decreasing above 20.5 km to about 0.9 at the top of the altitude range.

ACE SO_2 data, February 2004 to December 2019, were used. This paper describes two studies of the ACE SO_2 observations: (1) a quantification of the typical background abundances of SO_2, and (2) an examination of volcanic SO_2 plumes. The altitude range of interest is the Upper Troposphere/ Lower Stratosphere (UT/LS), because of high concentrations of stratospheric aerosols [51]. High SO_2 concentrations from significant volcanic eruptions show up as anomalous data, so the first step was to find a filter/discriminator to differentiate between normal background SO_2 and volcanic plumes. Empirically, a 3 Median Absolute Deviation (MAD) was found to be suitable. [33]"

The MAD is:

$$\text{MAD} = \text{median}(|X_i - \tilde{X}|) \tag{92}$$

where X_i are the data points and $\tilde{X}$ is the median of the data.

"Data within 3 MADs are likely are likely to be background SO_2; any data beyond 3 MADs are likely of volcanic origin or non-physical. Non-physial data points appeared in the data set, showing obvious discontinuities when comparing datapoints within the same data bin. Such points were manually deleted. Deletion of data points only occurred within the bins used to plot SO_2 VMR or extinction in volcanic plumes. A data bin is defined here as the data points over a one-month time period at a specific latitude (5° wide) and altitude (1 km high). The plotted data at a given altitude and latitude is the mean of the corresponding data bin. Only individual points in a bin, not the entire bin were deleted. A month of data is on the order of 500 occultations. (Dissertation note: The previous sentence is from the quoted paper, on the average month there are roughly 895 occultations.) In total 16 occultations had data points manually deleted; in each case only the data at one or occasionally two altitudes were deleted, not the entire occultation." [33]

The ACE-FTS Imager filtered to observe solar radiaton at 1020 nm was used to determine aerosol extinction in conjunction with volcanic plumes. Other than the 1020 nm filter, there was no filtering or further processing of the data. The data was simply sorted into bins in the same method as the SO_2 data and then the mean of the data in each bin was taken. In isolated cases individual observations that were clearly outliers were manually deleted.

5.3 RESULTS AND DISCUSSION

"Figure 23 is the mean of all background SO_2 data, resolved by altitude. Data from an ACE-FTS research product (generated prior to v4.0 used in this study) were employed in a

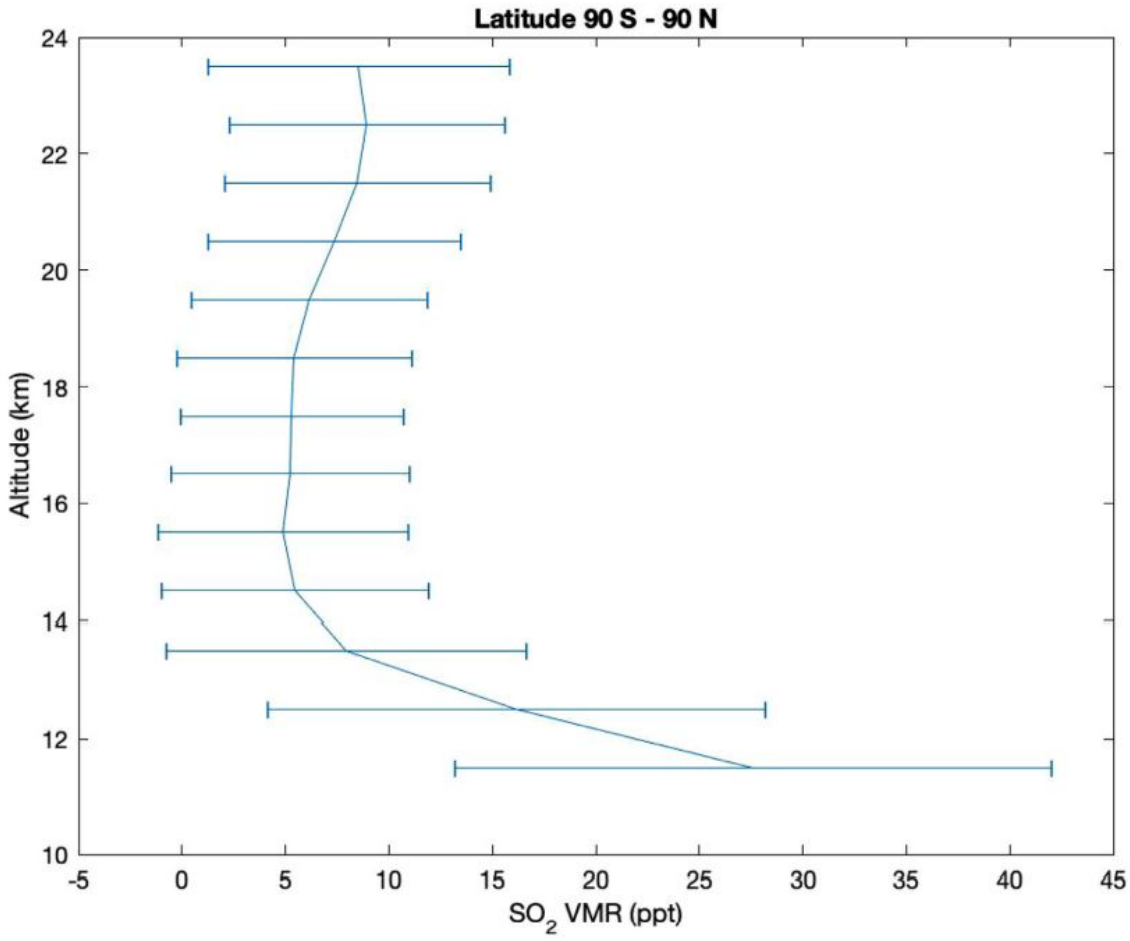

FIG. 23: Mean SO_2 VMR resolved by altitude, horizontal bars show 1 standard deviation [33].

study by Rollins et al. [52] who found agreement within 10-15 ppt compared to results from MIPAS. Figure 3 from that paper compared ACE-FTS results to aircraft in situ measurements taken by NASA's VIRGAS experiment (Volcano-plume Investigation Readiness and Gas-phase and Aerosol Sulfur), showing agreement within 5 ppt.

Given the variability of the tropopause by latitude, the data of Figure 23 can be broken down into latitude zones. Figure 24 divides the data from Figure 23 into 30° latitude zones. The plots covering from the equator to 30° North or South are almost identical, both showing an increase in SO_2 VMRs as the altitude increases above 20 km. The remaining plots are similar above 14 km, but the Northern Hemisphere clearly shows higher concentrations of SO_2 in the upper troposphere between 10 and 14 km, highlighting the presence of major anthropogenic sources from North America, Europe, the Middle East and China.

Figure 25 is the mean of all background SO_2 data, resolved by altitude and latitude, with volcanic activity filtered out through a 3 MAD filter. The highest concentration is about 35 ppt, which occurs in the upper troposphere in the 30°N-60°N latitude range. A similar plot was provided by Höpfner et al. [48] based on bias corrected MIPAS data. Höpfner et al. also see enhanced SO_2 near the equator above 18 km.

Fig. 26 resolves global background SO_2 VMRs by altitude, latitude and season. Similar MIPAS results show some seasonality; specifically, MIPAS shows the summer VMR at 10 km altitude is 80-100 ppt in the mid and upper northern latitudes; this anomaly is inconsistent with the ACE data depicted in Fig. 26. Both MIPAS and ACE show the VMR decreasing as altitude increases with the lower layer gone by around 16 km, and then the VMR is constant at around 10 ppt. Note the seasonality to Fig. 26: in Jun-Aug a slightly higher concentration of SO_2 forms at 24 km near the South Pole and persists into Sep-Nov; in Dec-Feb a slightly higher concentration of SO_2 forms at 24 km near the North Pole and persists into Mar-May. We suspect these phenomena are due to descending air within the polar vortex. The suspected source of the SO_2 enhancement is atmospheric OCS. There is an enhancement feature above 22 km near the equator. Some research data retrievals indicate this SO_2 enhancement to be the bottom of a larger, higher feature. Future ACE-FTS data processing will explore this topic. In Jun-Aug and Sep-Nov, a slightly higher concentration of SO_2 spans the equatorial region at 13-14 km.

The hunt for volcanic SO_2 plumes began by studying the Smithsonian Institution's, Global Volcanism Program webpage at http://volcano.si.edu [38]. The search focused on volcanic emissions where the SO_2 plume reached 10 km or more in altitude. Those volcanic eruptions where the SO_2 plume height met or exceeded 10 km and the mass of SO_2 emissions

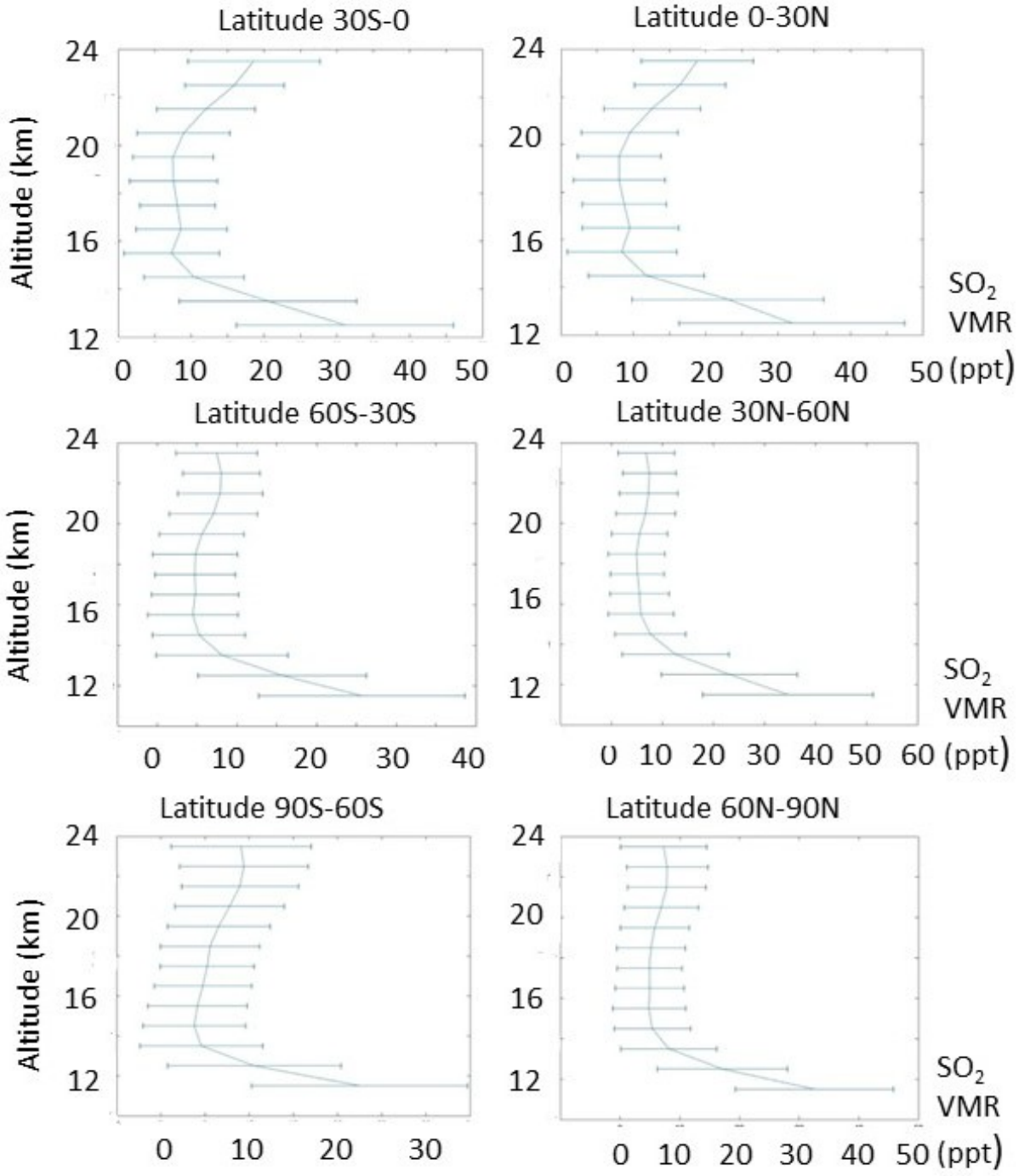

FIG. 24: Mean SO_2 VMR resolved by altitude, horizontal bars show 1 standard deviation [33].

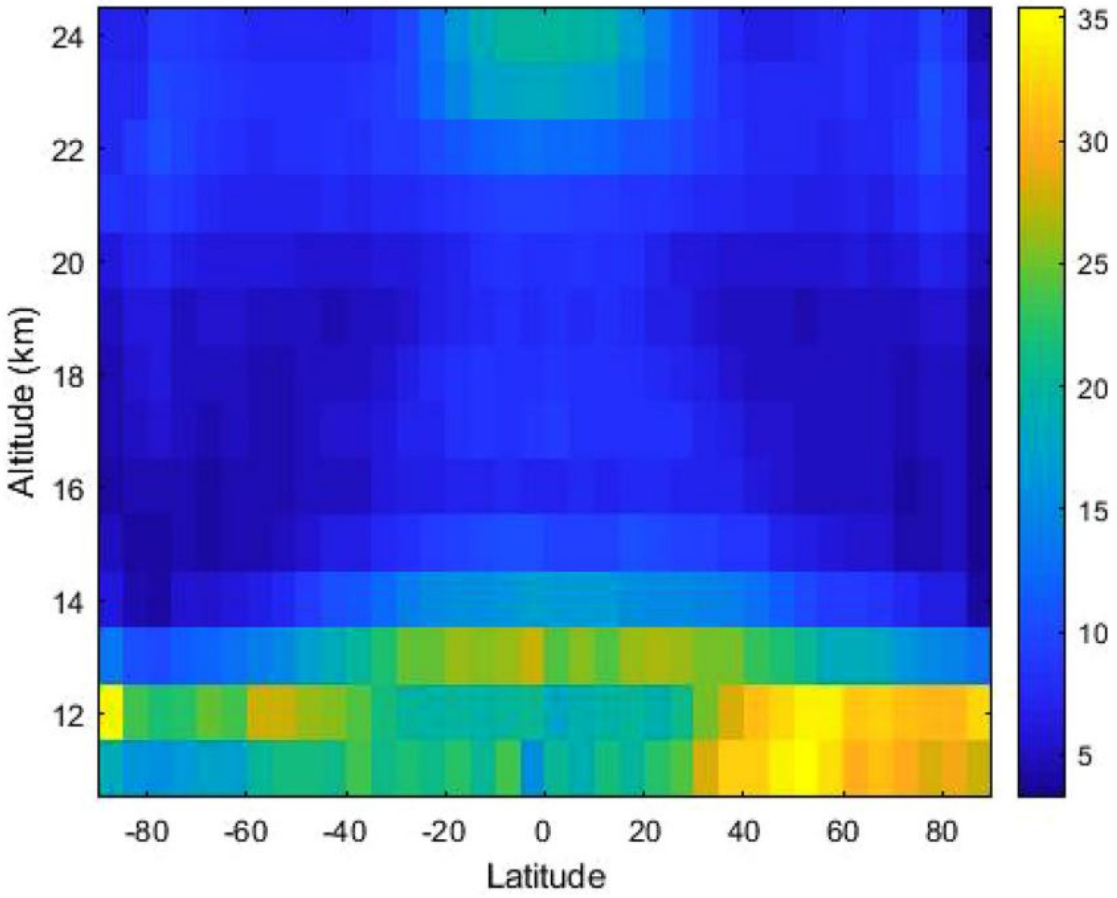

FIG. 25: Mean SO_2 VMR (in ppt) resolved by altitude and latitude [33].

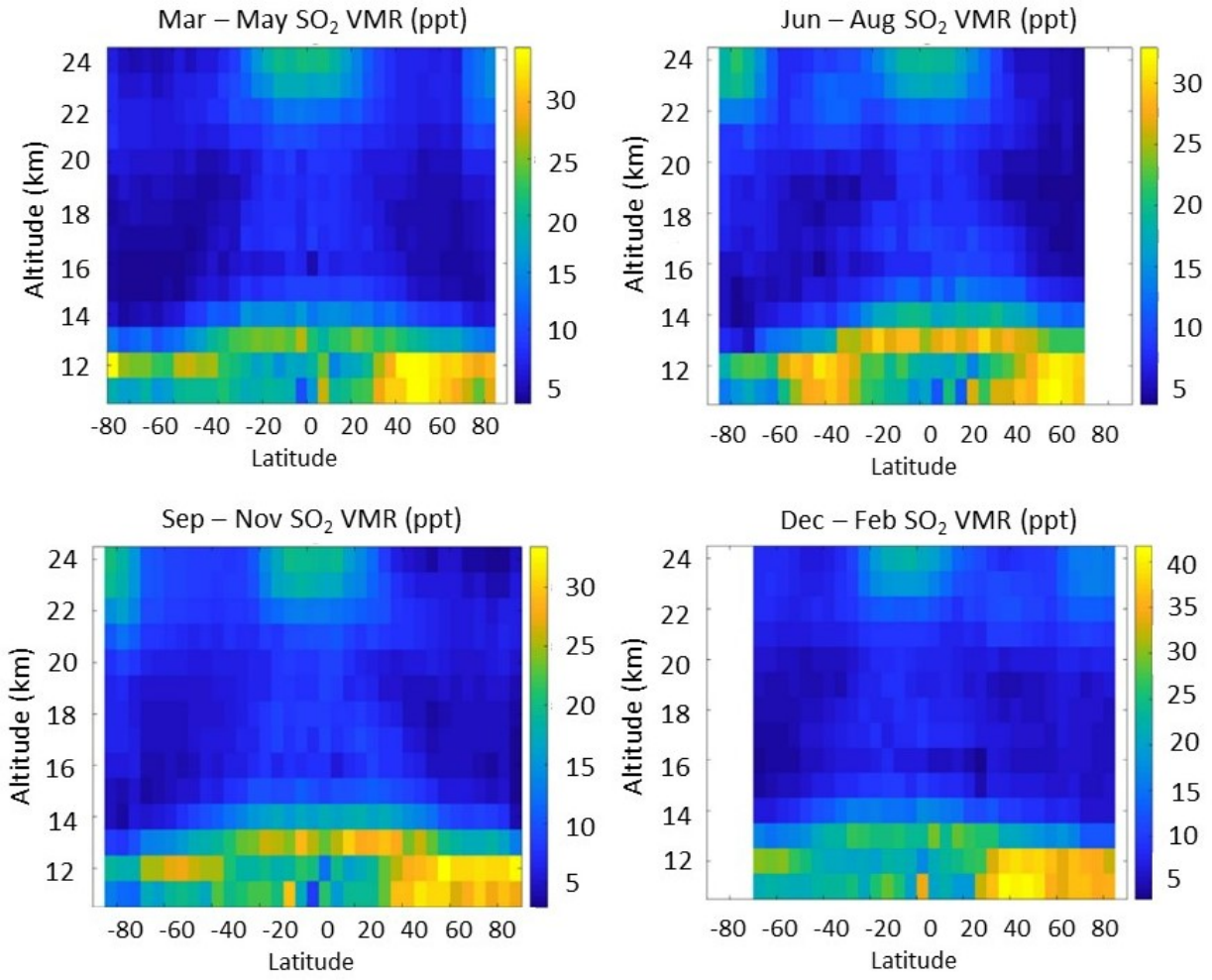

FIG. 26: Seasonal mean SO_2 VMRs (in ppt) resolved by altitude and latitude [33]. Note: Top left Mar-May, top right Jun-Aug, bottom left Sep-Nov, bottom right Dec-Feb.

TABLE 2: Volcanic SO_2 plumes detected by ACE [33].

Volcano Name	Lat/Long	Eruption Date	SO_2 (kt)	Plume (km)
Manam	4.1°S, 145.0°E	27 Jan 2005	140	24
Rabaul	4.3°S, 152.2°E	7 Oct 2006	300	18
Okmok	53.4°N, 168.1°W	12 Jul 2008	150	15
Sarychev	48.1°N, 153.2°W	12 Jun 2009	1200	17
Grimsvotn	64.4°N, 17.3°W	21 May 2011	300	12
Puyehue-Cordon Caulle	40.6°S, 72.1°W	4 Jun 2011	200	14
Nabro	13.4°N, 41.7°E	13 Jun 2011	3650	18
Kelut	7.9°S, 112.3°E	13 Feb 2014	200	19
Calbuco	41.3°S, 72.6°W	22 Apr 2015	400	20
Raikoke	48.3°N, 153.3°E	22 Jun 2019	1500	23

met or exceeded 80 kt are typically visible in a plot of SO_2 VMR resolved by altitude and latitude. At the time of writing 113 (dissertation note: 113 is a typographical error in the published paper; 37 eruptions met both criteria) volcanic eruptions in the Smithsonian database met both criteria. For reference, the average SO_2 emission for the 113 volcanoes with SO_2 plume heights at or beyond 10 km is 421 kt; 37 out of the 113 eruptions exceed 80 kt. The final discriminator in locating a specific volcanic plume is whether the ACE-FTS measured near the plume latitude between the time of eruption and about 2 months afterwards. For example, the eruption of the Kasatochi volcano in August of 2008 in Alaska's Aleutian Islands produced about 2000 kt of SO_2 with a plume height of 15 km, but was not viewed by ACE occultations. The 10 eruptions that meet all the preceding criteria, including timely and nearby ACE occultations, are listed in Table 2.

In order to obtain enough limb observations to observe a volcanic plume, one month of data are used. Plumes from the larger eruptions were clearly visible two months after the eruption. Local VMRs in the 500–1000 ppt range are typical for the eruptions depicted. The latitudes of the plumes match the latitudes of the eruptions with slight shifts becoming more pronounced over time. Plume altitudes in Table 2 are in general agreement with the

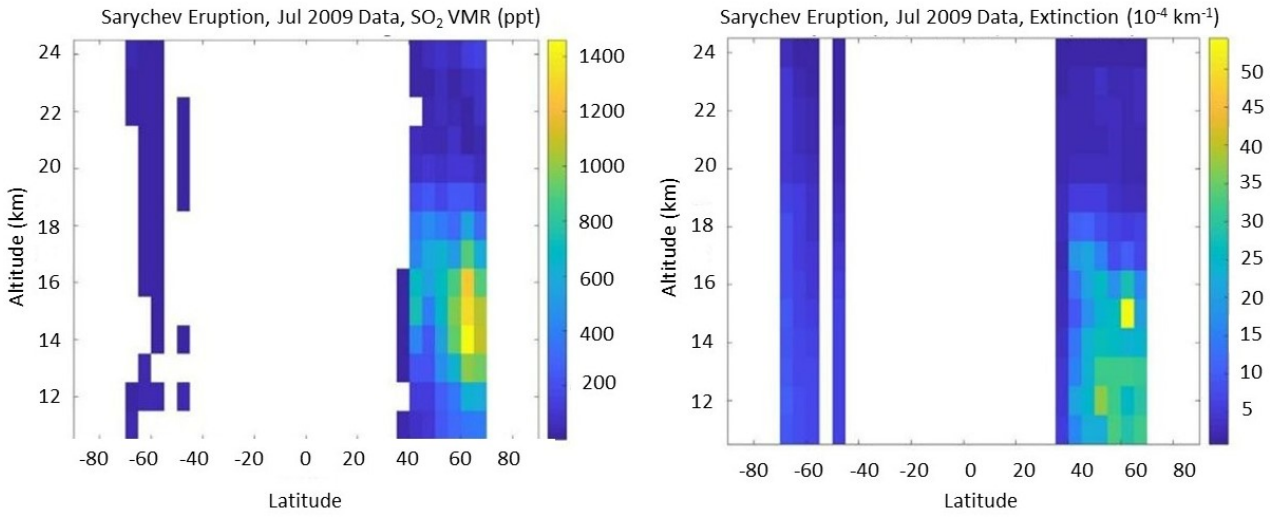

FIG. 27: Sarychev volcano eruption [33].

Note: Eruption occurred 12 Jun 2009 at 48.1°N, 153.2°W; July 2009 data shown. Left SO_2 VMR; right aerosol extinction.

altitudes from the Smithsonian database. To the right of each SO_2 plot is a similar plot of the atmospheric extinction from the near infrared imager at 1020 nm for the same time period. The altitude−latitude distribution plot showing the Sarychev volcanic eruption is shown in Fig. 27 for July 2009.

In Fig. 28 are three altitude-latitude plots for the Raikoke volcanic eruption, located in Russia's Kuril Islands. It erupted on 22 Jun 2019 and made a large, persistent signature in the ACE-FTS data. The first plot is for July 2019; the second shows data from September 2019. Raikoke's June 2019 eruption is chronicled in the Smithsonian database. The estimated plume height shown in the table is based on ACE-FTS data. It shows that the SO_2 plume from a large eruption can remain visible for two to three months after eruption. Because of ACE's orbit no suitable occultations are available in Fig. 28 for August.

The Raikoke eruption was observed by ACE for 4 months. These observations afford the opportunity to evaluate the decay of the SO_2 plume. As shown by McKeen et al. [53], the reaction that controls the conversion rate of SO_2 to sulfuric acid (H_2SO_4) in the stratosphere is

$$SO_2 + OH \xrightarrow{M} HSO_3. \tag{93}$$

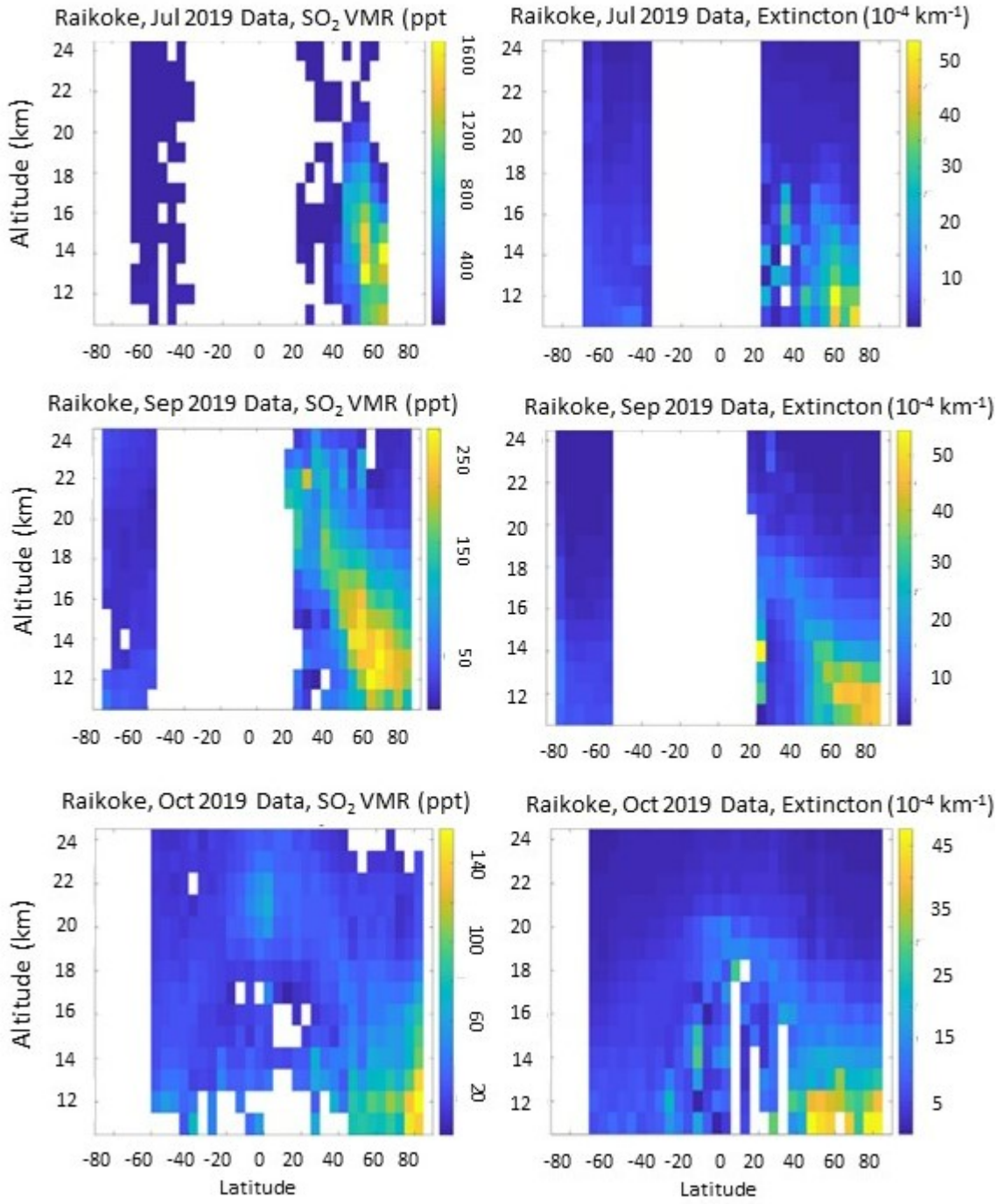

FIG. 28: Raikoke erupted on 22 Jun 2019 at 48.3°N, 153.3°E; the SO_2 plume drifted to 80°N by September 2019 [33].

Note: Left column SO_2 VMR, right column aerosol extinction. Top row Jul 2019 data, middle row Sep 2019 data, bottom row Oct 2019 data. Note the Ulawun volcano erupted at 5.05°S 151.33°E between June and Oct 2019 but does not significantly appear in the plots.

From this reaction the SO_2 decay rate can be approximated:

$$\frac{\mathrm{d}[SO_2]}{\mathrm{dt}} = -k[SO_2][OH][M], \tag{94}$$

where the square brackets denote number density: M is the total number density and k is a temperature dependent rate constant [53]. For constant [OH] and [M] pseudo-first order kinetics are obtained. For the Raikoke SO_2 plume, the portion of the plume at 14 km altitude between 55°N and 60°N appears relatively stationary and was used to make a rough estimate of the e-folding time of about 27 days. While only a rough estimate, this number compares well with similar calculations made by Read et al. using data from MLS and UARS on the 1991 Mt. Pinatubu eruption [41], 33 days, as well as those made by Pumphrey et al. using data from MLS on Aura for multiple volcanic eruptions between 2005 and 2014, 24 days and an uncertainty of 3 days [47].

Using extinction data from its Imager, ACE also provides the data to determine the decay of H_2SO_4 aerosol cloud for the same time period:

$$\frac{\mathrm{d}[H_2SO_4]}{\mathrm{dt}} = k_{SO_2}[SO_2] - k_{H_2SO_4}[H_2SO_4]. \tag{95}$$

Using the same latitude/altitude section as used for determination of decay of SO_2 yields the approximate e-folding time for the H_2SO_4 aerosol cloud to be about 111 days. As the aerosol cloud is fed by the decaying SO_2 plume, the concentration of H_2SO_4 increases for about 50 days and then begins to decrease." [33]

5.4 CONCLUSION

"The ACE mission has more than 16 years of SO_2 data that spans many significant volcanic eruptions and provides a large data set from which to derive background SO_2 atmospheric data. Background SO_2 VMRs are in the 30 ppt range at altitudes between 10 and 14 km and then fall to less than 10 ppt as altitude increases. SO_2 VMRs in the upper troposphere are consistently 5 to 10 ppt higher above 30° latitude in the Northern Hemisphere in comparison to the Southern Hemisphere. Some seasonality has been measured, primarily in the polar and equatorial regions. Volcanic SO_2 plumes can persist for up to three months. Extinction data for sulfate aerosols from the ACE mission has been used to corroborate the detection of volcanic plumes."[33]

5.5 APPENDIX NOTE

"ACE offers simultaneous observations of both SO_2 plumes and sulfate aerosol distributions in the form of extinction plots. Additional volcanic eruptions from Table 2 with SO_2 VMR plots shown beside extinction plots for the same time period for comparison are included in the Appendix. Each figure caption includes the latitude of eruption as well as the month the data was taken from (typically one or two months after the eruption)." [33] (See Appendix A).

CHAPTER 6

SATELLITE CHARACTERIZATION OF GLOBAL STRATOSPHERIC SULFATE AEROSOLS RELEASED BY TONGA VOLCANO

The findings and most of the material presented in this section are published in the Journal of Quantitative Spectroscopy & Radiative Transfer (Bernath et al.[54]). Peter Bernath is the corresponding author and coordinator of co-author efforts, the ACE Mission Scientist and FTS Principal Investigator. The co-authors of the paper are Chris Boone (University of Waterloo), Adam Pasotorek (Old Dominion University), me, and Mike Lecours (University of Waterloo). Chris Boone is the ACE Project Scientist and Co-Principal Investigator; he performed the data retrievals using University of Waterloo resources and did some initial investigating into retrieval results. Adam Pastorek is a post doctoral researcher on the Bernath research team and was the lead developer of the multiple linear regression model, working with Chris Boone. The model was used to explore the composition of the Tunga aerosols and generate the figures that depict aerosol composition. I wrote and executed the computer programs used to probe ACE-FTS data, specifically looking for trends in aerosols, $ClONO_2$, O_3, and HCl. Only the aerosol data made it into the paper. I also generated the graphic showing the location of ACE occultations for 2021. Mike Lecours provided data curation. Everyone assisted in review/ editing. All the figures and tables in this section are from the paper and cited accordingly. This work is original and was not published anywhere prior to its publication in the Journal of Quantitative Spectroscopy & Radiative Transfer.

6.1 INTRODUCTION

The role of SO_2 and the sulfate aerosols it generates in the stratosphere are discussed in section 5.1. In addition to the cooling effect stratospheric sulfate aerosols have on the climate, they also impact stratospheric ozone. The exceptionally large Mount Pinatubo eruption in the Phillipines in 1991 decreased stratospheric ozone by 3-4% [55]. As mentioned in section 5.1, sulfate aerosols act as seed particles for clouds, of particular interest to this research is that they specifically seed Polar Stratospheric Clouds (PSCs), which are key to the formation of the Antarctic ozone hole [51]. The eruption of large tropical volcanoes has

been shown to impact stratospheric circulation patterns; the stratospheric heating increases the temperature gradient between the equator and the pole, causing a stronger than normal polar vortex [56]. Aerosols are important in climate modelling, currently modelling their role is incomplete; smaller error bars brought about by better understanding of aerosols would be beneficial [57].

The Hunga Tonga-Hunga Ha'apai volcano, referred to in this research as simply Tonga, is located under water at 20.54° S 175.38° W. It erupted on 15 Jan 2022. There were two key factors that made the eruption so significant: (1) the plume reached an exceptional height of 57 km [58] [59] , and (2) a large amount of water vapor was injected into the stratosphere [60] [61], causing a cooling effect [62] [63].

While the underwater eruption of Tonga resulted in an unusually large amount of water in the plume, the amount of SO_2 was a much more modest 410 kt [60], slightly above average in comparison to the eruptions shown in Table 2. The water vapor significantly decreased the SO_2 lifetime to about 12 days, which can be compared to the more typical 27 days calculated for the Raikoke eruption in section 5.1; the result was a rapid conversion to sulfate aerosol [64]. Using the OMPS LP (Ozone Monitoring and Profiler Suite, Limb Profiler) instrument aboard NASA's Suomi NPP (National Polar-orbiting Partnership) satellite, Taha et al. [65] found the Tonga eruption caused the largest stratospheric optical depth since the eruption of Mount Pinatubo in 1991.

There are several characteristics of stratospheric sulfate aerosols that determine their impact on the climate, including: particle number density, particle size distribution, average particle size, and particle composition [54]. Large particles (effective radii $> 2\ \mu$m) can cause global surface heating instead of global surface cooling [66]. Particle composition (meaning weight percentage of sulfuric acid) impacts sunlight extinction and absorption of thermal radiation from Earth. Particle composition [51] is generally assumed to be 75% H_2SO_4; this research shows the number varies from 45% to 79%. Due to its effect on infrared aerosol extinction [67], assuming a constant 75% H_2SO_4 particle composition causes a significant systemic error in modeling stratospheric heating by sulfate aerosols. Particle composition also has an impact on optical constants used to model scattering in the visible region [68], so assuming it to be a constant has yet another detrimental impact on climate modelling as well as lidar, limb scattering, solar occultation and nadir retrievals of sulfate aerosol properties.

6.2 METHODS

"ACE-FTS spectra are processed on the ground [70] to provide concentration profiles as a

function of altitude for 44 gaseous molecules [71] for version 4.1/4.2. The absorption features due to these molecules can be removed from the spectra to create "residual" spectra that contain broad features due to cloud and aerosol particles [69]. These residual spectra contain some artefacts, for example from molecules such as HNO_3 for which the experimental line lists are incomplete. Thus, each spectrum is divided by a suitable reference spectrum that does not contain the volcanic plume but does contain background sulfate aerosol contributions. The background sulfate aerosol contributions in these reference spectra are removed by fitting. The final, corrected residual spectrum therefore has artefacts largely removed, and sulfate contributions from both the background and the volcanic eruption.

Simulation of these characteristic spectra can provide information on composition, particle size and particle shape. For example, transmittance spectra of Polar Stratospheric Clouds (PSCs) have shown that binary nitric acid and water particles (supercooled nitric acid, SNA) are common in addition to nitric acid trihydrate (NAT), supercooled ternary solutions of nitric acid and sulfuric acid (STS), and ice [72]. The sulfate aerosols from the Raikoke volcanic eruption have also been characterized using residual ACE-FTS spectra [67]."[54]

Boone et al. [67] describes how the ACE-FTS is used to retrieve sulfate aerosol properties. A slightly modified Beer-Lambert equation from the versions previously shown in equations (38)-(40) is used:

$$\tau = Ae^{-\sigma_{ext}Nl} = Ae^{-\alpha l}, \tag{96}$$

where A is a baseline parameter fitted to improve agreement with ACE spectra, σ_{ext} is the extinction cross section (which includes both absorption and scattering), N is particle concentration, l is the path length and α is the extinction coefficient. The extinction coefficient was calculated using Oxford University's Mie scattering code for spherical particles (http://eodg.atm.ox.ac.uk/MIE/index.html).

The extinction cross section is dependent upon wavenumber, particle size distribution and optical constants of the material at the ambient temperature. Temperatures were taken from the ACE-FTS retrievals.

The particle size distribution was determined by a log normal distribution:

$$n(r) = \frac{N}{\sqrt{2\pi}} \frac{1}{\ln(S)} \frac{1}{r} \exp[\frac{(\ln(r) - \ln(r_m))^2}{2\ln^2(S)}] \tag{97}$$

where r_m is the median radius and $\ln(S) = \sigma$ with σ being the distribution standard deviation. The value of S was not directly obtainable because the distribution width can not be obtained from only infrared data; after some preliminary sulfate aerosol retrievals including coincident ACE infrared data and and optical SAGE III/ISS extinction data from the

Raikoke volcanic eruption, S was fixed to 1.3. The aerosol path length l is also unknown; the column density Nl was determined in the fit. The optical constants are based on values from Lund Myhre et al. [73]. In summation, the observed transmittance spectra were fitted by floating four parameters: the baseline A, the median radius r_m, the particle composition (weight percentage of sulfuric acid), and the column density Nl.

6.3 RESULTS AND DISCUSSION

The ACE satellite occultations were not in a location to intersect the Tonga plume until about 4 Feb 2022. Figure 29 shows the aerosol extinction from the 1.02 μm imager. A reference occultation with no volcanic plume is included for comparison. Figure 30 shows the residual stratospheric transmittance spectrum at 23.1 km for the same occultation shown in Figure 29. The median radius r_m was determined to be 0.323 $\pm$ 0.0002 μm, the particle composition (weight percentage of sulfuric acid) 62.5 $\pm$ 0.2 %, and the column density Nl 5.2 $\pm$ 0.1 x 10^8 particles/cm^2 [70]. The retrieved temperatue was 212.5 K.

"The latitude of the Tonga plume was tracked with the 1.02 μm ACE imager. During February 2022 the plume was located between 30°S and 10°N latitude and by April 2022 covered 40°S and 20°N (Fig. 31). By June 2022, the plume had reached Antarctica and in August (Fig. 32) extended from 25°N to within the Antarctic polar vortex, where Polar Stratospheric Clouds (PSCs) were observed along with sulfate aerosols. In August 2022, the plume was near 22 km altitude at the equator, but descended steadily to about 18 km at 60°S. The plume persisted and was present in October 2022 from 30°N to Antarctica. By late November 2022 the Tonga plume reached the Arctic at about 21 km in altitude and was still strongly present in Antarctica. Tonga stratospheric aerosols have therefore spread around the globe. Daily plots of atmospheric extinction from the 1.02 μm imager are available on the ACE website, https://ace.uwaterloo.ca/."[54]

As can be seen in Figure 33, the composition of Tonga aerosols is dependent upon both temperature and water vapor pressure. Note that the figure includes data from the Tonga, Raikoke and Nabro volacanoes were included in order to test the generality of the dependence. In general, the % sulfuric acid in the aerosol decreases as temperature decreases and as water vapor pressure increases. The authors presume this relationship is due to water being taken up by the droplet. The temperature dependence is strong; Figure 34 plots sulfuric acid weight composition % as a function of temperature for the Tonga aerosol.

A multiple linear regression model was conducted using temperature T, water vapor pressure $\log_{10}(\mathrm{P}_{H2O})$ as independent variables and and the % sulfuric acid, w_{H2SO4} as the

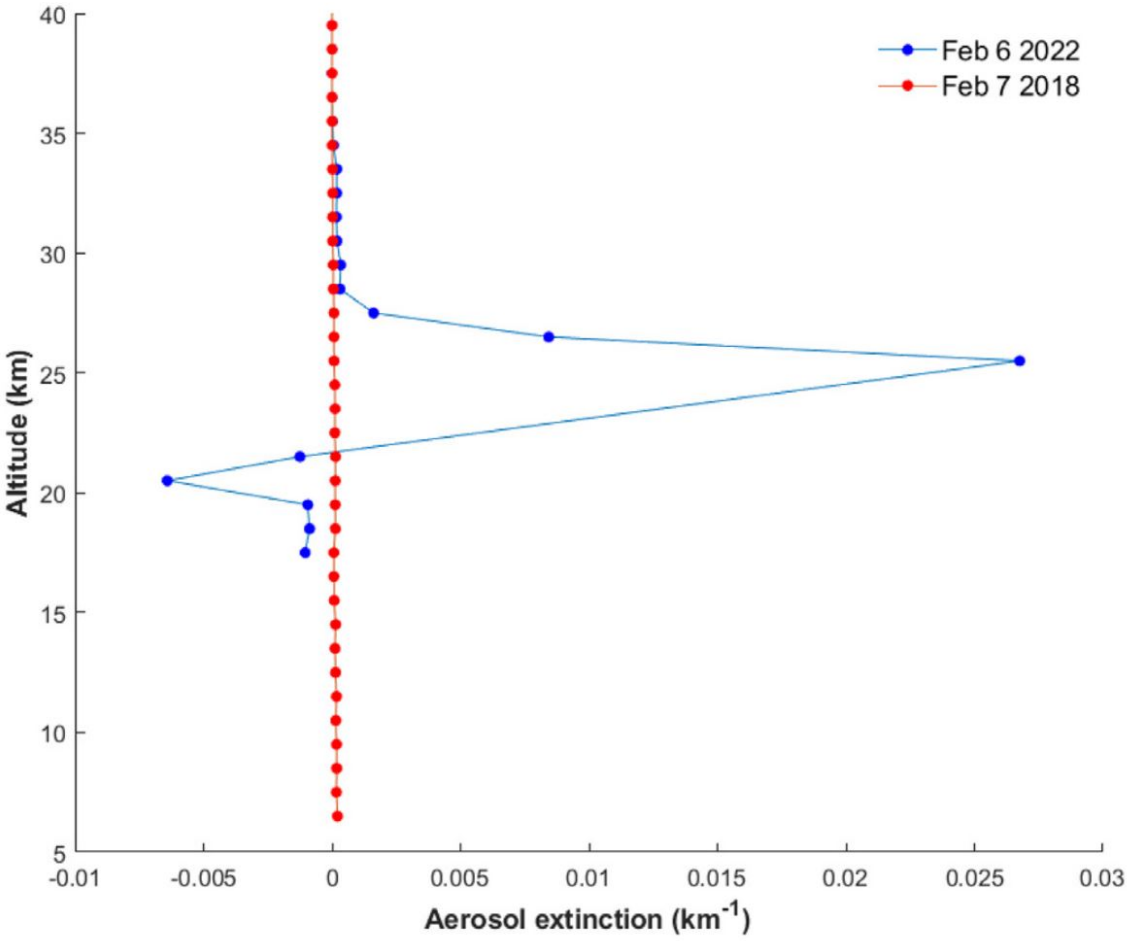

FIG. 29: Aerosol extinction from the ACE 1.02 μm imager from 6 Feb 2022 showing aerosol from the Tonga volcano [54].

Note: Occultation at 19.85°S 127.59°E. A reference occultation with no volcanic plume from 7 Feb 2018 is included for comparison.

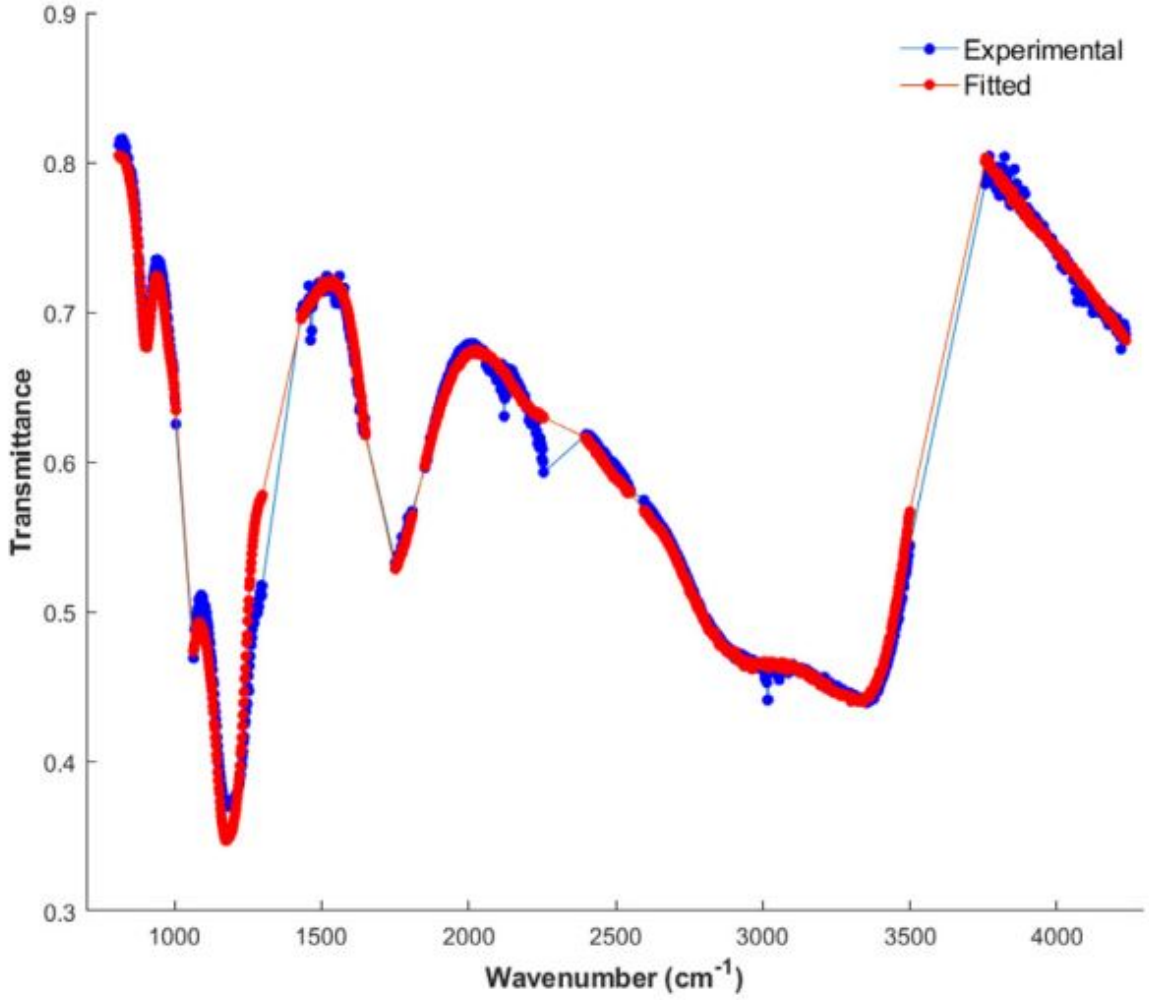

FIG. 30: Sulfate aerosol spectra from 6 Feb 2022 at 23.1 km [54].
Note: Occultation at 19.85°S 127.59°E. Observed spectrum in blue, fitted spectrum in red.

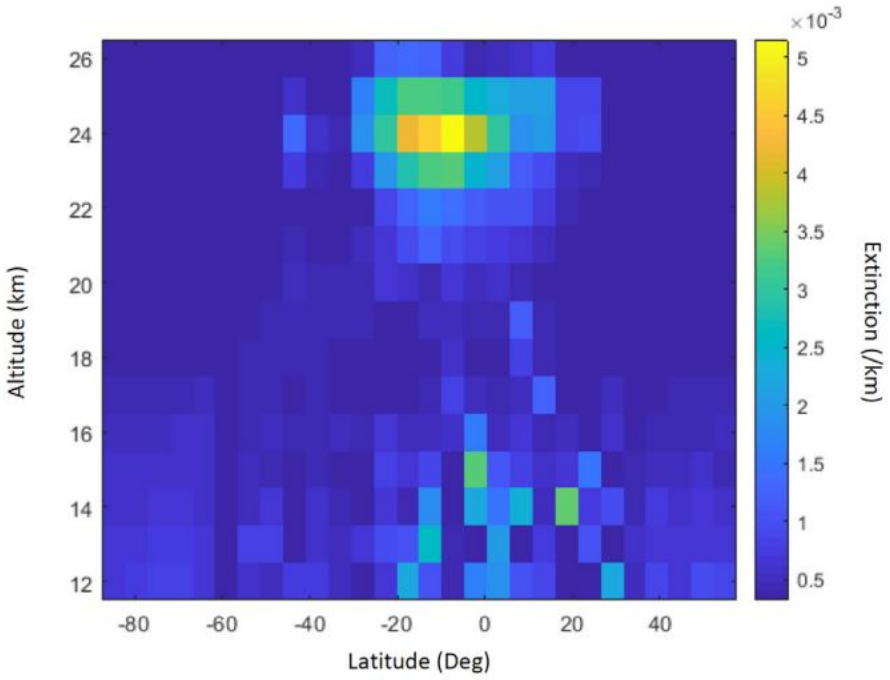

FIG. 31: Aerosol extinction for April 2022 [54].

Note: ACE Imager aerosol extinction at 1.02 μm for 5° latitude by 1 km altitude bins .

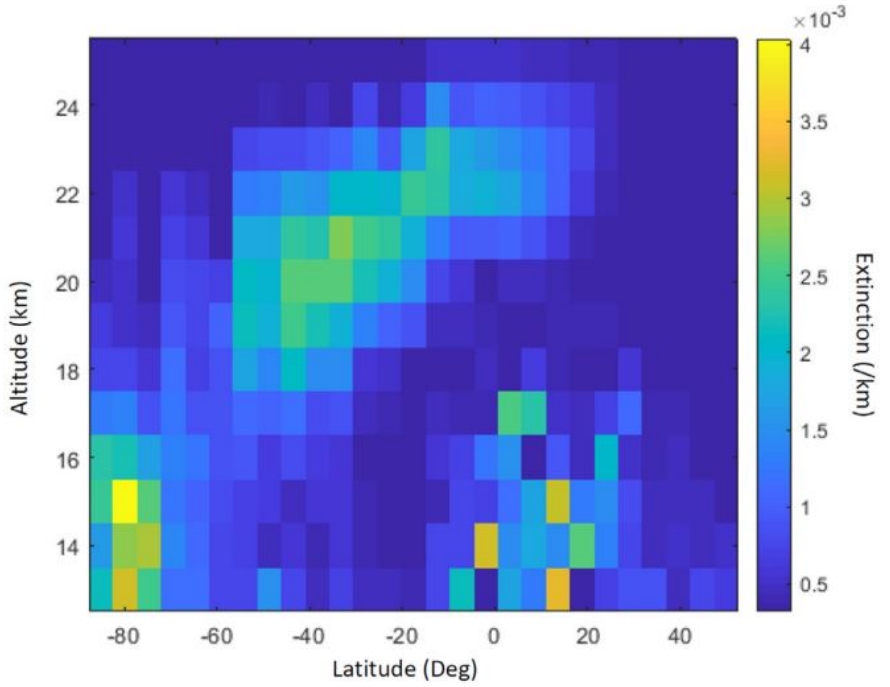

FIG. 32: Aerosol extinction for August 2022 [54].

Note: ACE Imager aerosol extinction at 1.02 μm for 5° latitude by 1 km altitude bins.

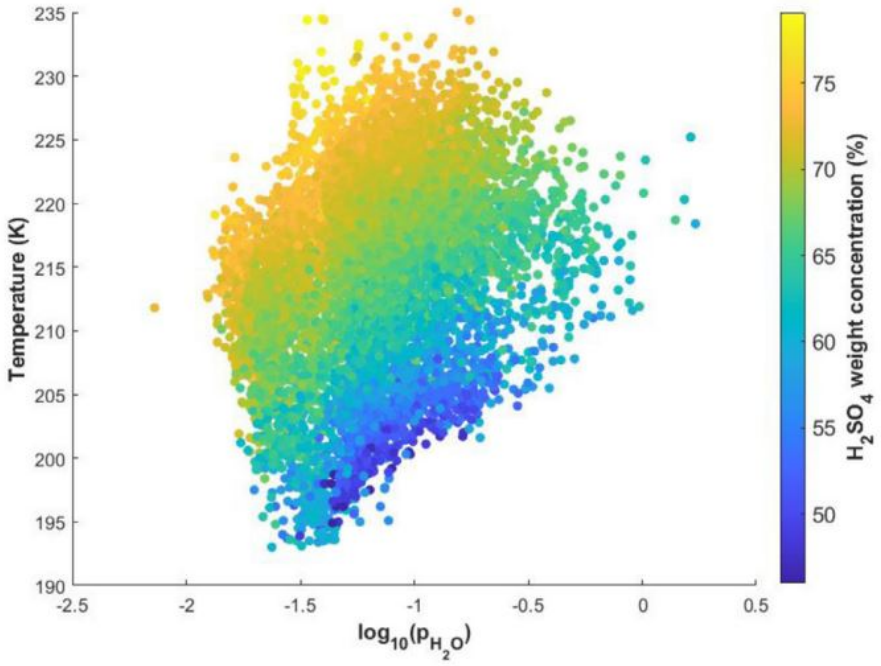

FIG. 33: Observed composition of sulfate aerosols [54].

Note: The H_2SO_4 concentration (weight %) using the color scale on the right as a function of temperature (K) and $\log_{10}(H_2O$ vapor pressure in Pa). As the temperature decreases and the water vapor pressure increases, the sulfuric acid concentration decreases. Points from Tonga, Raikoke and Nabro volcanic eruptions are included.

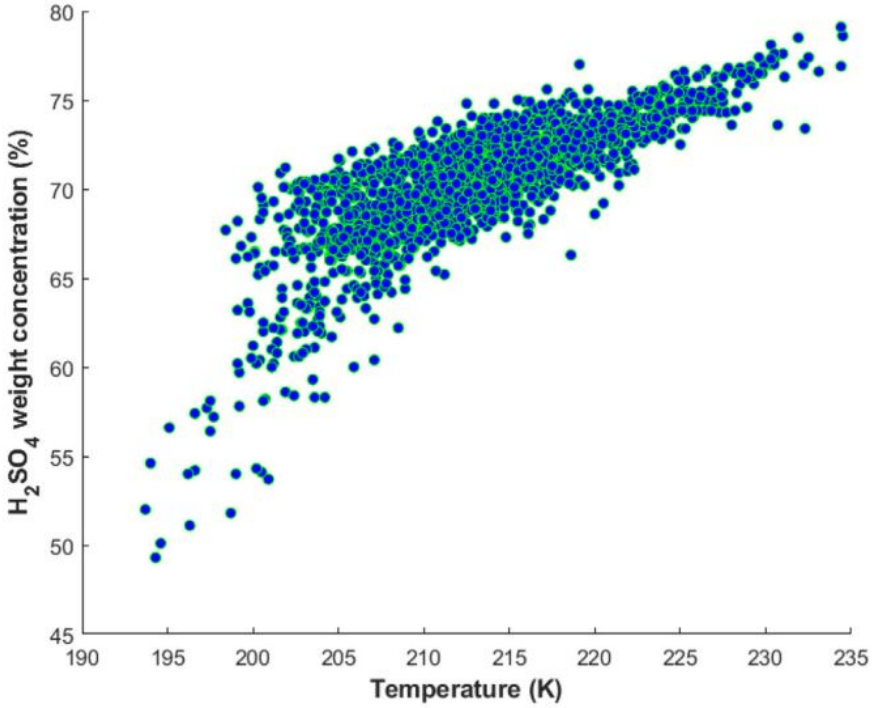

FIG. 34: Composition of Tonga aerosols [54].

Note: H_2SO4 concentration (weight %) as a function of temperature.

TABLE 3: Model fitting parameters 95% confidence intervals for expression [54].

:

$w_{H_2SO_4} = b_1 + b_2 \cdot \log(p_{H_2O}) + b_3 \cdot T + b_4 \cdot \log(p_{H_2O}) \cdot T + b_5 \cdot T^2 + b_6 \cdot \log(p_{H_2O}) \cdot T^2$

b_1	b_2	b_3	b_4	b_5	b_6
-3247.978526	-2006.279378	29.50611648	18.09111791	-0.065698667	-0.040907737
	Lower	**Upper**			
b_1	-3402.87290	-3.09308416			
b_2	-2126.71903	-1885.83972			
b_3	28.06348	30.94875			
b_4	16.96591	19.21632			
b_5	-0.06906	-0.06234			
b_6	-0.04353	-0.03828			

Note that the parameters are strongly correlated. Lower column is the b-lower margin, Upper column is the b-upper margin.

dependent variable. Data from the Tonga and Raikoke volcanoes was used. Data from the month immediately after the eruption of both volcanoes was excluded to allow the aerosols to stabilize. Note in Fig. 34 the dependence of composition on temperature does not appear linear, to account for this a T^2 term was added to model. The model includes a cross term between the independent variables as well as between $\log_{10}(\mathrm{P_{H_2O}})$ and T^2[54]:

$$\begin{aligned} w_{H_2SO_4} = &-3247.97853 - 2006.27938 \cdot \log(p_{H_2O}) + 29.50612 \cdot T \\ &+18.09112(p_{H_2O}) \cdot T - 0.06570 \cdot T^2 - 0.04091 \cdot \log(p_{H_2O}) \cdot T^2. \end{aligned} \tag{98}$$

The coefficient of determination (R^2) is 0.88 and errors for the fitting parameters are given as 95% confidence intervals. See Table 3.

"The strong dependence on temperature of aerosol composition is not unexpected because the vapor pressure of water is an exponential function of temperature (at equilibrium). Therefore as temperaure decreases, water vapor pressure decreases and more water will go into sulfate solution, diluting the H_2SO_4 concentration."[54]

The median radii, r_m of the sulfate aerosols are weakly dependent upon temperature and

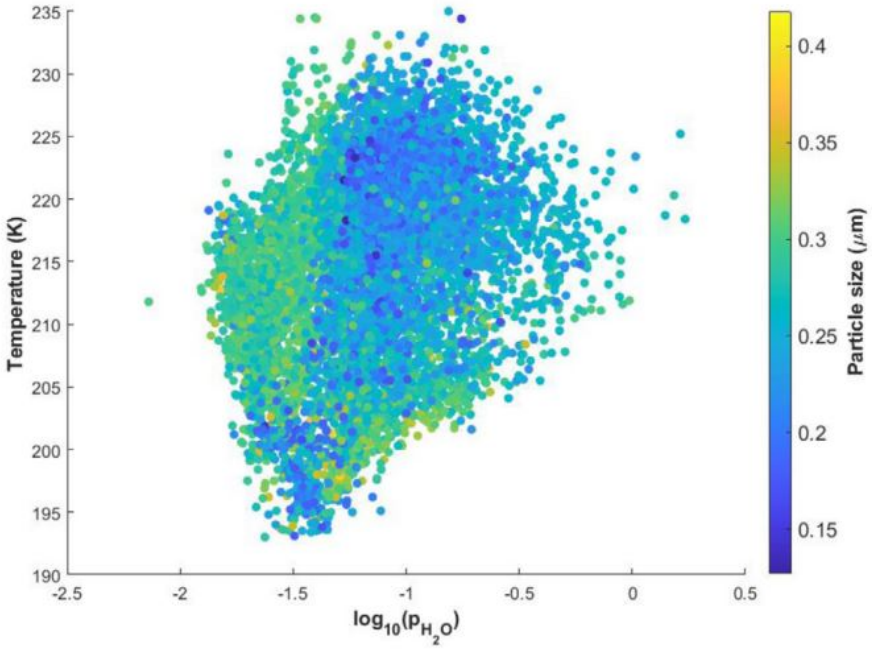

FIG. 35: Observed median particle radius [54].

Note: Particle size r_m in μm as a function of temperature and logarithm (base 10) of the water vapor pressure in Pa.

water vapor pressure. See Fig. 35.

The median particle radius was calculated for aerosols from the Tonga, Raikoke and Nabro volcanoes. The average values are: Tonga, 0.295 $\pm$ 0.022 μm; Raikoke, 0.257 $\pm$ 0.027 μm; Nabro, 0.214 $\pm$ 0.031 μm. Combining all three volcanoes into one data set results in r_m=0.261 $\pm$ 0.035 μm.

"There are thermodynamic predictions for the size and composition stratospheric sulfate aerosols [74, 75]. The size of the aerosols depends on the mass of sulfuric acid in the droplet but depends only weakly (as we find, Fig. 35) on temperature and water vapor pressure for typical stratospheric conditions [75]. The composition at a given temperature depends only on the water vapor pressure and the predicted thermodynamic values are in reasonable agreement with our observations [75]. For three examples from Raikoke, the composition predictions [75] for 225 K, 220 K and 215 K are 72.4%, 69.4%, 68.1% compared

to the observed 72.8%, 69.9% and 68.8%, respectively. Although our analysis and model are for volcanic plumes, the work is based on thermodynamic variables, so Eq. (99) likely applies to background stratospheric aerosols; further work on this topic with ACE data is underway."[54]

CHAPTER 7

VOLUME MIXING RATIOS OF NITROGEN DIOXIDE, NITRIC ACID AND THEIR ^{15}N ISOTOPOLOGUES

The findings and most of the material presented in this section have not yet been published. I researched the topic and presented my findings at the ACE Satellite Science Meeting held on 18 Oct 2022 at the University of Waterloo. I presented remotely from Old Dominion University. Peter Bernath (Old Dominion University) is the advisor on this project, to include making edits to my presentation. The research presented in this section is based on the power point presentation and supporting notes I used to present at the ACE meeting. I composed all the presentation materials and did the analysis. This work is original and has not yet been published anywhere. Based on discussions with Dr. Bernath, this material is likely to be made into a paper after my dissertation defense.

7.1 INTRODUCTION

Much of our understanding of the stratospheric ozone layer stems from 1930 when Sydney Chapman proposed that the ozone layer, known to exist since the 1920s, was formed from photolysis of O_2:

$$\begin{aligned} O_2 + h\nu &\rightarrow 2O \\ (\lambda < 240 \text{ nm}) & \\ O + O_2 &\overset{M}{\rightarrow} O_3. \end{aligned} \tag{99}$$

The ozone then undergoes photolysis:

$$\begin{aligned} O_3 + h\nu &\rightarrow O_2 + O(^1D) \\ (\lambda < 320 \text{ nm}) & \\ O(^1D) &\overset{M}{\rightarrow} O \\ O_3 + O &\rightarrow 2O_2. \end{aligned} \tag{100}$$

The combined reactions shown in equations (100) and (101) are known as the Chapman mechanism. The Chapman mechanism accounts for the production of ozone and its photolysis, but taken in isolation it overestimates the amount of ozone that should be in the stratosphere by about a factor of two. There are other sinks that account for the observed levels of ozone in the stratosphere, primarily the catalytic loss cycles known as the HO_x, NO_x and ClO_x cycles. NO_x collectively refers to NO_2 and NO. The significance of atmospheric nitrogen dioxide and nitric acid will become apparent in the discussion that follows regarding the NO_x cycle.

The NO_x cycle, resulting in the destruction of ozone, is:

$$\begin{aligned} NO + O_3 &\rightarrow NO_2 + O_2 \\ NO_2 + O &\rightarrow NO + O_2. \end{aligned} \tag{101}$$

Note the net reaction is

$$O_3 + O \rightarrow 2O_2. \tag{102}$$

There is an additional null cycle known as the Leighton cycle:

$$\begin{aligned} NO + O_3 &\rightarrow NO_2 + O_2 \\ NO_2 + h\nu &\rightarrow NO + O \\ O + O_2 &\overset{M}{\rightarrow} O_3. \end{aligned} \tag{103}$$

The net reaction of the Leighton cycle is

$$NO + NO_2 \rightarrow NO_2 + NO; \tag{104}$$

a rapid cycling between NO and NO_2 occurs, the entire cycle only takes about a minute in the Earth's atmosphere.

Nitric acid, HNO_3, plays a key role in the daylight termination of the NO_x cycle:

$$NO_2 + OH \overset{M}{\rightarrow} HNO_3. \tag{105}$$

NO, NO_2, HNO_3 and several other molecules that are not part of the chemistry shown here are collecively referred to as NO_y. At night there is minimal OH in the atmosphere, so the NO_x cycle is terminated by the reaction series:

$$\begin{aligned} NO_2 + O_3 &\rightarrow NO_3 + O_2 \\ NO_3 + NO_2 &\overset{M}{\rightarrow} N_2O_5. \end{aligned} \tag{106}$$

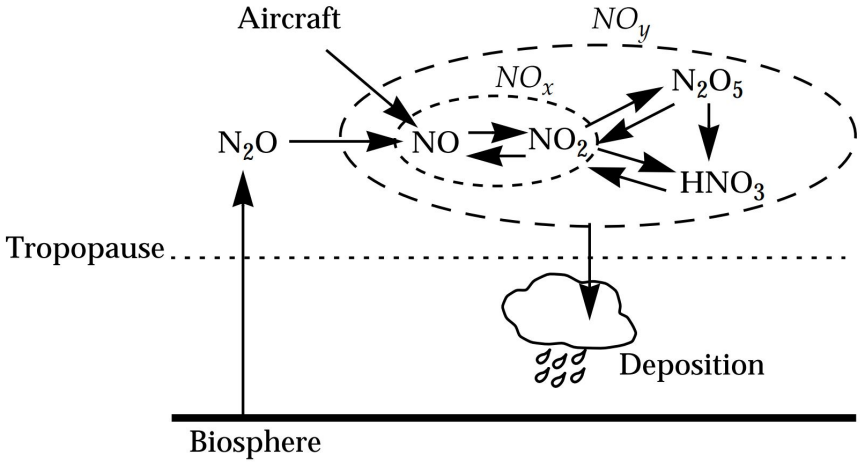

FIG. 36: NO_x cycle, sources and sinks [76].

Note this reaction series can only take place at night, since under daylight conditions NO_3 is photolyzed back into NO_2 on a time scale of a few seconds. HNO_3 and N_2O_5 can be thought of as reservoirs for NO_x.

The diagram from Jacob [76] sums it up nicely (See Fig. 36); NO_x flips back and forth between NO and NO_2. NO_x collectively moves back and forth in a bigger cycle with NO_y. N_2O coming up from the biosphere is the primary source of it all. At the end, HNO_3 slowly sinks out of the stratosphere. Note the arrows in the diagram go both ways with HNO_3 and N_2O_5; during daylight through photolysis and reactions with OH both molecules revert back to NO_2. A recurring theme in discussion of the NO_x cycle is sunlight. With sunlight NO_2 is enhanced. The expectation is then that the reservoir HNO_3 is enhanced at night.

7.2 ANALYSIS AND RESULTS

The ACE-FTS database includes NO_2, HNO_3 and the ^{15}N isotopologue of both molecules. Fig. 37 shows the volume mixing ratio of NO_2 and HNO_3 averaged over the entire ACE database, broken down by latitude and altitude.

As expected, Figure 37 confirms NO_2 to have higher VMRs in the equatorial region where sunlight is always present for much of the day, and HNO_3 has higher VMRs over the poles, immersed in darkness for long periods. Similar plots made with the ^{15}N isotopologues of

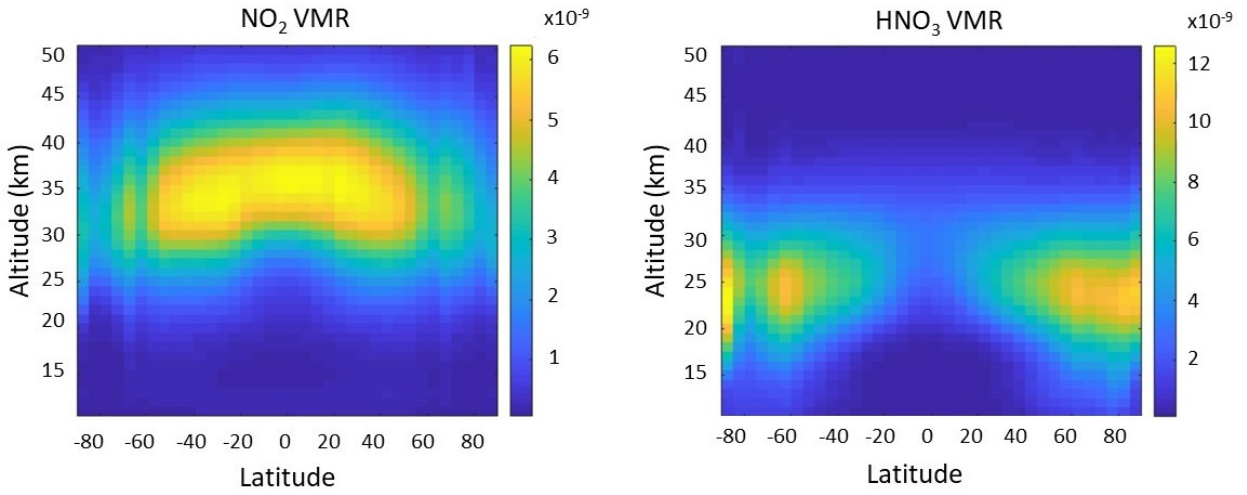

FIG. 37: NO_2 (left) and HNO_3 (right) VMRs averaged over the entire ACE database. Note: In each plot latitude is along the x axis, altitude (km) is along the y-axis, left side. Color code for VMR is displayed to right side of the plot.

both molecules show the same patterns. Since the poles also have long periods of sunlight, a more revealing plot would be seasonal. Figures 38 and 39 show seasonal plots of NO_2 and HNO_3, respectively. The plots confirm NO_2's affinity for sunlight, with accumulations occuring over the summer pole along with the equator. HNO_3 seasonal plots reveal the polar patterns show enhanced HNO_3 over the darkened winter pole. Note the equinoxes are in September and March, so as expected, the polar NO_2 pattern begins in the spring, and the polar HNO_3 pattern begins in the autumn.

The goal of this research is to search for patterns in the fractionation of the isotopologues. Specifically, we wanted to investigate whether or not there were predictable patterns in which the fractionation of the two molecules differed from their standard atmospheric values. The U.S. Geological Survey publishes standard atmospheric ratios between isotopes. For nitrogen, the published value is $\frac{[^{14}\mathrm{N}]}{[^{15}\mathrm{N}]} = 272$. A handy measurement of fractionation is to calculate what is known as the δ value:

$$\delta^{15}\mathrm{N} = \left[\frac{\left[\frac{^{15}\mathrm{N}}{^{14}\mathrm{N}}\right]_{\mathrm{x}}}{\left[\frac{^{15}\mathrm{N}}{^{14}\mathrm{N}}\right]_{\mathrm{air}N_2}} - 1 \right] \cdot 1000, \tag{107}$$

where the value is in permille ($\frac{o}{oo}$). If $\delta^{15}\mathrm{N} = 0$, the standard atmospheric ratio is present,

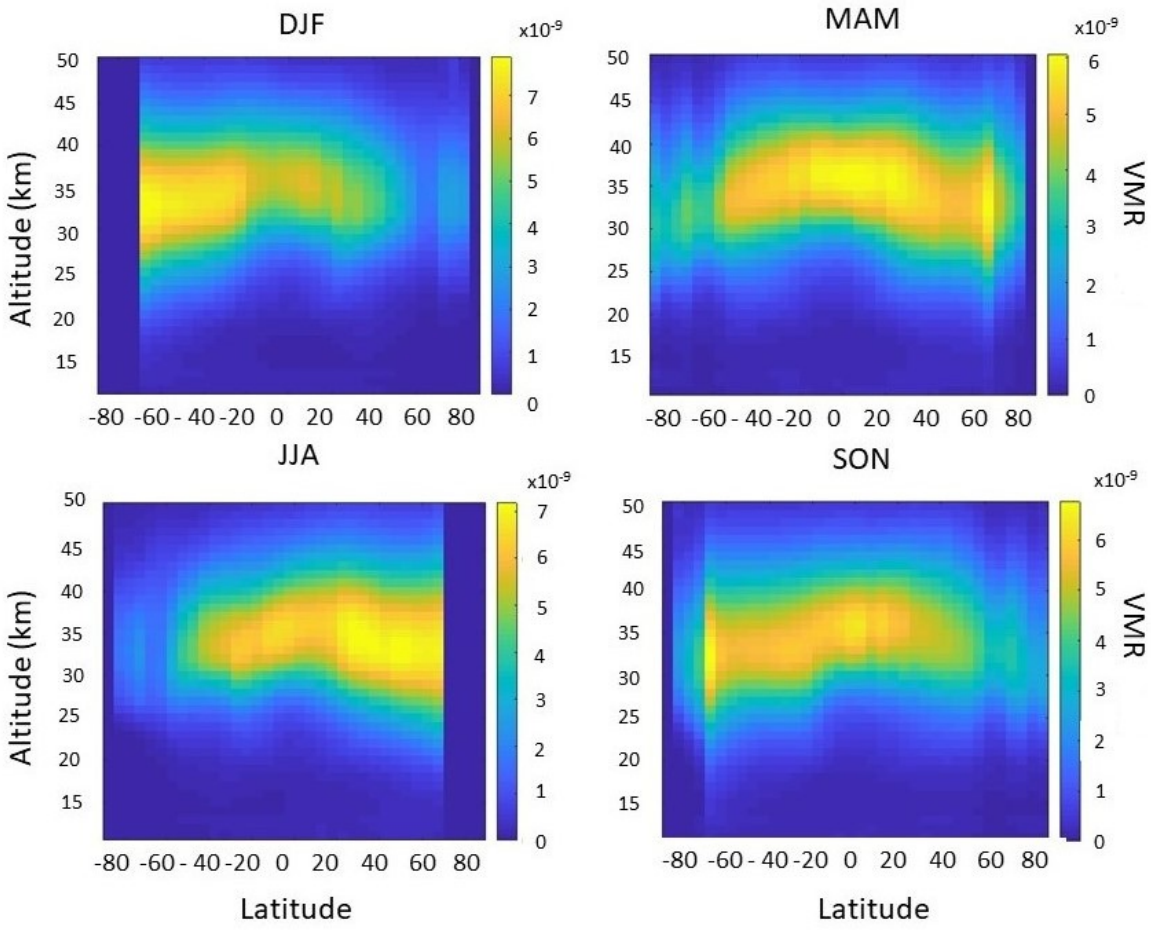

FIG. 38: NO_2 seasonal VMRs averaged over the entire ACE database.
Note: In each plot latitude is along the x axis, altitude (km) is along the y-axis, left side. Color code for VMR is displayed to right side of the plot.

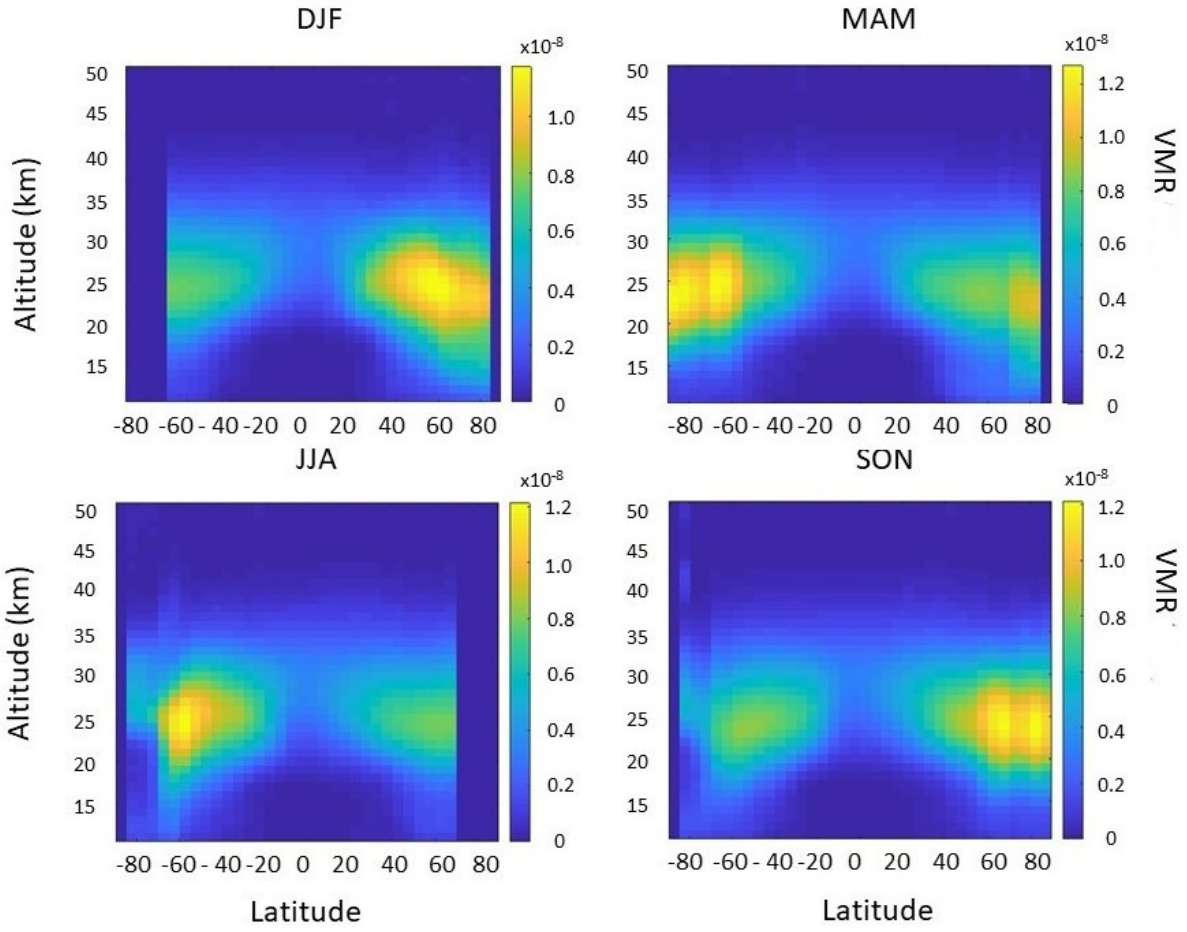

FIG. 39: HNO_3 seasonal VMRs averaged over the entire ACE database.
Note: In each plot latitude is along the x axis, altitude (km) is along the y-axis, left side. Color code for VMR is displayed to right side of the plot.

a positive number indicates above standard presence of the ^{15}N isotope, a negative number indicates a below standard presence of the ^{15}N isotope. There are three basic ways the fractionation δ value can be altered: the equilibrium isotope effect, the kinetic isotope effect and the photochemical isotope effect.

Li et al. (2020) [77] did a study on fractionation effects between NO and NO_2. The equilibrium isotopic effect (EIE), addresses an exchange between two compounds without forming new molecules, in this case the exchange would be

$$^{15}NO + ^{14}NO_2 \rightarrow ^{14}NO + ^{15}NO_2, \tag{108}$$

EIE has a positive δ^{15}N value for NO_2. The EIE is influenced by differences in vibratioanal frequencies between the isotopologues. Li et al. experimentally found δ^{15}N for EIE to be $+28.9\frac{o}{oo}$, consistent with past experiments and calculations. The kinetic isotope effect (KIE) is associated with the difference in isotopologue rate coefficients during unidirectional reactions, in this case KIE would mean oxidation of NO into NO_2 by $O_3/HO_2/RO_2$. The photochemical istope fractionation effect (PHIFE) is related to photolysis, in this case photolysis of NO_2 into NO. Li et al. found the combined effects of KIE and PHIFE, which they refer to as Leighton Cycle isotope effects (LCIE) to have a δ^{15}N value of -10$\frac{o}{oo}$. They summed up their findings in a diagram, see Figure 40.

Applying these findings to the stratospheric NO_x cycle, the expectations are that wherever NO and NO_2 are cycling back and forth, perhaps wherever the null cycle is occurring, δ^{15}N is positive for NO_2. Note this enhancement of the NO_2 δ^{15}N value is no more than about $19\frac{o}{oo}$ based on Li et al. More influentially, wherever NO_2 or HNO_3 have accumulated and then that accumulation has recently decreased due to seasonal cycles, caused by photolysis and/or kinetic isotope effect type reactions, the ^{14}N molecules will leave more quickly due to the ^{15}N molecules having slower kinetic interaction and a higher photolysis threshold, enhancing δ^{15}N where the accumulation had been.

Figure 41 shows the NO_2 δ^{15}N enhancement for the months December through February averaged over the entire ACE database. The left image in Figure 41 is the same as the upper left DJF image in Fig. 38 and is included for reference. In DJF sunlight has left the North Pole and NO_2 is being replaced by HNO_3; the upper right image shows a δ^{15}N enhancement from the tropopause up to about 20 km; in the lower right images all δ^{15}N values above 1000 have been removed to show the enhancement actually extends higher and includes a second smaller group of peak values at the top of the microwindow which extends up to 38 km. As shown if Figure 18, the Brewer-Dobson circulation includes a descending polar vortex over

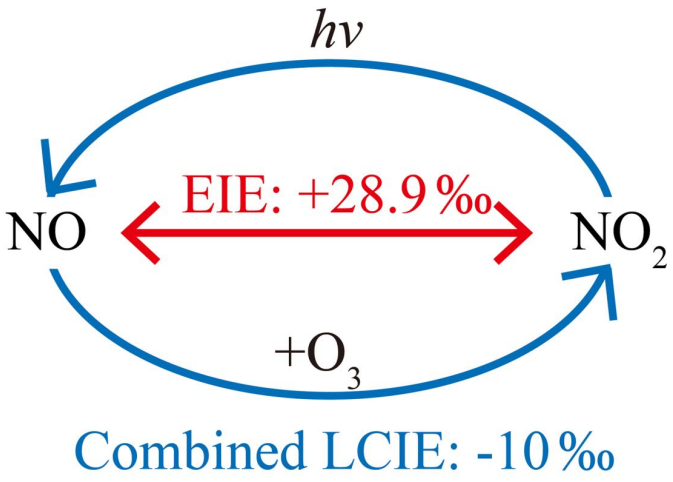

FIG. 40: Isotopic fractionation process between NO and NO_2 [77].

the winter pole, it is possible this upper smaller peak is due to the polar vortex; an issue for future analysis.

Figure 42 shows the HNO_3 $\delta^{15}N$ enhancement for the months March through May averaged over the entire ACE database. The left image in Figure 42 is the same as the upper right MAM image in Figure 39 and is included for reference. The HNO_3 $\delta^{15}N$ plots differ from NO_2 due to HNO_3 being constantly photolyzed over the equator, so there is a strong permanent enhancement there. In the March-May time frame sunlight has arrived in the North Pole region and there is a corresponding enhancement in HNO_3 $\delta^{15}N$ up high at 28-32 km near the pole. As in Figure 41, having peak values at the top of the microwindow again raises questions over the role of upper level Brewer-Dobson circulation; an issue for future analysis.

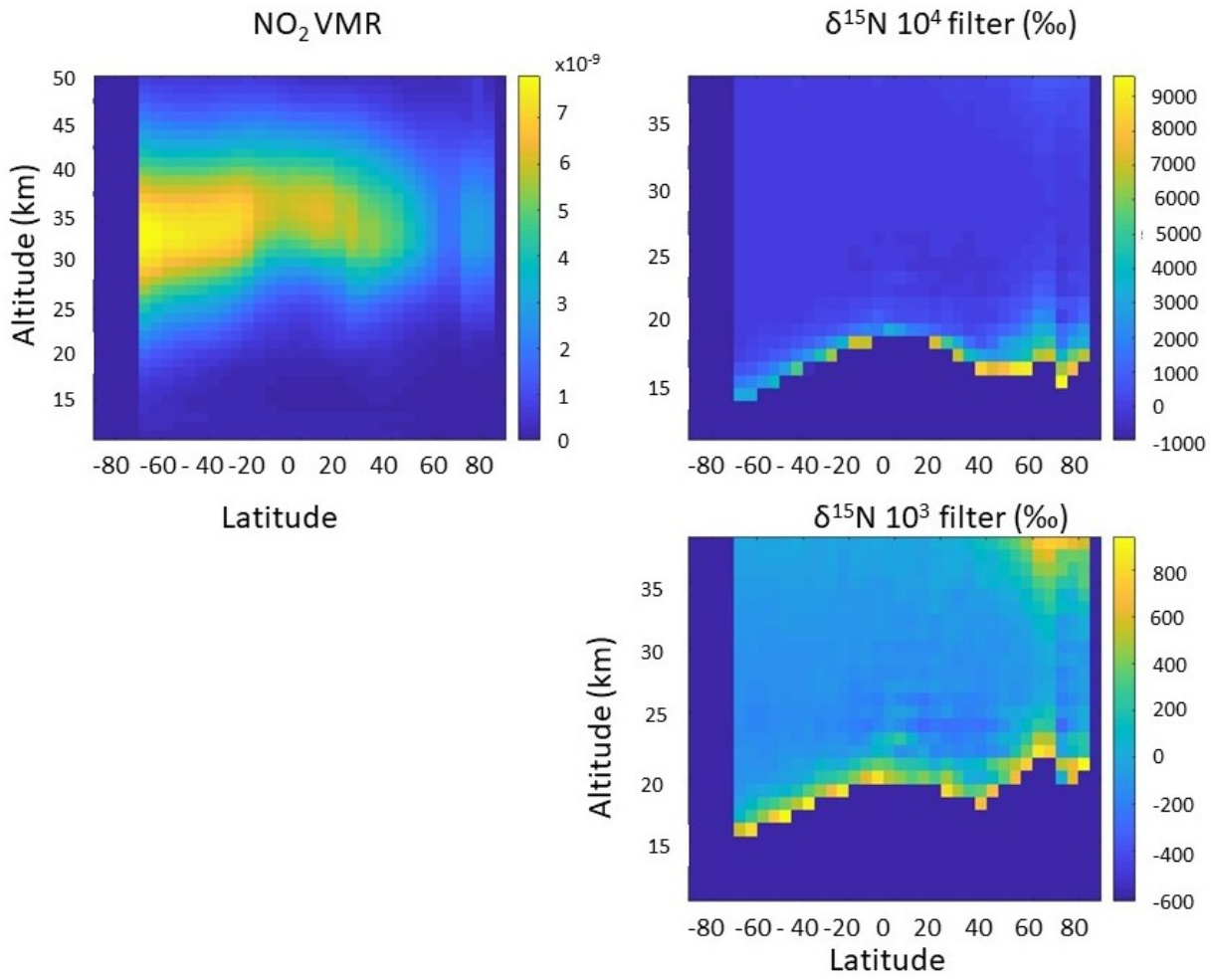

FIG. 41: Left side is NO_2 VMR for Dec/Jan/Feb averaged over entire ACE database; right top image shows δ^{15}N enhancement at 17-20 km on the north end.
Note: Filtering out high $\delta^{15}N$ values at right bottom shows a lesser peak at 30-38 km on the north end.

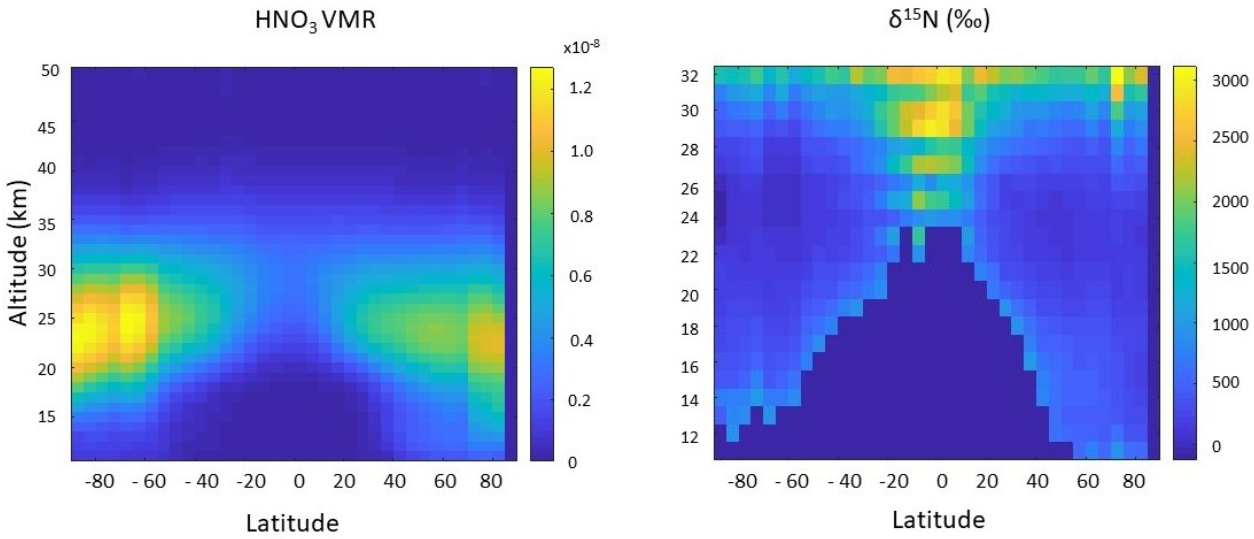

FIG. 42: Left side is HNO_3 VMR for Mar/Apr/May averaged over entire ACE database; right image shows δ^{15}N enhancement over the equator and a lesser peak at 28-32 km on the north end.

CHAPTER 8

NEAR-INFRARED OPACITY OF LATE M DWARFS AND HOT JUPITERS: THE $E^3\Pi$-$X^3\Delta$ TRANSITION OF TITANIUM MONOXIDE

The findings and most of the material presented in this section are published in The Astrophysical Journal (Bernath & Cameron [80]). Peter Bernath (Old Dominion University) is the corresponding author and project advisor, he wrote the text of the paper and advised me during the analysis. I am the co-author, I did the rotational analysis to include developing the line list and spectroscopic constants, which also generated the figures and tables in the paper. This work is original and was not published anywhere prior to its publication in The Astrophysical Journal.

8.1 INTRODUCTION

"Titanium oxide (TiO) plays a key role in astronomical observations of varied sources to include stars, circumstellar envelopes and gas giant planets, to include exoplanets. For M class dwarf stars, the most numerous star type in our galaxy, the spectra are marked with strong absorption features due to TiO [82]. The pure rotational microwave transitions of TiO have been detected in red supergiants, supporting the concept that titanium oxides are formed in circumstellar envelopes and seed inorganic dust formation [83]. TiO has been detected in the atmospheres of exoplanets by its electronic spectra and shown to cause formation of stratospheres in hot Jupiters [4, 84].[81]"

The success of astronomical observations is significantly dependent upon the results of laboratory spectroscopy. McKemmish et al. (2017) [85] provides a summary of laboratory spectroscopy for the TiO molecule. McKemmish et al. (2019) [12] is currently the most comprehensive line list for TiO with over 60 million transitions, to include the minor isotopologues. That line list is largely based on calculations, and can be improved upon by laboratory spectroscopy. See Fig. 7 for a diagram of the energy levels of the TiO molecule.

"The $E^3\Pi$ - $X^3\Delta$ transition (ϵ system) is a relatively weak band system in the near-infrared near 8450 Å (11,830 cm^{-1}) for the 0–0 band. In spite of an oscillator strength (f_{0-0})

of only 0.0019 [86], the 0–0 band is the strongest absorption feature in the near-infrared spectra of late M dwarfs, e.g., Figure 12 in the spectral library of Rayner et al. [87].

The $E^3\Pi$ - $X^3\Delta$ transition was first measured by McIntyre et al. [88] in a neon matrix, followed by low resolution chemiluminescence spectra in the gas phase [89]. Simard & Hackett [90] carried out the first rotational analysis of the 0-0 band at medium resolution by pulsed-laser excitation spectroscopy with a laser vaporization TiO source. Steimle & Virgo [91] used the Stark effect to measure the permanent electric dipole moments in several electronic states including $E^3\Pi$. The definitive rotational analysis was by Kobayashi et al. [92], who used a high resolution c.w. laser and a cold free jet expansion source. While the jet-cooled TiO source gave clean spectra, relatively few rotational levels were measured in the 0-0 band and almost none in the weak 1-0 band.

During the preparation of the high temperature absorption cross sections, it was noted [93] that the E−X 0-0 band was present, although overlapped by the $A^3\Phi$- $X^3\Delta$ 0-2 band [94]. The low J transitions observed in the laboratory matched the ExoMol lines [12] which are the measured lines of Kobayashi et al. [92], but the higher J values deviated from the ExoMol DUO [95] prediction. We present here an improved rotational analysis of the 0-0 band of the $E^3\Pi$ - $X^3\Delta$ transition." [80]

8.2 METHOD AND RESULTS

"The experimental TiO cross sections used in the analysis were based on an emission spectrum recorded at the McMath–Pierce Solar Telescope using the 1 m Fourier transform spectrometer, operated by the National Solar Observatory at Kitt Peak, Arizona. The source was a carbon tube furnace at about 2300 K, and the conversion of the spectrum to calibrated cross sections has been described (Bernath) [93]. These cross sections have a resolution of about 0.06 cm^{-1} and an accuracy of ± 0.002 cm^{-1} for the wavenumber calibration. An overview of the cross sections (upwards) and the simulation of the 0–0 $E^3\Pi$- $X^3\Delta$ and 0–2, 1–3 $A^3\Phi$- $X^3\Delta$ bands (downwards) is presented in Figure 43.

The 2300 K temperature of the TiO source is a good match for the photospheric temperatures of late M dwarfs. For example, Luhman et al. [96] have determined the temperature of M8 dwarfs to be 2500 K and M9 dwarfs to be 2300 K. Hot Jupiter exoplanets also have atmospheric temperatures in this range. TiO has been detected by high-resolution spectroscopy in very hot Jupiter exoplanet WASP-33 b [4]. WASP-33 b has a brightness temperature of about 3600 K and atmospheric temperatures in the range 2700-3700 K.

The $E^3\Pi$, $A^3\Phi$ and $X^3\Delta$ states all belong to Hund's case (a) so the E - X and A - X

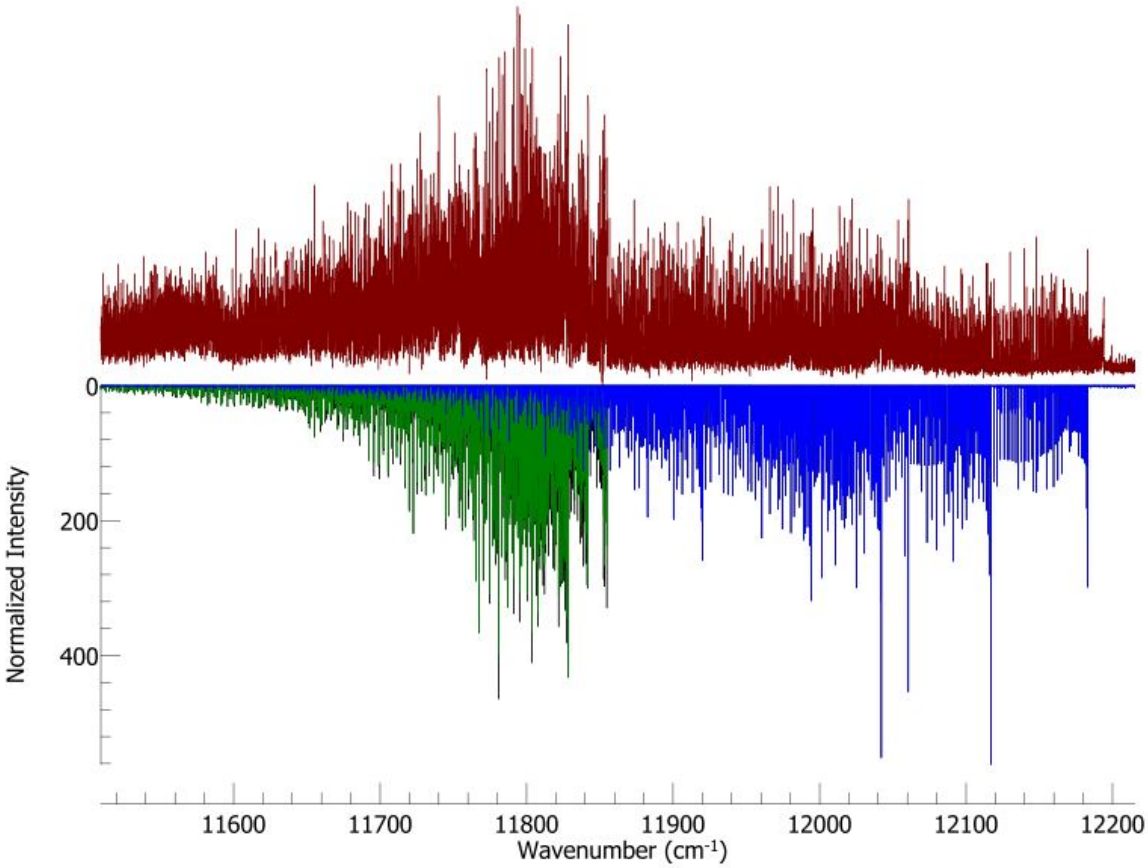

FIG. 43: Overview spectrum of TiO (upwards) and the simulation of the 0-0 $E^3\Pi$-$X^3\Delta$ (green) and 0-2, 1-3 $A^3\Phi$-$X^3\Delta$ bands (blue) (downwards) [80].

transitions have three spin components, $E^3\Pi_2$- $X^3\Delta_3$, $E^3\Pi_1$- $X^3\Delta_2$, $E^3\Pi_{0^+0^-}$- $X^3\Delta_1$ and $A^3\Phi_2$-$X^3\Delta_1$, $A^3\Phi_3$-$X^3\Delta_2$, $A^3\Phi_4$-$X^3\Delta_3$, in order of increasing wavenumbers. In Figure 43, the three R-branch subband heads are to the right for the 0-2 A - X band (12042.40, 12116.95, 12183.15 cm^{-1}; R_1, R_2, R_3 heads, respectively) and to the left for the 0-0 E - X band (11828.49; 11841.68, 11842.19; 11853.58, 11854.76 cm^{-1}; $R_{3e,f}$; R_{2e}, R_{2f}, R_{1e}, R_{1f}, respectively). To the far right at 12193.96 cm^{-1} is another R-head not included in the simulation that is due to the 1-0 $b^1\Pi$-$a^1\Delta$ band.

The rotational analysis of the E - X 0-0 band was carried out with PGOPHER [19], starting with a spectral simulation using the E state constants of Kobayashi et al. [92] and the constants from the A - X analysis of Ram et al. [94]. The cross section file was used as an "overlay" in PGOPHER and the previously measured lines [92] were also included in the fit. New lines were measured and additional spectroscopic constants were added as the assignments were extended to higher J values. Although the spectral features were often blended (Figure 44), assignments were made up to J of about 60. Figure 44 shows the E - X lines in green (downwards) and the A - X lines in blue (downwards) compared to the observed cross sections (upwards) for a typical region with J values around 40. No attempt was made to assign all of the features in the observed spectrum.

Based on the E - X lines and spectroscopic constants for the 1-0 band, a careful search was made in the observed spectrum but without success. The 1-1 band also was too weak and not present in the experimental cross section data.

The new spectroscopic constants for $v = 0$ of the $E^3\Pi$ state are provided in Table 4. In the end, 1058 lines were fitted with the standard N^2 Hamiltonian [94] with an average error of 0.014 cm^{-1}. The lines and the observed minus calculated values are given in Table 5."[80]

8.3 DISCUSSION AND CONCLUSION

"The spectroscopic constants (Table 4) and 0-0 E - X lines (Table 5) extend the previous analysis from the maximum J of about 30 in a few branches to higher J values of about 60. Five higher order spectroscopic constants (H, o_D, p_D, A_H, λ_D) were determined and the spectrum of this band of hot TiO is now reliably reproduced by the constants as needed for stellar and exoplanet spectroscopy. The traditional spectroscopic labels for the lines are provided in Table 5: $\Delta N \Delta J_{F_i' F_j''} p(J)$, in which N is the quantum number for the total angular momentum excluding electron spin, p is e/f the rotationless parity, F_i labels the spin components (for $^3\Pi$, $F_3 = {}^3\Pi_2$, $F_2 = {}^3\Pi_1$, $F_1 = {}^3\Pi_0$ and for $^3\Delta$, $F_3 = {}^3\Delta_3$, $F_2 = {}^3\Delta_2$, $F_1 = {}^3\Delta_1$) [93].

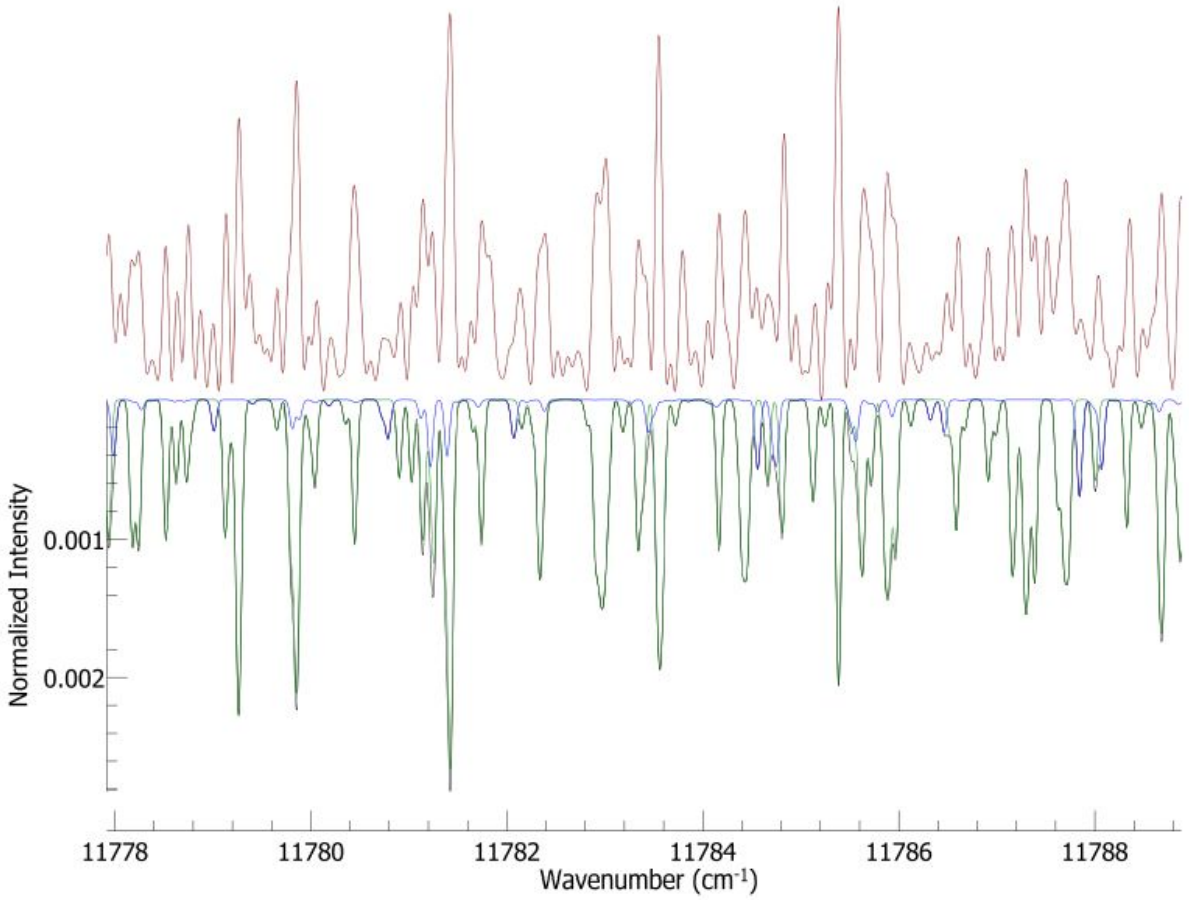

FIG. 44: Typical TiO E - X spectrum (upwards) with the simulation in green pointing downwards [80].

Note: The A - X simulation in blue points downwards also.

TABLE 4: Spectroscopic Constants for the $v = 0$ Level of the $E^3\Pi$ State in cm^{-1} with one Standard Deviation Error in the Last Two Digits in Parentheses [80].

Constant	New Values	Kobayashi et al. Values
Origin	11826.95319(61)	11826.95482(94)
B	0.5150704(25)	0.5150622(72)
A	86.81598(65)	86.81686(98)
λ	1.41349(48)	1.41405(56)
o	0.82668(74)	0.82775(43)
p	0.02374(19)	0.02292(31)
q	2.38(39)e-5	4.4(10)e-5
D	6.427(20)e-7	6.58(11)e-7
H	-2.17(39)e-12	$\cdots$
λ_D	2.01(59)e-6	$\cdots$
o_D	1.08(18)e-5	$\cdots$
p_D	-1.82(48)e-7	$\cdots$
A_D	-1.641(16)e-4	-1.745(36)e-4
A_H	-2.46(53)e-9	$\cdots$

TABLE 5: Sample of Lines and Residuals for the 0-0 band of the E - X Transition from PGOPHER Log File [80].

J'	P'	J''	P''	Obs (cm^{-1})	Calc (cm^{-1})	O-C (cm^{-1})	Weight	Line
12	e	13	e	11796.476	11796.478	-0.0023	0.5	pP3e(13)
12	f	13	f	11796.476	11796.479	-0.0029	0.5	pP3f(13)
11	e	12	e	11797.997	11797.998	-0.0013	0.5	pP3e(12)
11	f	12	f	11797.997	11797.999	-0.0018	0.5	pP3f(12)
19	e	20	e	11798.740	11798.739	0.0015	0.5	pP2e(20)
26	f	27	f	11798.866	11798.870	-0.0035	0.5	pP1f(27)
19	f	20	f	11798.996	11799.002	-0.0062	0.5	pP2f(20)
10	e	11	e	11799.483	11799.482	0.0014	0.5	pP3e(11)

Note: Lines from Kobayashi et al. [92] have a weight of 0.5. New lines have a weight of 1. J is total angular momentum; P is the e/f parity; Obs is the observed line position in cm^{-1}; Calc is the calculated line position in cm^{-1}; O - C is the observed minus calculated line position in cm^{-1}; weight is the weight of the line in the fit. Source indicates the source of the line in the numbered line list; the first 399 lines are from Kobayashi et al. [92] and the rest are measured from the cross sections [93].
(This table is available in its entirety in machine-readable form.)

TABLE 6: Sample Table for Line List for the 0–0 and 0–1 Bands of the E - X Transition of TiO [80].

J'	J''	Pos (cm^{-1})	Eup (cm^{-1})	Elow (cm^{-1})	A (s^{-1})	f	Line
79	80	10510.390	15054.848	4544.458	8.585	1.151×10^{-7}	oP23e(80)
79	80	10512.660	15057.118	4544.458	12.901	1.728×10^{-7}	oP23f(80)
78	79	10514.641	14974.776	4460.135	8.570	1.147×10^{-7}	oP23e(79)
78	79	10516.885	14977.020	4460.135	12.799	1.713×10^{-7}	oP23f(79)
77	78	10518.854	14895.685	4376.831	8.552	1.144×10^{-7}	oP23e(78)
77	78	10521.071	14897.902	4376.831	12.695	1.697×10^{-7}	oP23f(78)
76	77	10523.027	14817.576	4294.548	8.532	1.140×10^{-7}	oP23e(77)
76	77	10525.217	14819.765	4294.548	12.586	1.681×10^{-7}	oP23f(77)
79	80	10525.486	14939.229	4413.743	12.993	1.736×10^{-7}	oP12f(80)

Note: J is total angular momentum; Pos is the line position in vacuum cm^{-1}; Eup and Elow are upper and lower energy levels in cm^{-1}; A is Einstein A value in s^{-1}; f is the oscillator strength; line assignments are the quantum numbers for the transition [93].
(This table is available in its entirety in machine-readable form.)

The radiative lifetime of $v = 0$ of the E state has been measured to be 4.9 ± 0.2 μs [86] leading to an oscillator strength $f_{0-0} = 0.00195 \pm 0.00008$ using Franck-Condon factors of $q_{0-0} = 0.86$, $q_{0-1} = 0.13$ and $q_{0-2} = 0.009$. These Franck-Condon factors were obtained using LeRoy's RKR [20] and LEVEL [21] programs with X state equilibrium constants from Ram et al. [94] and E state constants of $\omega_e = 921.3$ cm^{-1}, $\omega_e x_e = 4.2$ cm^{-1}, $B_e = 0.516680$ cm^{-1} and $\alpha_e = 0.003235$ cm^{-1}. This oscillator strength converts to a transition moment $M_{0-0} = 0.592$ D using $M = \sqrt{1458.377 f/\tilde{v}}$ with $\tilde{v}$ in cm^{-1} [93]. Using this band strength in PGOPHER provides a more complete calculated line list up to $J = 80$ including experimental line strengths (Table 6).

A similar calculation for the 0-1 band gives $f_{0-1} = 0.000270$ and a transition dipole moment $M_{0-1} = 0.230$ D. Using the $v = 1$ X state constants [94], a 0-1 line list was calculated (Table 6). For line strengths, the Einstein $A_{J' \to J''}$ values calculated by PGOPHER are

provided and also converted [1] to oscillator strengths $f_{J' \to J''}$ using,

$$f_{J' \to J''} = \frac{1.499194}{\tilde{v}^2} \frac{2J'+1}{2J''+1} A_{J' \to J''} \tag{109}$$

with $\tilde{v}$ in cm^{-1}.

The errors in the calculated line positions are estimated to be about ± 0.005 cm^{-1} based on the A - X analysis [94] and the new E - X analysis using the calibrated TiO cross sections [93]. The accuracy of the line strengths are more difficult to assess, but the lifetime on which the calculations are based has an accuracy of 4% [86]. This value, however, is a lower limit because it does not include systematic errors in the measurement and in the calculation. The most recent ab initio calculation (MRCI/aug-cc-pVQZ) has an E - X transition moment of 0.584 D [12] or 0.502 D using the 0-0 Franck-Condon factor of 0.86. The ExoMol calculation is thus 15% less than the experimental value."[80]

CHAPTER 9

VISIBLE OPACITY OF M DWARFS AND HOT JUPITERS:

THE TITANIUM MONOXIDE $B^3\Pi$-$X^3\Delta$ BAND SYSTEM

The findings and the material presented in this section are published in The Astrophysical Journal (Cameron & Bernath [97]). I am the corresponding author, I did the rotational analysis to include developing the line list and spectroscopic constants, which also generated the figures and tables in the paper, and I wrote the text. Peter Bernath (Old Dominion University) is the coauthor and project advisor, he also edited the paper. This work is original and was not published anywhere prior to its publication in The Astrophysical Journal.

9.1 INTRODUCTION

"The TiO molecule has a long and significant astronomical history. Its fluted spectral lines were noted by Fowler (1907) [2] in the spectra of Antarian stars, and its spectrum has been used as part of the Morgan Keenan (MK) classification system [3]. For M dwarf stars, the most numerous star type in our galaxy, the spectra are marked with strong absorption features due to TiO [82].

The near-IR and visible electronic transition spectra of TiO have been explored in sunspots [94] and in embedded protostars [98]. The pure rotational microwave transitions of TiO have been detected in red supergiants, supporting the concept that titanium oxides are formed in circumstellar envelopes and seed inorganic dust formation [99]. Its importance continues to expand as we explore exoplanets, where it has been detected by its electronic spectra and shown to cause formation of stratospheres in hot Jupiters [4, 84].

TiO is particularly important as a strong source of opacity in the visible and near-IR [85]. Therefore, accurate TiO line lists are essential in successfully modeling the spectra of many astronomical objects. The current ExoMol line list for TiO [12] remains the most reliable overall. Instead of using a Hamiltonian approach based on spectroscopic constants as this research does, the ExoMol line list is generated from potential energy curves using the DUO program [95]. The line list contains the $^{46}Ti^{16}O$, $^{47}Ti^{16}O$, $^{48}Ti^{16}O$, $^{49}Ti^{16}O$, and $^{50}Ti^{16}O$ isotopologues of TiO with 30 million transitions for $^{48}Ti^{16}O$. Laboratory spectroscopy is essential in the continuing effort to expand and improve the TiO line list.

A good recent summary of the state of laboratory spectroscopy of TiO research is provided by McKemmish et al. [85]. Efforts taken by our group since that summary include a reanalysis of the TiO singlet transitions (Bittner & Bernath 2018) [100], the $C^3\Delta$ - $X^3\Delta$ transition (Hodges & Bernath 2018) [101], high-resolution absorption cross sections in the visible and near IR (Bernath 2020) [93] and the $E^3\Pi$ - $X^3\Delta$ transition in the near-IR (Bernath & Cameron 2020) [80]. The $B^3\Pi$ - $X^3\Delta$ transition (γ' system) contains strong lines and is a dominant feature of late-type stars [102]. The B - X 0-0, 1-0, 0-1, and 1-1 bands were previously studied by emission spectroscopy, revealing significant lambda doubling in the $B^3\Pi$ state, and provided molecular constants for the $v = 0$ and $v = 1$ levels of the $B^3\Pi$ and $X^3\Delta$ states [102]. The B - X 1-0 band was revisited and updated by the laser spectroscopy of a molecular beam [103]. Through Stark spectroscopy, the permanent electric dipole moments of the $B^3\Pi_0$ and $X^3\Delta_1$ states along with the $E^3\Pi_0$ and $A^3\Phi_2$ were measured [91]. The IR spectrum of $^{46-50}$TiO was measured around 1000 cm^{-1} using a laser ablation source probed by IR radiation produced by quantum cascade lasers [104].

The starting point for our $B^3\Pi$ - $X^3\Delta$ analysis is the study of the $A^3\Pi$ - $X^3\Delta$ system by Ram et al. [94], which provided the equilibrium constants for the $X^3\Delta$ state, the spectroscopic constants for $v = 0 - 4$ of the X state, and the constants for $v = 1$ of the B state. The data were obtained from laboratory and sunspot spectra recorded using a Fourier transform spectrometer."[97]

9.2 METHOD AND RESULTS

"The TiO experimental cross sections [93] used in this analysis are based on the same emission spectrum recorded at the McMath-Pierce Solar Telescope using the 1 m Fourier transform spectrometer operated by the National Solar Observatory at Kitt Peak, Arizona that was used by Bernath & Cameron [80] for their $E^3\Pi$ - $X^3\Delta$ work. The source, a carbon tube furnace operating at about 2300 K, and the method of conversion of the emission spectrum to calibrated cross sections are described in detail by Bernath [93]. The spectral resolution is about 0.05 cm^{-1} with wavenumber calibration accuracy $\pm$0.002 cm^{-1}. Figure 45 shows the cross sections in red pointing upwards with the simulation pointing downwards showing the $B^3\Pi$ - $X^3\Delta$ 0–0, 1–0, and 2–1 bands (green) and the $A^3\Pi$ - $X^3\Delta$ 2–0 band (blue).

The $B^3\Pi$ and $X^3\Delta$ states obey Hund's case (a) coupling. The B - X transition has three spin components: $B^3\Pi_2$ - $X^3\Delta_3$, $B^3\Pi_1$ - $X^3\Delta_2$, and $B^3\Pi_0$ - $X^3\Delta_1$. The state labels of the spin components are for $^3\Pi$: $F_3 = {}^3\Pi_2$, $F_2 = {}^3\Pi_1$, $F_1 = {}^3\Pi_0$; the following are for $^3\Delta$: $F_3 = {}^3\Delta_3$,

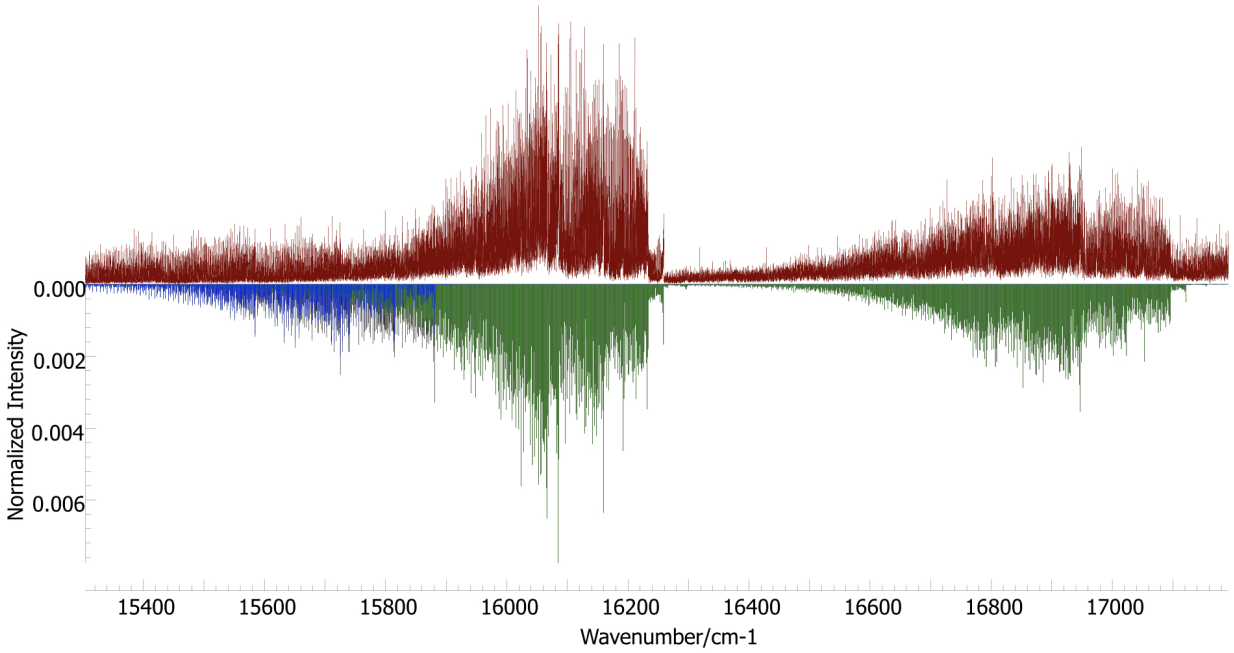

FIG. 45: TiO spectrum in red pointing upwards, simulation pointing downwards showing the 0–0, 1–0, and 2–1 $B^3\Pi$ - $X^3\Delta$ bands in green [97].

Note: The $B^3\Pi$ - $X^3\Delta$ 0–0 band is to the left, running from about 15800–16200 cm^{-1}; the 1–0 and 2–1 bands are intermixed to the right, running from about 16200–17100 cm^{-1}. The 2–0 $A^3\Pi$ - $X^3\Delta$ band is also shown pointing downwards in blue.

TABLE 7: R Band head Locations for the TiO $B^3\Pi$ - $X^3\Delta$ Transition [97].

Transition	Bandhead	0–0 (cm^{-1})	1–0 (cm^{-1})	2–1 (cm^{-1})
$B^3\Pi_{0^+} - X^3\Delta_1$	R_{1e}	16233.19	17096.31	16957.91
$B^3\Pi_{0^-} - X^3\Delta_1$	R_{1f}	16231.79	17095.00	16956.66
$B^3\Pi_1 - X^3\Delta_2$	R_{2e}	16160.04	17023.30	16885.39
$B^3\Pi_1 - X^3\Delta_2$	R_{2f}	16160.23	17023.50	16885.62
$B^3\Pi_2 - X^3\Delta_3$	R_{3e}	16085.46	16947.29	16809.36
$B^3\Pi_2 - X^3\Delta_3$	R_{3f}	16085.87	16947.59	16809.60

$F_2 = {}^3\Delta_2$, and $F_1 = {}^3\Delta_1$ [1]. Each sub-band has P, Q, and R branches, and each branch has "e" and "f" parities due to lambda doubling. The R-branch band heads for the 0–0, 1–0, and 2–1 bands of the $B^3\Pi$ - $X^3\Delta$ transition are listed in Table 7. Figure 46 shows the $B^3\Pi_0$ - $X^3\Delta_1$ R band heads.

The PGOPHER program [19] was used to perform the rotational analysis of the TiO B - X transition. The process started with $B^3\Pi$ equilibrium constants from Amiot et al. [105], which were used to calculate case (a) v state constants for $v = 0$ through v=4, using Ram et al. [94] $v = 1$ constants as a benchmark. For the $X^3\Delta$ constants, Ram et al. [94] was again used. Ram et al. [94] improved the existing ground state constants by combining sunspot and laboratory spectra with the pure rotational measurement of Steimle et al. [106] and Namiki et al. [107]. The cross section file was used as an overlay in PGOPHER. Spectroscopic constants were updated as lines were fit up to J of at least 100. Attempts were made to fit lines in the 3–2 band, but the region of the spectrum was so congested the fit was not deemed reliable. In the rotational analysis, 5507 lines were fitted with an average error of 0.024 cm^{-1}. The TiO line database presented by McKemmish et al. [12] includes the five stable isotopologues: $^{46}Ti^{16}O$, $^{47}Ti^{16}O$, $^{48}Ti^{16}O$, $^{49}Ti^{16}O$, and $^{50}Ti^{16}O$. The telluric abundances of ^{46}Ti, ^{47}Ti, ^{48}Ti, ^{49}Ti, and ^{50}Ti are 8.25%, 7.44%, 73.72%, 5.41%, and 5.18% respectively [108]. The minor isotopologues are clearly present in the experimental spectrum from Kitt Peak but did not complicate the analysis of the most abundant isotopologue.

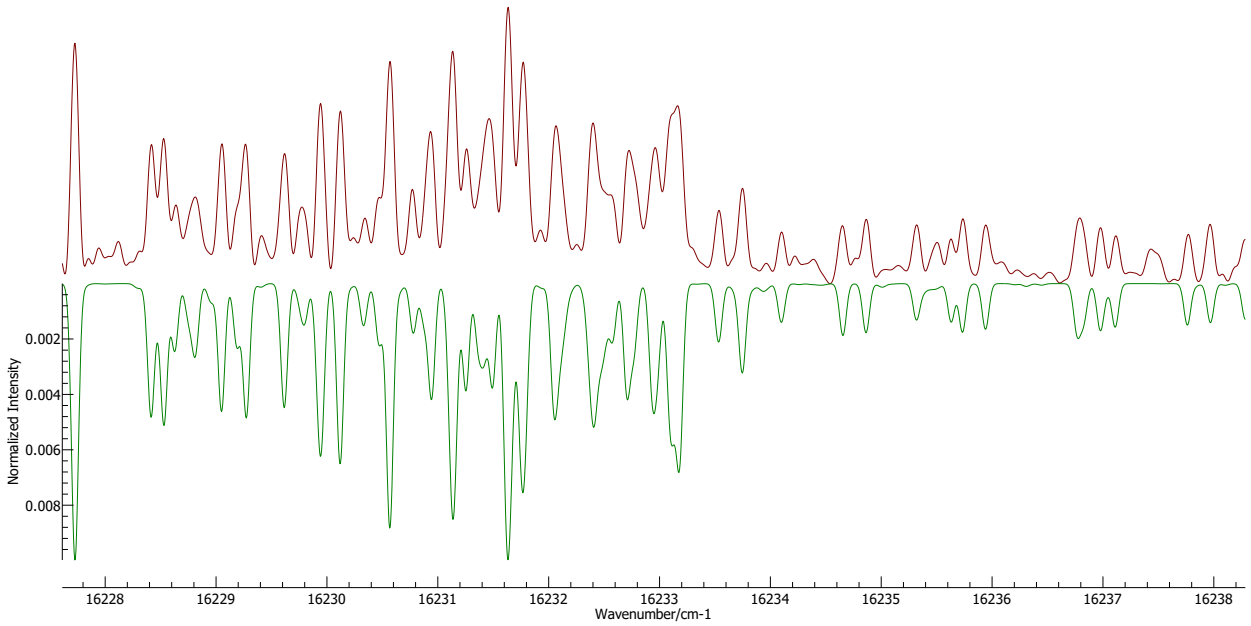

FIG. 46: TiO $B^3\Pi$ - $X^3\Delta$ spectrum in red pointing upwards, simulation pointing downwards in green, showing the 0–0 R_1e bandhead at about 16233.2 cm^{-1} and the 0–0 R_1f bandhead at about 16231.8 cm^{-1} [97].

Rotational analysis of the four minor isotopologues of TiO is a topic of our ongoing research. New spectroscopic constants resulting from the rotational analysis for $v = 0$ though $v = 2$ of the B state are provided in Table 8.

The reader may note the H_v value for $v = 2$ appears to be anomalous; thorough investigation of the constant through PGOPHER shows it to be stable with small relative standard deviation. Higher-order lambda-doubling centrifugal distortion terms were statistically determined for the B state due to large lambda doubling in the B - X transition. It is possible global perturbations exist, but no local perturbations were discovered. The standard N^2 Hamiltonian [94] was used for fitting.

New equilibrium constants are provided in Table 9. The equilibrium constants were derived by the exact fit of the PGOPHER generated spectroscopic constants. The number of decimal places shown in the equilibrium constants was determined by allowing a ± 1 standard deviation in the value of the spectroscopic constants. The equilibrium constants were input into Le Roy's Rydberg-Klein-Rees (RKR) program [20] to generate the potential energy curves for the B and X states, which were then inserted into Le Roy's LEVEL program [21], along with the transition-dipole moment points, to generate transition-dipole moment matrix elements. The transition-dipole moment points for the B - X transition were obtained from McKemmish et al. [12], who fit a curve to their own *ab initio* data as well as the *ab initio* data of Langhoff [109]. The functional form of the fit for the transition-dipole μ is [12]

$$\mu_{fit}(r) = \frac{c}{2\pi}\left(\pi + 2\tan^{-1}(-a(r - r_m))\right), \tag{110}$$

in which c, a, and r_m are fitting paramters; for the B - X transition, $c = 5.013$, $a = 4.101$ and $r_m = 1.667$. Excel was used to calculate 317 transition-dipole moment points for $r =$ 0.84–2.42 Å.

The average radiative lifetime of the three spin states of the $v = 0$ B state was measured to be 65.4 ± 1.3 ns [110]. The Einstein A for the $v = 0$ B state can be calculated, with the calculated lifetime τ for the state being

$$\tau = \frac{1}{\sum A_{0\to v''}}. \tag{111}$$

The Einstein A is linked to line strength through the following relationship:

$$A_{v'\to v''} = 3.136189 \times 10^{-7}\tilde{v}^3 S_{v'\to v''} \tag{112}$$

where $\tilde{v}$ is cm^{-1} [1]. The line strength S is the square of the transition-dipole moment. The transition-dipole moment matrix elements were obtained from the LEVEL program.

TABLE 8: Spectroscopic Constants for the $v = 0$ through $v = 2$ Levels of the $B^3\Pi$ State in cm^{-1} [97].

Constant	$v = 0$	$v = 1$	$v = 1$ (Ram et al. 1999)	$v = 2$
T_v	16148.4377(16)	17012.4714(14)	17012.463041(147)	17874.6285(14)
B_v	0.5060425(16)	0.50286131(71)	0.502865409(228)	0.49966314(81)
$D_v \times 10^7$	6.8913(41)	6.89443(93)	6.90626(113)	6.4812(13)
$H_v \times 10^{14}$	7.4(29)	0.84(33)	9.82(142)	-2153.09(59)
A_v	20.3851(21)	20.7817(21)	20.788469(223)	21.2050(20)
$A_{Dv} \times 10^4$	-1.65(28)	0.47(19)	-1.1437(257)	-2.41(22)
$A_{Hv} \times 10^9$	-6.51(43)	-6.26(12)	-6.446(105)	-4.96(35)
$\gamma_v \times 10^2$	2.333(56)	2.819(40)	2.49139(521)	2.2831(471)
λ_v	-0.7900(23)	-0.9329(23)	-0.93069(235)	-1.0733(22)
$\lambda_{Dv} \times 10^5$	-0.099(61)	-1.147(33)	-0.3826(658)	2.21(14)
$\lambda_{Hv} \times 10^8$	...	...	-0.0519(161)	-1.8761(88)
o_v	-0.6582(21)	-0.6139(22)	-0.618623(260)	-0.5800(24)
$o_{Dv} \times 10^6$	4.74(93)	-4.91(97)	1.918(427)	12.2(13)
$o_{Hv} \times 10^{10}$	...	5.14(53)	...	-19.53(98)
$p_v \times 10^2$	2.5573(65)	2.6156(67)	2.611711(933)	2.7552(81)
$p_{Dv} \times 10^8$	8.80(91)	6.4(13)	...	29.9(22)
$p_{Hv} \times 10^{12}$	...	3.58(63)	...	-3.6(14)
$q_v \times 10^4$	2.909(18)	3.062(11)	2.95986(352)	3.050(14)
$q_{Dv} \times 10^{10}$	-3.6(14)	-6.88(41)	...	-223.75(77)

Note: Numbers in parentheses are uncertainties to 1 standard deviation. Additional $v = 1$ values from Ram et al. 1999 [94] included for reference.

TABLE 9: Equilibrium Constants for the $B^3\Pi$ State in cm^{-1} [97].

Constant	New Values	(Amiot et al. 2002)
ω_e	865.91124	865.87593
$\omega_e x_e$	0.93876	0.924582159
B_e	0.50762697	0.50763(388)
$\alpha_e \times 10^3$	3.16477	3.179246
$\gamma_e \times 10^6$	−8.23	···

Note: Amiot et al. 2002 [105] values included for reference.

Comparing the calculated radiative lifetime of 122.3 ns to the measured radiative lifetime shows that a correction factor of 1.87 must be applied to the calculated Einstein A values. The calculated transition-dipole moment matrix elements obtained from the LEVEL program were corrected by applying a scaling factor of $\sqrt{1.87}$ to make this correction to the PGOPHER band strengths. Based on the experimental accuracy of 2.0% for the lifetime of $v = 0$ [110], the minimum error for calculated Einstein A values is also about 2%. The scaled transition-dipole moment matrix elements are shown in Table 10."[97]

9.3 DISCUSSION

"The spectroscopic constants (Table 8) extend the previously published $v' = 1$ constants of Ram et al. [94] to also include $v' = 0$ and $v' = 2$. A sample of the lines fitted and the observed-minus calculated values are given in Table 11. Table 11 uses the traditional spectroscopic line label: ${}^{\Delta N}\Delta J_{F_i' F_j''} p(J)$ where N is the quantum number for the total angular momentum excluding electron spin, J is the quantum number for the total angular momentum, p is the e/f rotationless parity, and F_i is the spin component label discussed in the previous section. In addition, the line assignment information in Table 11 uses the PGOPHER $NameJNFnp$ format.

Through this analysis, the equilibrium constants (Table 9) of the $B^3\Pi$ state [105] have also been updated. McKemmish et al. [12] noted that future improvements on the TiO line list should concentrate on wavelength regions such as 570-640 nm (15625–17544 cm^{-1}),

TABLE 10: Scaled Transition-dipole Moment Matrix Elements for the $B^3\Pi$ - $X^3\Delta$ Transition in Debye [97].

Band $v' - v''$	Transition-dipole Moment Matrix Element (debye)
0–0	3.08127
1–0	−2.01087
2–0	0.93507
0–1	1.44348
1–1	2.03017
2–1	−2.32573
0–2	0.46731
1–2	1.69027
2–2	1.15678
0–3	0.12070
1–3	0.71320
2–3	1.69059
0–4	$2.40917x10^{-2}$
1–4	0.218792
2–4	0.885716

TABLE 11: Sample of Fitted Lines for the $B^3\Pi$ - $X^3\Delta$ Transition Baseed on the PGOPHER Log File [97].

J'	P'	J''	P''	Obs (cm^{-1})	Calc (cm^{-1})	O-C (cm^{-1})	Line
3	f	3	e	16225.3072	16225.3166	-0.0094	qQ1(3)
4	f	4	e	16224.9672	16224.9628	0.0044	qQ1e(4)
5	e	5	f	16793.445	16793.43	0.015	qQ3f(5)
62	e	62	f	16890.5924	16890.5999	-0.0075	qQ2f(62)
10	e	11	e	16210.8103	16210.8135	-0.0032	pP1e(11)
85	f	86	f	16545.7223	16545.7023	0.02	pP2f(86)
11	f	10	f	16077.8369	16077.8404	-0.0035	rR3f(10)
102	f	101	f	16829.3663	16829.3996	-0.0333	rR1f(101)

Note: J is total angular momentum; p is the e/f parity; Obs is the observed line position in cm^{-1}; Calc is the calculated line position in cm^{-1}; O - C is the observed minus calculated line position in cm^{-1}; Line is the spectroscopic line label; Line Assignment contains additional information.

(This table is available in its entirety in machine-readable form.)

TABLE 12: Sample Table for Line List for the $B^3\Pi$ - $X^3\Delta$ Transition of TiO [97].

J'	J''	Pos	Eup	Elow	A (s^{-1})	f	Line
21	20	17022.517	17245.485	222.968	8.922×10^5	4.841×10^{-3}	rR2f(20)
10	9	17022.522	17069.345	46.823	9.208×10^5	5.265×10^{-3}	rR2e(9)
28	28	17022.572	17454.600	432.027	6.563×10^5	3.395×10^{-3}	rQ32f(28)
20	19	17022.582	17224.206	201.624	9.027×10^5	4.910×10^{-3}	rR2e(19)
57	58	17022.588	18726.276	1703.689	1.273×10^4	6.474×10^{-5}	rP31e(58)
10	9	17022.646	17069.470	46.823	9.197×10^5	5.259×10^{-3}	rR2f(9)
41	41	17022.704	17832.655	809.950	2.486×10^6	1.286×10^{-2}	qQ1f(41)
11	10	17022.800	17080.303	57.503	9.337×10^5	5.291×10^{-3}	rR2e(10)

Note: J is total angular momentum; Pos is the line position in vacuum cm^{-1}; Eup and Elow are upper and lower energy levels in cm^{-1}; A is Einstein A value in s^{-1}; f is the oscillator strength; Line is the spectroscopic line label.
(This table is available in its entirety in machine-readable form.)

which is coincident with the $B^3\Pi$ - $X^3\Delta$ 0–0, 1–0, and 2–1 bands that are the focus of this research. Using the $X^3\Delta$ spectroscopic constants for $v'' = 0$ through $v'' = 4$ from Ram et al. [94] and the new $B^3\Pi$ spectroscopic constants from Table 8, a new line list for the $B^3\Pi$ - $X^3\Delta$ transition has been calculated; a sample of that line list is shown in Table 12. The same line and line assignment formats used in Table 11 are used in Table 12.

The transition-dipole moment matrix elements shown in Table 10 were used in PGOPHER as band strengths to obtain a more complete line list. In addition, the oscillator strength for each line, $f_{J' \leftarrow J''}$, was calculated from the Einstein A values, which are provided for each line by PGOPHER, using the following:

$$f_{J' \leftarrow J''} = \frac{\epsilon_0 m_e c^3}{2\pi e^2 v^2} \frac{2J'+1}{2J''+2} A_{J' \rightarrow J''}, \tag{113}$$

where SI units are used. In terms of numerical values, the equation becomes

$$f_{J' \leftarrow J''} = \frac{1.499194}{\tilde{v}^2} \frac{2J'+1}{2J''+2} A_{J' \rightarrow J''}, \tag{114}$$

with $\tilde{v}$ in cm^{-1} [1].

The line list was compared with both the ExoMol line list and Amiot et al. [103]. As noted by Bernath [93], the 0-0 band in the ExoMol line list agrees well with the measured cross sections down to about 16200 cm^{-1}, below that wavenumber missing/shifted lines and intensity errors begin to appear. 16200 cm^{-1} marks the upper (low J) end of the 0–0 band. A slightly more detailed analysis shows occasional errant lines from 16200 down to about 16050 cm^{-1} at which point they become more commonplace, roughly around $J = 60$. The 0–0 band is the ideal comparison between this research and the ExoMol line list in that it is somewhat isolated as opposed to the region where the 1–0, 2–1, and 3–2 bands are mostly overlaid, making unique line identification often challenging. From about 17100 cm^{-1} down to about 17000 cm^{-1}, the 1–0 band is relatively isolated; J values are typically below 60, and both the line list generated here and the ExoMol line list are in good agreement with the measured cross sections. Comparing the line list from this research with the Amiot et al. [103] line list, which encompasses the 1–0 band from $J = 1$–100, a subset from all three branches, both the parities and J values ranging from 5 to 100 show an average difference of less than 0.005 cm^{-1}." [97]

9.4 CONCLUSION

"The new TiO $B^3\Pi$ - $X^3\Delta$ line list derived from the TiO emission spectrum recorded at the McMath-Pierce Solar Telescope, operated by the National Solar Observatory at Kitt Peak, Arizona in 1985 January [93] improves on the existing data. New spectroscopic constants for $v' = 0$–2 in the B state have been produced, expanding the existing constants from Ram et al. [94] and updating the equilibrium constants from Amiot et al. [103]. The fitted lines and the calculated line list for $v' = 0$–2 and $v'' = 0$–4, sampled in Tables 11 and 12 respectively, are available in their entirety as supplementary data files." [97]

CHAPTER 10

LINE LISTS FOR TITANIUM MONOXIDE MINOR ISOTOPOLOGUES FOR THE $A^3\Phi$ - $X^3\Delta$ ELECTRONIC TRANSITION

The findings and the material presented in this section were submitted for publication in the Journal of Quantitative Spectroscopy and Radiative Transfer on 16 February 2023 [111]. Peter Bernath (Old Dominion University) is the corresponding author and project advisor, he also edited the paper. I am the coauthor, I did the rotational analysis to include developing the line list and spectroscopic constants, which also generated the figures and tables in the paper, and I wrote the text. There was a discussion between Peter Bernath and me after the paper was completed regarding which of us should be the corresponding author, in that while I wrote the paper, his editing was more significant than typical. He was comfortable in my retaining the corresponding author role; we mutually decided he would be the corresponding author, with the deciding factor being that the paper would likely return from peer review just as I was in the midst of my dissertation defense. This work is original and was not published anywhere prior to its submission for publication in the Journal of Quantitative Spectroscopy and Radiative Transfer.

10.1 INTRODUCTION

"TiO is among the most prominent diatomic molecules from an astronomical perspective, given the early discovery of its spectral lines by Fowler in 1907 [2] and its strong presence in the visible and near infrared spectra of M dwarf stars [82]. The significance of TiO has increased with the exploration of exoplanets, where TiO has been shown to cause formation of stratospheres in hot Jupiters [4, 84]. Recent analysis of observations of oxygen-rich asymptotic giant branch (AGB) stars have revealed a significant presence of TiO as a possible precursor to dust [112]. Astronomical observations of TiO need to be supported by comprehensive line lists, which should be based on laboratory spectroscopy. The ExoMol TiO line list by McKemmish et al. [12] is currently the most comprehensive and reliable, with 30 million $^{48}Ti^{16}O$ transitions as well as predictions for the four minor isotopologues, derived for titanium's four minor isotopes: ^{46}Ti, ^{47}Ti, ^{49}Ti and ^{50}Ti with natural abundances on Earth of 8%, 7%, 5% and 5%, respectively. The ExoMol line list is calculated

from potential energy curves using the DUO program [95]. The potential energy curves were adjusted using experimental data and calculated line positions were replaced by calculated values from experimentally derived term values, if available.

A thorough summary of TiO laboratory spectroscopy for the $^{48}Ti^{16}O$ molecule was made by McKemmish et al. [85]. Since then, our group has continued to improve TiO laboratory spectroscopy; those efforts include analysis of singlet transitions [100], the $C^3\Delta$ - $X^3\Delta$ transition [101], absorption cross sections in the visible and near IR [93], the $E^3\Pi$ - $X^3\Delta$ transition [80] and the $B^3\Pi$ - $X^3\Delta$ transition [97].

The isotopes of Ti have different nucleosynthetic origins: oxygen and silicon burning in massive stars yields ^{46}Ti and ^{47}Ti, $^{48-50}$Ti are formed mainly in supernova explosions [113]. Determining the relative abundances of isotopes and understanding the processes that form the various isotopes can potentially lead to determining the formation and evolution of astronomical objects [114]. The relative abundances of Ti isotopes of two M dwarf stars were measured by Pavlenko et al. [115] using the ExoMol line list. They found that $^{46-48}$Ti abundances were reduced by a few % and $^{49-50}$Ti abundances were increased by a few % relative to solar abundances. Current large telescopes with high resolution spectrographs such as the VLT/RISTRETTO and those coming such as the ELT/ANDES can easily determine the relative TiO abundances of young gas giant exoplanets [114]. We present here the results of rotational analysis of the minor TiO isotopologues, through laboratory spectroscopy, providing improvement to existing line lists."[111]

10.2 METHOD AND RESULTS

"The rotational analysis of the minor isotopologues of the TiO molecule $A^3\Phi$ - $X^3\Delta$ transition was carried out with the PGOPHER program [19], using as an overlay the same TiO experimental cross sections, recorded at McMath-Pierce Solar Telescope at Kitt Peak, AZ in 1985, that were used by Bernath & Cameron [80] and Cameron & Bernath [97]. The source for the emission spectrum is a carbon tube furnace operated at about 2300 K; the conversion of the spectrum to calibrated cross sections is detailed by Bernath [93]. Wavenumber calibration accuracy for the cross sections is ± 0.002 cm^{-1} and the spectral resolution is about 0.05 cm^{-1}. In addition, low J line positions for the 0-0 band of all four minor isotopologues from Barnes et al. [116] were manually added to the PGOPHER fit.

The states in the $A^3\Phi$ - $X^3\Delta$ transition obey Hund's case (a) coupling; each vibrational band has 3 subbands due to the three spin components, and each subband has P, Q and R branches, with no Λ-doubling. Figure 47 shows an overview of the 0-1 band; the cross

sections are in red, pointing up, and the simulation is pointing down. Figure 48 shows an expanded portion of the 0-0 band, allowing a better view of the faithfulness of the simulation. In general, the stronger lines are generated by the main $^{48}Ti^{16}O$ isotopologue, and the weaker lines are from the minor isotopologues, as demonstrated in Figure 49, where the main isotopologue simulation is pointing downwards in black, and the minor isotopologues are color coded as described in the figure caption. Note the line strengths in Figures 47 through 50 were set manually in PGOPHER to match the line strengths of the cross sections, not calculated. The most prominent feature in Figure 49, at 14155.7 cm^{-1}, is expanded in Figure 50 to get a better sense of the distribution of the lines of the different isotopologues. The same color scheme introduced in Figure 49 is continued in Figure 50. It can be seen the feature at 14155.7 stands out because it is a merger of two lines of the major $^{48}Ti^{16}O$ isotopologue, specifically an R(39) line and a Q(15) line. It can be seen that the same two lines are merged into a single feature for all five isotopologues, which appear in order by mass starting with the $^{46}Ti^{16}O$ isotopologue on the left progressing through the $^{50}Ti^{16}O$ isotopologue on the right. In the rotational analysis, 8233 lines from 0-0 and 0-1 bands were fit across the four minor isotopologues with an average observed minus calculated error of 0.013 cm^{-1}. These observed lines are provided in Supplementary Table 1.

To begin the analysis, initial spectroscopic constants for both the $A^3\Phi$ and $X^3\Delta$ states for the major $^{48}Ti^{16}O$ isotopologue were obtained from Ram et al. [94]. Ram et al. [94] provide equilibrium constants in a power series. These equilibrium constants were scaled for the different atomic masses of the four minor isotopologues using the following usual relationship from Bernath [1]:

$$Y_{jk} \propto \mu^{-(j+2k)/2}, \tag{115}$$

in which Y_{jk} is a Dunham parameter and μ is the reduced mass.

Bernath [1] also details the relationship between Dunham parameters and conventional spectroscopic constants using customary energy level expressions to obtain the origin, B, D, and H constants. The A, A_D, λ and λ_D spin-orbit and spin-spin initial constants were obtained from similar Dunham-like expansion parameters provided by Ram et al. [94]. There is no isotopic dependence for A or λ, but A_D and λ_D were scaled with the same isotopic dependence as B. The derived equilibrium constants are shown in Tables 13-15.

The equilibrium constants were used to generate initial values for the spectroscopic constants for $v = 0$ through $v = 4$ for both the $A^3\Phi$ and $X^3\Delta$ states (available as supplementary files, see Appendix B). These initial constants were used to start the analysis of the isotopologue lines in the 0-0 and 0-1 bands. The ground state constants were held fixed to the

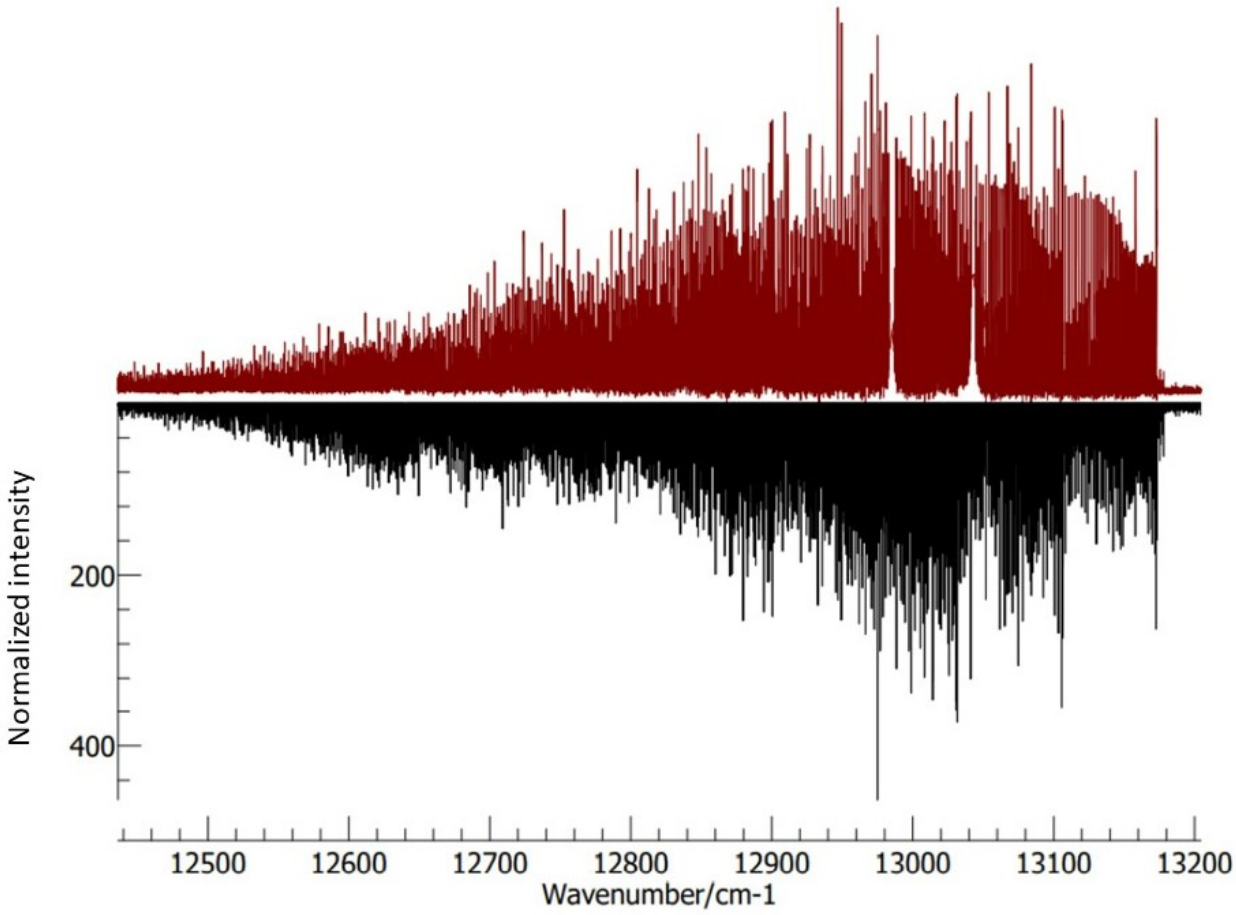

FIG. 47: TiO spectrum, a portion of the $A^3\Phi$ - $X^3\Delta$ transition 0-1 band, in red pointing upwards, simulation pointing downwards [111].

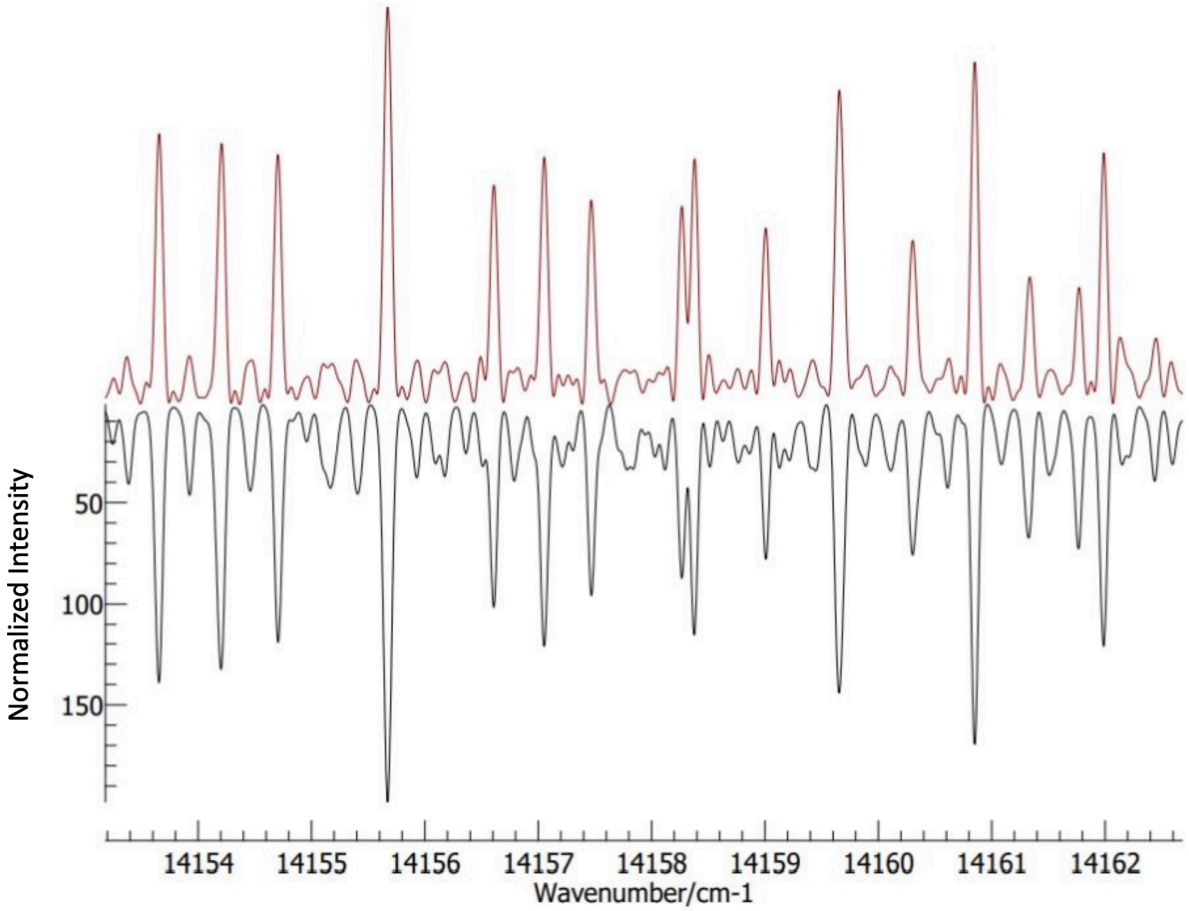

FIG. 48: TiO spectrum, an expanded portion of the $A^3\Phi$ - $X^3\Delta$ transition, 0-0 band, highlighting the accuracy of the simulation, pointing downwards [111].

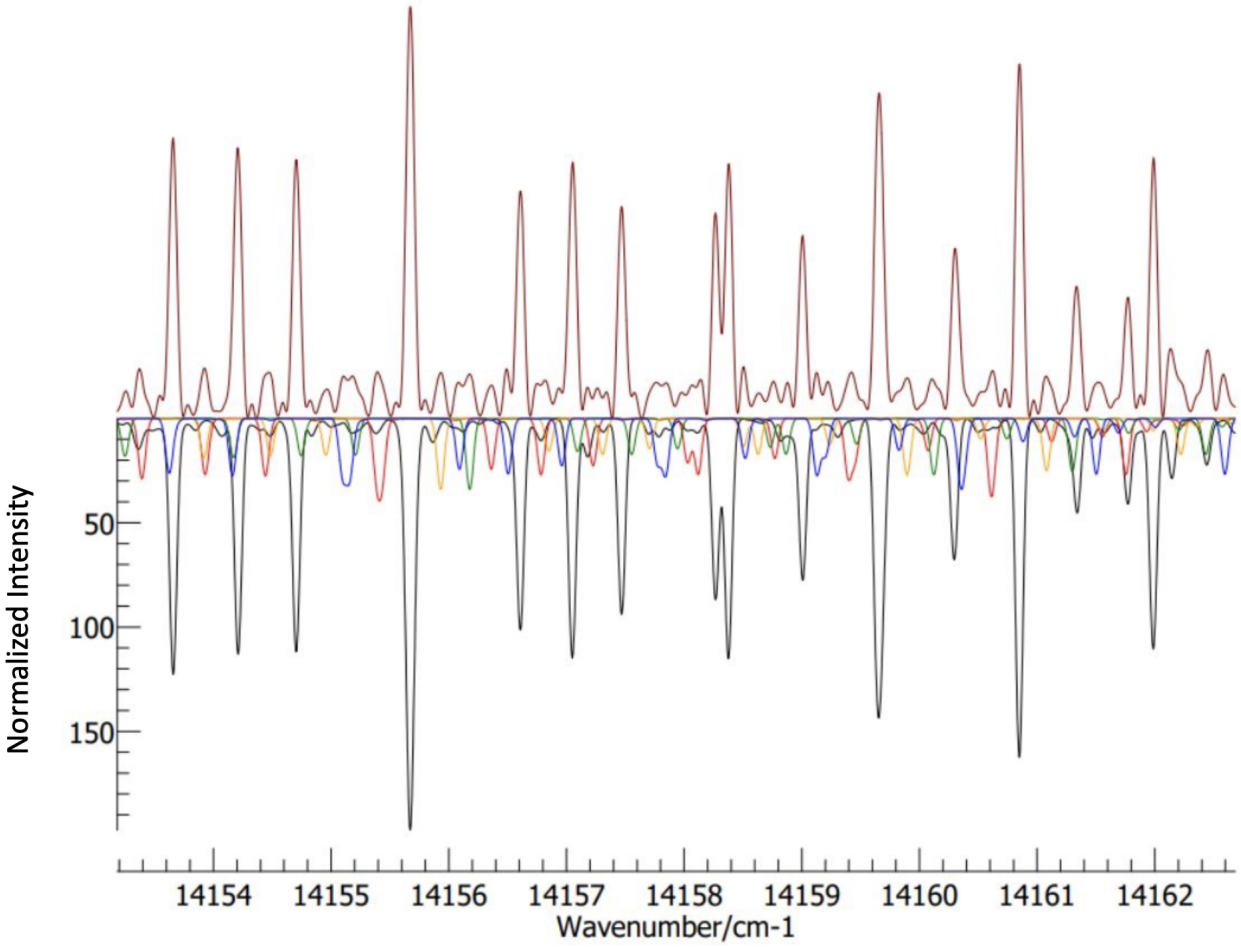

FIG. 49: The same portion of the $A^3\Phi$ - $X^3\Delta$ transition, 0-0 band, depicted in Figure 48, with color coding added to show the isotopologues that comprise the features [111].
Note: Blue is $^{46}Ti^{16}O$, red is $^{47}Ti^{16}O$, black is $^{48}Ti^{16}O$, orange is $^{49}Ti^{16}O$ and green is $^{50}Ti^{16}O$.

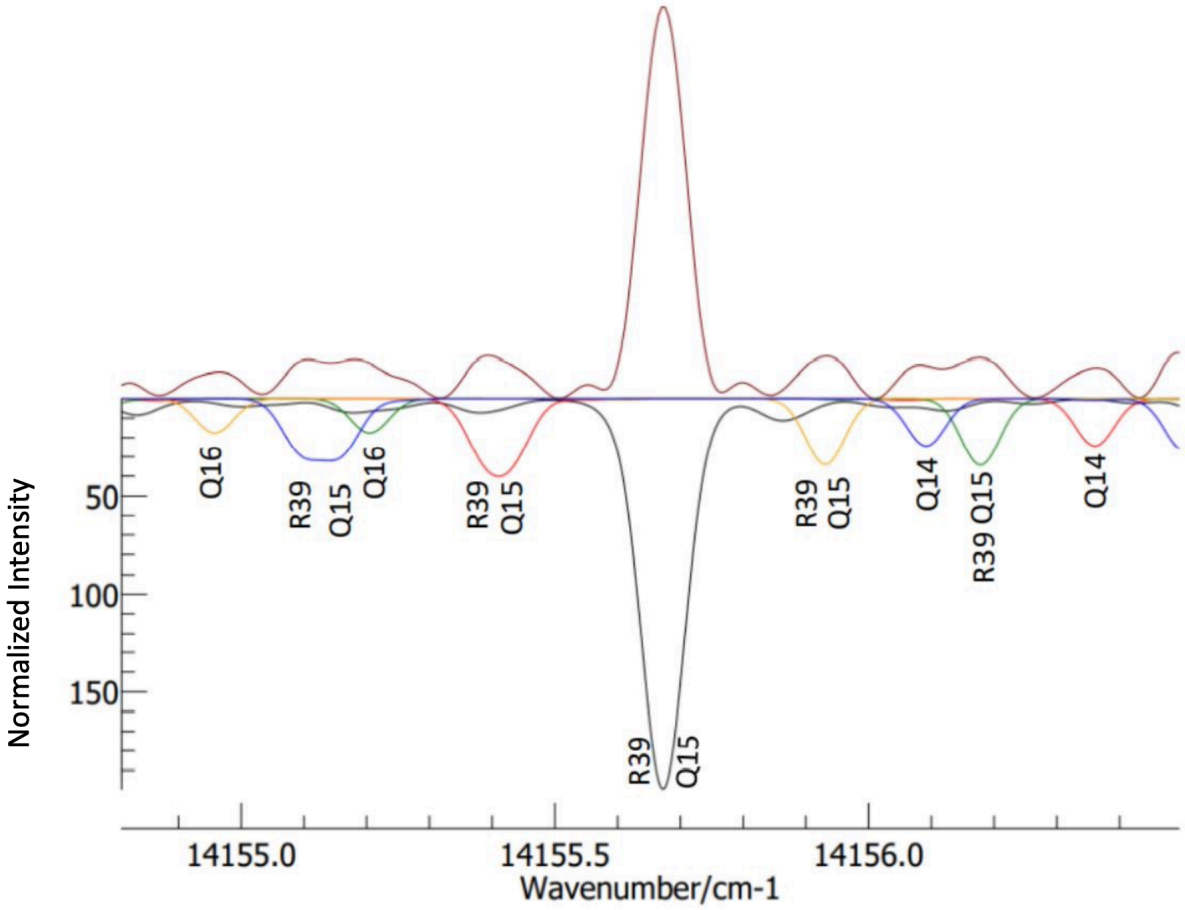

FIG. 50: Expanded view of the prominent feature in Figure 49 at 14155.7 cm^{-1} [111]. Note: Lines composing the features are labelled. Color coding as in Figure 49.

TABLE 13: Equilibrium constants for the TiO minor isotopologue $X^3\Delta$ and $A^3\Pi$ states in cm^{-1} derived from Ram et al. [94, 111] $^{48}Ti^{16}O$ constants, which are included for reference in Table 14. [111].

P_v	p_0	p_1	p_2	p_3
$^{46}Ti^{16}O$ $X^3\Delta$ State				
T_v	0	1014.642232	-4.611283418	-3.843378E-03
B_v	0.541149919	-0.003073155	-9.4132E-06	0
D_v	6.15486E-07	3.50849E-09	3.30541E-11	0
H_v	7.10663E-14	0	0	0
A_v	50.650414	0.001944475	-8.852114E-04	0
A_{Dv}	-2.61946E-05	-1.1199E-06	0	0
λ_v	1.749911	-0.005449355	3.031574E-04	0
λ_{Dv}	6.79703E-07	0	0	0
$^{46}Ti^{16}O$ $A^3\Phi$ State				
T_v	14163.554562	872.215449	-3.875084	-0.011903
B_v	5.128105E-01	-0.003218	-5.8797E-06	-3.5342E-07
D_v	7.082973E-07	1.119223E-09	1.7994E-10	0
H_v	1.180650E-13	0	0	0
A_v	58.010058	-1.064333E-01	0.001214	0
A_{Dv}	-4.246629E-05	2.640442E-07	0	0
λ_v	-5.163460E-01	3.068530E-03	-0.000249	0
λ_{Dv}	-4.534320E-06	1.965595E-07	0	0

Note: The Ram et al. [94] format had been replicated: $P_v = \sum_{k=0}^{3} p_k (v + \frac{1}{2})^K$. For $P_v = T_v$, $p_0 = T_e$, $p_1 = \omega_e$, $p_2 = \omega_e x_e$, $p_3 = \omega_e y_e$; for $P_v = B_v$, $p_0 = B_e$, $p_1 = -\alpha_e$, $p_2 = \gamma_e$, etc.

TABLE 14: Continuation of equilibrium constants for the TiO minor isotopologue $X^3\Delta$ and $A^3\Pi$ states in cm^{-1} derived from Ram et al. [94] $^{48}Ti^{16}O$ constants, which are included for reference [111].

P_v	p_0	p_1	p_2	p_3
$^{47}Ti^{16}O$ $X^3\Delta$ State				
T_v	0	1011.850914	-4.585946703	-0.003811745
B_v	0.538176569	-3.047862E-03	-9.31004E-06	0
D_v	6.08741E-07	3.46049E-09	3.25122E-11	0
H_v	6.99013E-14	0	0	0
A_v	50.650414	1.939125E-03	-8.803476E-04	0
A_{Dv}	-2.60506E-05	-1.11068E-06	0	0
λ_v	1.749911	-5.434364E-03	3.014917E-04	0
λ_{Dv}	6.75969E-07	0	0	0
$^{47}Ti^{16}O$ $A^3\Phi$ State				
T_v	14163.554562	869.815953	-3.853792	-1.180466E-02
B_v	5.099929E-01	-3.191863E-03	-5.815239E-06	-3.485825E-07
D_v	7.005352E-07	1.103912E-09	1.769884E-10	0
H_v	1.161296E-13	0	0	0
A_v	58.010058	-1.061405E-01	1.207676E-03	0
A_{Dv}	-4.223296E-05	2.618710E-07	0	0
λ_v	-5.163460E-01	3.060088E-03	-2.480093E-04	0
λ_{Dv}	-4.509407E-06	1.949417E-07	0	0

Terms in parentheses for the source main $^{48}Ti^{16}O$ isotopologue equilibrium constants are 1 standard deviation.

$^{48}Ti^{16}O$ $X^3\Delta$ State				
T_v	0	1009.176435(654)	-4.561736(301)	-3.7816(420)E-03
B_v	0.535335360(164)	-3.023758(366)E-03	-9.2120(912)E-06	0
D_v	6.023307(870)E-07	3.4150(632)E-09	3.20(180)E-11	0
H_v	6.88(161)E-14	0	0	0
A_v	50.650414(100)	1.934(166)E-03	-8.757(350)E-04	0
A_{Dv}	-2.59131(267)E-05	-1.1019(524)E-06	0	0
λ_v	1.749911(138)	-5.420(258)E-03	2.999(568)E-04	0
λ_{Dv}	6.724(158)E-07	0	0	0
$^{48}Ti^{16}O$ $A^3\Phi$ State				
T_v	14163.554562(548)	867.516894(914)	-3.833447(453)	-1.17113(623)E-02
B_v	0.507300491(369)	-3.166620(701)E-03	-5.754(322)E-06	-3.440(406)E-07
D_v	6.931580E-07(107)	1.0894(805)E-09	1.742(265)E-10	0
H_v	1.143(168)E-13	0	0	0
A_v	58.0100584(943)	-0.1058600(935)	1.2013(169)E-03	0
A_{Dv}	-4.20100(328)E-05	2.598(324)E-07	0	0
λ_v	-0.516346(226)	3.052(234)E-03	-2.467(441)E-04	0
λ_{Dv}	-4.4856(813)E-06	1.934(546)E-07	0	0

TABLE 15: Continuation of equilibrium constants for the TiO minor isotopologue $X^3\Delta$ and $A^3\Pi$ states in cm^{-1} derived from Ram et al. [94] $^{48}Ti^{16}O$ constants [111].

P_v	p_0	p_1	p_2	p_3
$^{49}Ti^{16}O$ $X^3\Delta$ State				
T_v	0	1006.594674	-4.538425415	-3.752651E-03
B_v	0.532599783	-3.000610E-03	-9.118093E-06	0
D_v	5.96191E-07	3.37154E-09	3.15119E-11	0
H_v	6.77507E-14	0	0	0
A_v	50.650414	1.929052E-03	-8.712252E-04	0
A_{Dv}	-2.57807E-05	-1.09346E-06	0	0
λ_v	1.749911	-5.406134E-03	2.983675E-04	0
λ_{Dv}	6.68964E-07	0	0	0
$^{49}Ti^{16}O$ $A^3\Phi$ State				
T_v	14163.554562	865.297539	-3.813858	-1.162165E-02
B_v	0.504708	-3.142379E-03	-5.695344E-06	-3.396222E-07
D_v	6.860920E-07	1.075536E-09	1.715431E-10	0
H_v	1.125567E-13	0	0	0
A_v	58.010058	-0.105589	1.195161E-03	0
A_{Dv}	-4.179533E-05	2.578112E-07	0	0
λ_v	-0.516346	3.044192E-03	-2.454394E-04	0
λ_{Dv}	-4.462678E-06	1.919195E-07	0	0
$^{50}Ti^{16}O$ $X^3\Delta$ State				
T_v	0	1004.11736	-4.516114009	-3.725012E-03
B_v	0.529981463	-2.978511E-03	-9.02866E-06	0
D_v	5.90343E-07	3.33026E-09	3.10495E-11	0
H_v	6.67564E-14	0	0	0
A_v	50.650414	1.924305E-03	-8.669421E-04	0
A_{Dv}	-2.56539E-05	-1.085411E-06	0	0
λ_v	1.749911	-5.392829E-03	2.969007E-04	0
λ_{Dv}	6.65675E-07	0	0	0
$^{50}Ti^{16}O$ $A^3\Phi$ State				
T_v	14163.554562	863.167968	-3.795109	-1.153605E-02
B_v	0.502227	-3.119235E-03	-5.639484E-06	-3.354635E-07
D_v	6.793628E-07	1.062366E-09	1.690256E-10	0
H_v	1.109048E-13	0	0	0
A_v	58.010058	-0.105329	1.189286E-03	0
A_{Dv}	-4.158986E-05	2.559124E-07	0	0
λ_v	-5.163460E-01	3.036700E-03	-2.442327E-04	0
λ_{Dv}	-4.440739E-06	1.905060E-07	0	0

TABLE 16: Calculated spectroscopic constants for $A^3\Phi$ $v = 0$ [111].

	$^{46}Ti^{16}O$	$^{47}Ti^{16}O$	$^{48}Ti^{16}O$	$^{49}Ti^{16}O$	$^{50}Ti^{16}O$
T	14092.5242	14092.7191	14092.9059	14093.0861	14093.2591
B	0.5111999	0.5083955	0.5057157	0.4999806	0.5006659
D	7.089019E-07	7.011314E-07	6.937463E-07	6.880913E-07	6.799362E-07
H	1.180650E-13	1.161296E-13	1.143000E-13	1.125567E-13	1.109048E-13
A	57.95715	57.95729	57.95743E	57.85436	57.95769
A_D	-4.233427E-05	-4.210203E-05	-4.188010E-05	-4.140861E-05	-4.146190E-05
λ	-0.5148741	-0.5148780E	-0.5148817	-0.5123320	-0.5148887
λ_D	-4.436041E-06	-4.411936E-06	-4.388900E-06	-4.174799E-06	-4.345486E-06

Note: The complete set of calculated spectroscopic constants are provided in supplementary tables in Appendix B.

calculated values in Tables 13-15 and the supplementary files (Appendix B), and the $v = 0$ $A^3\Phi$ constants were fitted. Updated $A^3\Phi$ spectroscopic constants for $v = 0$ derived from the PGOPHER rotational analysis are shown in Table 17. A line list was calculated for all the isotopologues for the 0-0, 0-1, 0-2, 0-3 The line list table is available with a separate table for each isotopologue, in total containing 183212 lines.

The equilibrium vibrational and rotational constants (Tables 13-15) were also input into LeRoy's Rydberg-Klein-Rees (RKR) program [20] to generate potential energy curves for the A and X states of all isotopologues. The potential energy curves, along with the transition dipole moment for the $A^3\Phi$ - $X^3\Delta$ transition, obtained from McKemmish et al. [12] Figure 4 and equation (4) were then input into LeRoy's LEVEL program [21], which generated transition-dipole moment matrix elements, shown in Table 18."[111]

10.3 DISCUSSION

"The $X^3\Delta$ constants used in our analysis were calculated using the isotopic relationships. The reliability of these constants can be assessed by comparison with recent independent measurements. Lincowski et al. [117] published B, D, A_D and λ_D spectroscopic constants for the $X^3\Delta$ $v = 0$ state for all four minor isotopologues from pure rotational transitions.

TABLE 17: Spectroscopic constants for the $v = 0$ $A^3\Phi$ state of the minor isotopologues of TiO in cm^{-1} obtained from rotational analysis[111].

	$^{46}Ti^{16}O$	$^{47}Ti^{16}O$	$^{48}Ti^{16}O$	$^{49}Ti^{16}O$	$^{50}Ti^{16}O$
T	14092.47573(73)	14092.70196(74)	14092.905684(193)	14093.10467(74)	14093.29833(76)
B	0.5112005(16)	0.5083876(16)	0.505716075(244)	0.5031484(16)	0.5006448(16)
D	7.1031(80)E-7	6.9804(80)E-7	6.937508(942)E-7	6.9349(80)E-7	6.6164(81)E-7
H	3.9(11)E-13	-1.5(11)E-13	8.25(102)E-14	9.9(11)E-13	-2.96(11)E-12
A	57.95700(18)	57.95680(16)	57.9573454(742)	57.95792(18)	57.96225(19)
A_D	-4.2117(79)E-5	-4.1542(79)E-5	-4.18140(290)E-5	-4.1320(80)E-5	-4.2521(81)E-5
λ	-0.51486(49)	-0.51359(49)	-0.515184(168)	-0.51472(49)	-0.51313(50)
λ_D	-5.32(23)E-6	-5.31(23)E-6	-4.2199(692)E-6	-5.67(23)E-6	-7.17(23)E-6

Note: The major isotopologue $^{48}Ti^{16}O$ constants are from Ram et al. [94] and included for reference. Terms in parentheses are 1 standard deviation.

TABLE 18: Transition-dipole Moment Matrix Elements for TiO $A^3\Phi$ - $X^3\Delta$ Transition [111].

Band	Transition-dipole Moment Matrix Element (debye)				
v' – v"	$^{46}Ti^{16}O$	$^{47}Ti^{16}O$	$^{48}Ti^{16}O$	$^{49}Ti^{16}O$	$^{50}Ti^{16}O$
0-0	2.07264	2.07149	2.07091	2.07053	2.06635
0-1	1.02271	1.02440	1.02546	1.02628	1.03152
0-2	3.56732E-1	3.58126E-1	3.59009E-1	3.59710E-1	3.62588E-1
0-3	9.71877E-2	9.78218E-2	9.82541E-2	9.86166E-2	1.00568E-1
0-4	2.16345E-2	2.17894E-2	2.19642E-2	2.21422E-2	2.28013E-2

The published constants were based on about 10 submillimeter lines for each isotopologue. The two sets of constants are shown for comparison in Table 19.

In addition, Breier et al. [118] conducted a mass-independent analysis of the isotopologues of TiO, recording over 130 pure rotational transitions in the $X^3\Delta$ state in the mm wave region (below 20 cm^{-1}) using a laser ablation source. That work was followed by Witsch et al. [104] also using a laser ablation source to record rovibrational lines in the $X^3\Delta$ state around 1000 cm^{-1}). Both papers published mass-independent constants for the TiO $X^3\Delta$ state. Those constants were converted to Dunham parameters using equation (1) in Breier et al. [118]. A comparison of the equilibrium constants extracted from those two papers with the calculated $X^3\Delta$ state equilibrium constants used in this work are shown in Table 20 with satisfactory agreement.

A comparison was also made between the line list produced by this research and the ExoMol TiO line list [12]. A section of the spectrum was chosen between 14145 and 14169 cm^{-1}. That region of the spectrum contains the 0-0 band of the $A^3\Phi$ - $X^3\Delta$ transition and includes lines from all four minor isotopologues, predominantly R and Q branch lines, with J ranging from 11 to 45. 71 lines were compared with an average difference of 0.015 cm^{-1}."[111]

10.4 CONCLUSION

"A new line list for the TiO minor isotopologues for the $A^3\Phi$ - $X^3\Delta$ transition has been produced from the TiO emission spectrum recorded in 1985 at the McMath-Pierce Solar Telescope. The list strengthens current TiO line lists and has also produced spectroscopic constants for all four minor isotopologues in the $v = 0$ $A^3\Phi$ state. The isotopologue line lists for $v' = 0$ and $v'' = 0 - 4$ are available as supplemental files." [111]

TABLE 19: Calculated TiO $X^3\Delta$ $v = 0$ state spectroscopic constants compared with Lincowski et al. [111, 117] in cm^{-1}.

	Calculated	Lincowski et al.
$^{46}Ti^{16}O$		
B	0.5396110	0.539608942(21)
D	6.172487E-07	6.17727E-07(56)
A_D	-2.675451E-05	-2.73022E-05(47)
λ_D	6.797033E-07	6.288E-07(83)
$^{47}Ti^{16}O$		
B	0.5366503	0.536649311(22)
D	6.104796E-07	6.10686E-07(63)
A_D	-2.660597E-05	-2.68983E-05(57)
λ_D	6.759687E-07	7.23E-07(26)
$^{49}Ti^{16}O$		
B	0.5310972	0.531098327(19)
D	5.978842E-07	5.98301E-07(32)
A_D	-2.632742E-05	-2.61548E-05(47)
λ_D	6.689640E-07	6.32E-07(11)
$^{50}Ti^{16}O$		
B	0.5284900	0.528492094(24)
D	5.920160E-07	5.92513(60)E-07
A_D	-2.619665E-05	-2.58065(53)E-05
λ_D	6.656753E-07	6.104(97)E-07

Note: Numbers in parentheses are 1 standard deviation.

TABLE 20: Comparison of equilibrium constants for the TiO $X^3\Delta$ state (cm^{-1})[111].

	Breier et al. (2019)	Witsch et al. (2021)	Calculated (this work)
$^{46}Ti^{16}O$			
ω_e (Y_{10})	1014.641593	1014.639822	1014.642261
$\omega_e x_e$ ($-Y_{20}$)	4.610977103	4.610454558	4.611283418
B_e (Y_{01})	0.541314542	0.54131547	0.541149932
α_e ($-Y_{11}$)	0.003072747	0.003072671	0.003073155
γ_e (Y_{21})	-9.56609E-06	-9.47517E-06	-9.4132E-06
$^{47}Ti^{16}O$			
ω_e (Y_{10})	1011.850278	1011.848511	1011.850943
$\omega_e x_e$ ($-Y_{20}$)	4.585642071	4.585122397	4.585946703
B_e (Y_{01})	0.538340288	0.53834121	0.538176582
α_e ($-Y_{11}$)	3.04745722E-03	3.04738199E-03	3.04786210E-03
γ_e (Y_{21})	-9.46126E-06	-9.37133E-06	-9.31004E-06
$^{48}Ti^{16}O$			
ω_e (Y_{10})	1009.1758	1009.174038	1009.176464
$\omega_e x_e$ ($-Y_{20}$)	4.561432976	4.560916046	4.561736
B_e (Y_{01})	0.535498214	0.535499131	0.535335373
α_e ($-Y_{11}$)	3.02335632E-03	3.02328169E-03	3.02375800E-03
γ_e (Y_{21})	-9.36162E-06	-9.27264E-06	-9.2120E-06
$^{49}Ti^{16}O$			
ω_e (Y_{10})	1006.594041	1006.592284	1006.594703
$\omega_e x_e$ ($-Y_{20}$)	4.538123939	4.537609651	4.538425415
B_e (Y_{01})	0.532761805	0.532762717	0.532599796
α_e ($-Y_{11}$)	3.00021181E-03	3.00013775E-03	3.00061042E-03
γ_e (Y_{21})	-9.26619E-06	-9.17812E-06	-9.11809E-06
$^{50}Ti^{16}O$			
ω_e (Y_{10})	1004.116728	1004.114975	1004.117388
$\omega_e x_e$ ($-Y_{20}$)	4.515814015	4.515302255	4.516114009
B_e (Y_{01})	0.530142688	0.530143596	0.529981476
α_e ($-Y_{11}$)	2.97811496E-03	2.97804144E-03	2.97851063E-03
γ_e (Y_{21})	-9.17531E-06	-9.0881E-06	-9.02866E-06

Note: The equivalent Dunham parameter symbol is shown in parentheses next to the equilibrium constant symbol in the first column.

CHAPTER 11

ABSORPTION CROSS SECTIONS OF CYCLOHEXANE

The findings and the material presented in this section are published in the Journal of Quantitative Spectroscopy and Radiative Transfer [119]. All the authors are from Old Dominion University. Jason Sorensen was a post doctoral researcher at the time of publication and is the corresponding author; he wrote the introduction and conclusion, supervised the spectrometer data collection done by the PhD candidate coauthors, and coordinated our joint writing efforts into one document. Peter Bernath is a coauthor and project advisor, he also edited the paper. The remaining authors, Ryan Johnson, Randika Dodangodage, Keith Labelle and I either are or were PhD candidates on Peter Bernath's research team at the time of publication. Each of the graduate students researched a hydrocarbon molecule; in my case it was cyclohexane. I did the spectrometer experiments on cyclohexane under the watchful eye of Jason Sorensen, then followed up with spectral analysis and wrote the sections of the paper dealing with cyclohexane and generated the cyclohexane graphics. This work is original and was not published anywhere prior to publication in the Journal of Quantitative Spectroscopy and Radiative Transfer.

11.1 INTRODUCTION

Hydrocarbons are significant molecules both in the Earth's atmosphere and in the astronomical realm.

"The oxidation of non-methane hydrocarbons plays an important role in the production of tropospheric ozone and aerosols, with these hydrocarbons largely coming from fugitive emissions of fossil fuel production [120]. Simple hydrocarbons have also been observed in the atmospheres of the giant planets [121] and Saturn's moon Titan [122] which has an organic-rich atmosphere and is considered to be like that of pre-biotic Earth [123, 124]. Organic molecules are produced on Titan by dissociation and ionization of nitrogen and methane in the upper atmosphere. Reactions between two methyl radicals produce ethane and other photochemical processes form larger hydrocarbons. Organic photochemistry also produces an orange aerosol haze on Titan [122, 125]. The atmospheres of giant planets are likely reservoirs of complex hydrocarbon species.

Numerous non-methane hydrocarbons (C_2H_2, C_2H_4, C_2H_6, CH_3C_2H, C_3H_6, C_3H_8, C_4H_2 and C_6H_6) [122] have been detected in the stratosphere of Titan mainly using the CIRS (Composite Infrared Spectrometer) Fourier transform instrument on the Cassini spacecraft that was in orbit around Saturn. The most recent hydrocarbons detected on Titan are allene (propadiene, CH_2CCH_2) from TEXES (Texas Echelon-cross-Echelle Spectrograph) on the NASA IR Telescope Facility by Lombardo et al. [126] and cyclopropenylidene (c-C_3H_2) found with ALMA (Atacama Large Millimeter/submillimeter Array) by Nixon et al. [127]. Titan's stratosphere has a temperature of about 80 to 200 K at pressure of about 10 to 0.01 Torr of mainly nitrogen [122]. Hydrocarbon fractional abundances range from 0.2 ppb for benzene (C_6H_6) to a few percent for methane (CH_4). None of the hydrocarbons studied in this paper have been detected on Titan yet, although they are all potentially present.

The detection of hydrocarbon species in the Earth's atmosphere and the atmospheres of planets, moons and exoplanets relies on reliable spectroscopic line lists and cross sections. Most existing spectroscopic cross sections for hydrocarbon species were collected at relatively low resolution and are often broadened by N_2. Higher resolution spectroscopic cross sections that can resolve sharper spectroscopic features are necessary in order to identify and quantify these species under conditions where pressure broadening is small. Our present work includes absorption cross sections in the 3000 cm^{-1} (CH stretching) region for n-butane, n-pentane, cyclopentane and cyclohexane along with 1460 cm^{-1} (6.8 μm) cross sections for cyclopentane."[119]

11.2 CYCLOHEXANE

"Cyclohexane (C_6H_{12}) is a ring of 6 carbon atoms with multiple conformations. Of these, the "chair" is the minimum energy conformation with its 6 axial and 6 equatorial hydrogen atoms. Local minima occur in the "twist boat" conformation, about 5.5 kcal/mol higher than the "chair conformation" [129, 130]. Cyclohexane is almost completely in the chair conformation at room temperature, where less than 0.1% of the molecules are in the twist-boat conformation. Volatile organic compounds including cyclohexane are found in the Earth's atmosphere, produced by biogenic and anthropogenic means [131]. Hydrocarbons such as cyclohexane may also be found in the atmospheres of gas giant planets such as Saturn as well as its moon Titan where it is formed by organic photochemistry and ion chemistry [128, 132] .

The chair form of cyclohexane has D_{3d} symmetry, and the twist boat form has D_2 symmetry. There are 48 normal modes and 32 fundamental vibration frequencies, listed

here grouped by symmetry and using numbering of the vibrational modes from the order of irreducible representations in Herzberg's character tables: [133] $a_{1g}(v_1 - v_6)$, $a_{1u}(v_7 - v_9)$, $a_{2g}(v_{10} - v_{11})$, $a_{2u}(v_{12} - v_{16})$, $e_g(v_{17} - v_{24})$ and $e_u(v_{25} - v_{32})$. Only the 3 a_{1u} and 8 e_u modes are infrared active [134]. The a_{1g} and e_g modes are Raman active. There have been many previous efforts to make infrared and Raman measurements of cyclohexane in its different phases with accompanying calculations to assist with vibrational assignments [135, 136, 137, 138, 139, 140, 141]. This work builds on the previous investigation into the high-resolution infrared spectra of cyclohexane published by Bernath and Sibert [142]."[119]

11.3 METHOD AND RESULTS

"All spectra were recorded with a Bruker IFS 120/125HR Fourier transform spectrometer at a resolution of 0.04 cm^{-1}. An internal glowbar source, KBr beamsplitter and a liquid N_2 cooled InSb detector were used in the setup (liquid N_2 cooled HgCdTe detector for the 1460 cm^{-1} band of cyclopentane). Samples of each molecular gas were prepared in a single pass 20 cm cell fitted with wedged CaF_2 windows. For the low temperature spectra, the cell was cooled with a liquid ethanol circulator. Table 21 displays the number of sample and background scans averaged for each molecule at the given temperature and pressure."[119]

Fig. 51 shows the CH stretch cross sections of cyclohexane between 2840 and 2980 cm^{-1}, collected at the temperatures 294.2 K and 221.6 K, as shown in Table 21. Fig 52 shows P, Q and R rotatonal structure for the v_{13} a_{2u} mode at 2861.51 cm^{-1} and the v_{26} e_u mode at 2862.28 cm^{-1}, measured at temperature 221.6 K [142]. The recorded spectra are included in the paper's supplemental data section as data point files.

11.4 CALIBRATION

"All spectra were wavenumber calibrated using CO_2 lines between 2323 and 2348 cm^{-1} from the HITRAN database [143]. The frequency correction factors are included in Table 21 along with their standard deviations. These correction factors do not have associated intercepts and resulted in an average shift in frequency in the 3.3 μm region of less than 0.01 cm^{-1} and a shift of 0.005 cm^{-1} in the 6.8 μm region for cyclopentane. As we had some difficulty obtaining accurate pressure measurements, all cross sections reported in this work had the area under their respective cross section calibrated to match the area under similar, lower resolution, spectra obtained by Pacific Northwest National Laboratory (PNNL) [144]. Table 22 shows the integrated areas of the PNNL data (at 296 K) along with the integration bounds used for each case.

TABLE 21: Molecule specific experimental parameters [119].

Molecule	Scans	Press (Torr)	Temp (k)	Freq. Corr. Factor
n-butane	512	2.047	294.2	0.999995689(16)
	512	2.560	230.5	0.999995727(14)
n-pentane	640	0.385	294.2	0.999999760(38)
	640	2.191	217.6	0.999998534(23)
Cyclopentane (3000 cm^{-1})	640	0.431	296.2	0.999995727(14)
	640	0.198	235.2	0.999995684(24)
Cyclopentane (1460 cm^{-1})	640	27.89	294.2	0.999994088(87)
	640	18.15	235.8	0.999994041(23)
Cyclohexane	640	1.06	294.2	0.999998539(25)
	640	0.87	221.6	0.999996739(21)

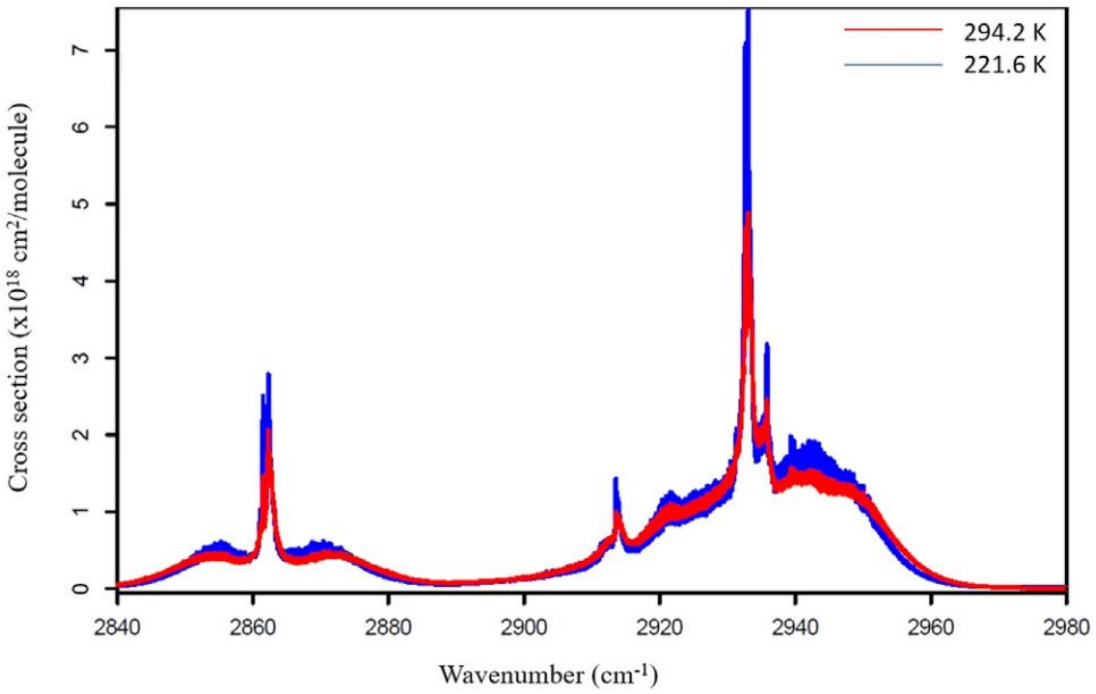

FIG. 51: Cross-section of pure cyclohexane C-H stretching region, blue plot is 221.6 K; red plot is 294.2 K [119].

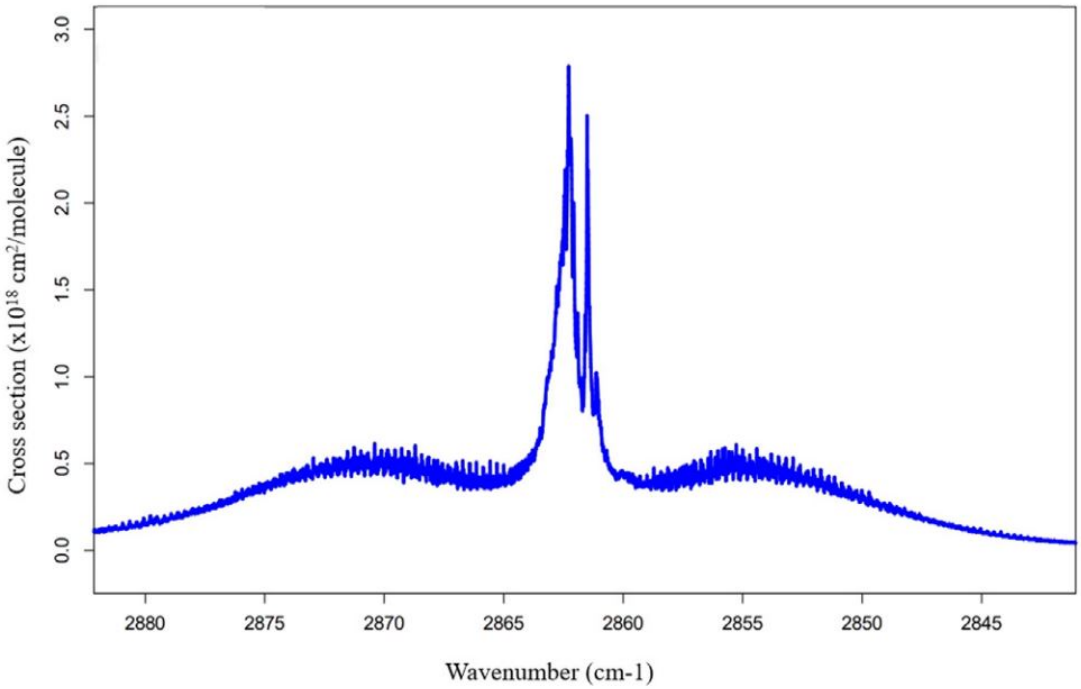

FIG. 52: P, Q, and R branches of cyclohexane centered around 2862 cm^{-1}; prominently visible are the v_{13} a_{2u} mode at 2861.51 cm^{-1} and the v_{26} e_u mode at 2862.28 cm^{-1} at temperature 221.6 K [119].

TABLE 22: Limits of integration along with the area under the curve for cross sections obtained from PNNL [119].

Molecule	Integration Limits (cm^{-1})	Area (x 10^{-18} cm/molecule)
n-butane	2776.298 - 3042.959	49.900
n-pentane	2778.116 - 3050.899	60.318
Cyclopentane (3000 cm^{-1})	2768.910 - 3062.819	57.843
Cyclopentane (1460 cm^{-1})	1350.561 - 1610.255	1.897
Cyclohexane	2833.759 - 2977.299	75.434

Note: The PNNL data was collected at 296K.

This correction assumes that the area under each cross section curve is independent of temperature as we have done in the past [143]. In addition, Grosch et al. [145] found that integrated cross sections of gaseous hydrocarbons do not change significantly with temperature. It is also worth noting that Grosch et al.'s cross section for n-butane also matched that of PNNL very closely [145].

The issue of reporting error in our cross sections is difficult and somewhat subjective. For the wavenumber calibration, the shift is on the order of 0.005-0.01 cm^{-1} as stated above, but after calibration the accuracy is 0.005 cm^{-1} or better based on the standard deviation of the calibration factor. The error in our cross sections comes from several sources including the PNNL data with an estimated error of $\leq$ 3% [144]. Our error cannot be lower than this. Based on previous experience [143], we estimate an error of about 5% for our cross sections."[119]

11.5 CONCLUSION

High resolution spectra of cyclohexane was collected at the temperatures 294.2 K and 221.6 K in the CH stretching region of about 3000 cm^{-1}. The spectra provide a significant improvement to previous cyclohexane spectra. The improved resolution will be useful in identifying the molecule in low pressure environments such as Saturn's moon Titan. The spectra collected for cyclohexane and the other molecular spectra collected in this research effort are available in the supplementary section of the published paper [119].

CHAPTER 12

CONCLUSIONS

Using satellite remote sensing data from the Atmospheric Chemistry Experiment (ACE) satellite, background SO_2 levels have been plotted by latitude and altitude from the tropopause up to an altitude of 24 km. In general, the SO_2 volume mixing ratio (VMR) is about 30 ppt near the tropopause, and then above an altitude of about 14 km the VMR falls off to about 10 ppt. The Northern and Southern Hemispheres differ in that the Northern Hemisphere background SO_2 VMR is about 5 to 10 ppt greater than the Southern Hemisphere in the upper troposphere in the latitude band from about 30° to the pole. Seasonal effects to background SO_2 levels have been observed in the polar and equatorial regions. Volcanic SO_2 plumes have been identified and confirmed through corroborating aerosol extinction also obtained from the ACE satellite. The volcanic SO_2 plumes have been shown to typically last in the stratosphere for about three months.

ACE satellite 1 μm imager data has been used to track sulfate aerosol extinction from the plume of the Hunga Tonga-Hunga Ha'apai volcano, which erupted in January 2022. The eruption was unique in terms of size of the plume and the amount of water injected into the stratosphere. This data analysis is part of a larger effort which led to determination of the composition of the aerosol in the plume in terms of weight percentage of sulfuric acid through derivation of an empirical formula.

The ACE database was probed for NO_2 and HNO_3 in the form of the major ^{14}N isotopologue and the minor ^{15}N isotopologue with VMR sorted by latitude and altitude. Combining these data and determining seasonal trends to the atmospheric fractionation δ value and applying known reaction and photolysis trends has led to a better understanding of the fractionation patterns within the significant stratospheric NO_x cycle.

Three electronic transitions of the astronomically prominent TiO molecule have been analyzed through rotational analysis of laboratory data, improving previous line lists and spectroscopic constants, directly applicable for stellar and exoplanet spectroscoppy. The spectroscopic constants determined and lines fitted for the $E^3\Pi$ - $X^3\Delta$ 0-0 band extend the previous efforts from a maximum J value of about 30 to higher values of about 60. Five higher order spectroscopic constants were determined (H, o_D, p_D, A_H and λ_D). Rotational analysis of the $B^3\Pi$ - $X^3\Delta$ electronic transition resulted in new spectroscopic constants for

$v' = 0 - 2$ in the B state and updated line lists for $v' = 0 - 2$ and $v'' = 0 - 4$. Solid data already exists for the $A^3\Phi$ - $X^3\Delta$ transition, however, only calculated values existed for the four minor isotopologues ($^{46}Ti^{16}O$, $^{47}Ti^{16}O$, $^{49}Ti^{16}O$, $^{50}Ti^{16}O$). Using the main isotopologue data, spectroscopic constants were calculated for each of the four minor isotopologues and a rotational analysis was conducted using the same experimental data used in the E - X and B - X rotational analyses. New line lists for $v' = 0$ and $v'' = 0 - 4$ and spectroscopic constants for $v = 0$ of the A state for each of the minor isotopologues have been produced.

The spectrum of cyclohexane was recorded in Old Dominion University's Atmospheric Chemistry Lab using a Bruker IFS 120/125HR Fourier transform spectrometer. Spectra were collected at two different temperatures in the 3000 cm^{-1} C-H stretching region. Significant improvements in resolution were made to existing spectral data. The spectra were collected at low pressures, improving their usefulness in astronomy applications.

BIBLIOGRAPHY

[1] P. F. Bernath, *Spectra of Atoms and Molecules* (Oxford University Press, New York, 2020).

[2] A. Fowler, Proc. R. Soc. Lond. A **79** 509-518 (1907).

[3] W. W. Morgan and P. C. Keenan, Annu. Rev. Astron. Astrophys. **11** 29 (1973)

[4] S. K. Nugroho, H. Kawahara, K. Masuda, T. Hirano, T. Kotani, and A. Tajitsu, Astron. J. **154** 221 (2017)

[5] C. Chackerian Jr., D. Goorvitch, A. Benidar, R. Farrenq, G. Guelachvili, P. M. Martin, M. C. Abrams, S. P. Davis, J. Quant. Spectrosc. Radiat. Transfer **48**, 5/6, 667-673 (1992)

[6] A Nordmann, https://commons.wikimedia.org/w/index.php?curid=3106631 (2007)

[7] J. Brown and A. Carrington, *Rotational Spectra of Diatomic Molecules* (Cambridge University Press, Cambridge, 2003)

[8] J.H. Van Vleck and V.F. Weisskopf, Revs. Mod. Phys. **17**, 227 (1945)

[9] A. Ibrahim, Spectroscopic Study of Channel Spectra Phenomena in the Synchrotron-Based FTIR Spectrometer at the Canadian Light Source, PhD Thesis (2011)

[10] J.L. Dunham, Phys. Rev. **41** 721 (1932)

[11] T.C. Reuter, https://commons.wikimedia.org/w/index.php?curid=49416157 (2016)

[12] L.K. McKemmish, T. Masseron, H.J. Hoeijmakers, V. Pérez, S.L. Grimm, S.N. Yurchenko, J. Tennyson, Mon. Not. R. Astron. Soc. **488**, 2, 2836-2854 (2019)

[13] S.A. Brooke, P.F. Bernath, T.W. Schmidt, G.B. Bacskay, J. Quant. Spectrosc. Radiat. Transf., **124** 11-20, (2013)

[14] https://phys.libretexts.org/Bookshelves/University Physics/Book Fig 3.6.1(b) (2022)

[15] R. White, *Chromatography/Fourier Transform Infrared Spectroscopy and Its Applications* (Marcel Dekker Inc, New York, 1990)

[16] J.B. West, R.S. Bradford Jr., J.D. Eversole, C.R. Jones, Rev. Sci. Instrum. **46**, 2, 164-168 (1975)

[17] P. F. Bernath, Science, **254**, 665-670, (1991)

[18] Bruker OPUS spectroscopy software, https://www.bruker.com/en/products-and-solutions/infrared-and-raman/opus-spectroscopy-software.html

[19] Colin M. Western, J. Quant. Spectrosc. Radiat. Transf. **186**, 221-242 (2017)

[20] Robert J. Le Roy, J. Quant. Spectrosc. Radiat. Transf. **186**, 158-166 (2017)

[21] Robert J. Le Roy, J. Quant. Spectrosc. Radiat. Transf. **186**, 167-178 (2017)

[22] R.N. Zare, J. K. Cashion, UCRL-10881 (1963)

[23] R. N. Zare, UCRL-10925 (1963)

[24] R. N. Zare J. Chem. Phys. **40**, 1934 (1964)

[25] J. W. Cooley, Math. Comput. **15**, 363 (1961)

[26] J. Cashion, J. Chem. Phys. **39**, 1872 (1963)

[27] J.C. Farman, B.G. Gardiner, J.D. Shanklin, Nature **315**, 207-210 (1985)

[28] A. Epton, https:/ghsearth.weebly.com/atmosphere.html

[29] H. Bönisch, A. Engel, Th. Birner, P. Hoor, D.W. Tarasick, E.A. Ray, Atmos. Chem. Phys. **11**, 3937-3948 (2011)

[30] https://www.esa.int/ESA Multimedia/Images/2018/08/Nadir-viewing vs. limb-viewing

[31] P.F. Bernath, J. Quant. Spectrosc. Radiat. Transf. **186**, 3-16 (2017)

[32] P.F. Bernath *The Atmospheric Chemistry Experiment ACE at 10: A Solar Occultation Anthology* (A. DEEPAK Publishing, Hampton VA, 2013)

[33] W.D. Cameron, P. Bernath, C. Boone, J. Quant. Spectrosc. Radiat. Transf. **258**, 107341 (2021)

[34] L. Thomason, T. Peter, SPARC **Rep No 4**, xi-xii (2006)

[35] F. Riccobono, S. Schobesberger, C.E. Scott, J. Dommen, J.K. Ortega, L. Rondo et al., Science **344**, 717-721 (2014)

[36] W. Aas, A. Mortier, V. Bowersox, R. Cherian, G. Faluvegi, H. Fagerli et al., Sci. Rep. **9**, 953 (2019)

[37] A.W. Rollins, T.D. Thornberry, E. Atlas, M. Navarro, S. Schauffler, F. Moore et al., J. Geophys. Res. - Atm. **123(13)**, 549-559 (2018)

[38] Global Volcanism Program, E. Venzke (editor), Smithsonian Institution; 2013, downloaded 11 Sep 2019, https://doi.org/10.5479/si.GVP.VOTW4-2013 (2019)

[39] D. Stevenson, C. Johnson, W. Collins, R. Derwent, Geol. Soc. Sp. **213**, 295-305 (2003)

[40] C.R. Hoyle, C. Fuchs, E. Järvinen, H. Saathoff, A. Dias, I. El Haddad, et al., Atmos. Chem. Phys. **16**, 1693-1712 (2016)

[41] W.G. Read, L. Froidevaux, J.W. Waters, Geophys. Res. Lett. **20**, 1299-1302 (1993)

[42] T.F. Stocker, D. Qin, G.K. Plattner, M. Tignor, S.K. Allen, J. Boschung, et al. (editors), *Climate Change 2013: the physical science basis. IPCC 2013* (Cambridge Univ Press, Cambridge, UK and New York, NY 2013)

[43] V.E. Fioletov, C.A. McLinden, N. Krotkov, M.D. Moran, K. Yang, Geophys Res. Lett. **38**, L21811 (2011)

[44] S.A. Carn, V.E. Fioletov, C.A. McLinden, N. Krotkov, Sci. Rep. **7**, 44095 (2017)

[45] V.E. Fioletov, C.A. McLinden, D. Griffin, N. Theys, D. Loyola, P. Hedelt, et al., Atmos. Chem. Phys. **20**, 5591-5607 (2020)

[46] K. Yang, X. Liu, N.A. Krotkov, A.J. Krueger, S.A. Carn, Geophys. Res. Lett. **36**, L10803 (2009)

[47] H.C. Pumphrey, W.G. Read, N.J. Livesy, K. Yang, Atmos. Meas. Tech. **8**, 195-209 (2015)

[48] M. Höpfner, C. Boone, B. Funke, N. Glatthor, U. Grabowski, A. Günther et al., Atmos. Chem. Phys. **12**, 7017-7037 (2015)

[49] ACE-FTS data, version 4.0, http://database.scisat.ca/level2/ace_v4.0 (2019)

[50] I.E. Gordon, L.S. Rothman, C. Hill, R.V. Kochanov, Y. Tan, P.F. Bernath et al., J. Quant. Spectrosc. Radiat. Transf. **203**, 3-69 (2017)

[51] S. Kremser, L.W. Thomason, M. von Hobe, M. Herrman, T. Deschler, C. Timmreck et al., Rev. Geophys. **54**, 278-335 (2016)

[52] A.W. Rollins, T.D. Thornberry, L.A. Watts, P. Yu, K.H. Rosenlof, M Mills et al., Geophys. Res. Lett. **44**, 4280-4286 (2017)

[53] S.A. McKeen, S.C. Liu, C.S. Kiang, J. Geophys. Res. **89**, 4873-4881 (1984)

[54] P. Bernath, C. Boone, A. Pastorek, D. Cameron, M. Lecours, J. Quant. Spectrosc. Radiat. Transf. **299**, 108520 (2023)

[55] J.F. Gleason et al., Science **260**, 523-526 (1993)

[56] A. Robock, Rev. Geophys. **38**, 191-219 (2000)

[57] G.G. Persad, B.H. Samset, L.J. Wilcox, Nature **611**, 662-664 (2022)

[58] J.L. Carr, K. Horváth, D.L. Wu, M.D. Friberg, Geophys. Res. Lett **49**, e2022GL098131 (2022)

[59] S.R. Proud, A. Prata, S. Schmauss, Science **378**, 554-557 (2022)

[60] L. Millán et al., Geophys. Res. Lett. **49**, e2022GL099381 (2022)

[61] H. Vömel, S. Evan, M. Tully, Science **377**, 1444-1447 (2022)

[62] M.R. Schoeberl, Y. Wang, R. Ueyama, G. Taha, E. Jensen, W. Yu, Geophys. Res. Lett. **49**, e2022GL100248 (2022)

[63] L. Coy, P. Newman, K. Wargan, G. Partyka, S. Strahan, S. Pawson, Geophys. Res. Lett. **49**, e2022GL100982 (2022)

[64] Y. Zhu et al., Commun. Earth Environ. **3**, 248 (2022)

[65] G. Taha, R. Loughman, P.R. Colarco, T. Zhu, L.W. Thomason, G. Jaross, Geophys. Res. Lett. **49**, e2022GL100091 (2022)

[66] A. Lacis, J. Hansen, M. Sato, Geophys. Res. Lett. **19**, 1607-1610 (1992)

[67] C.D. Boone, P.F. Bernath, K. Labelle, J. Crouse, J. Geophys. Res. **127**, e2022JD036600 (2022)

[68] K.F. Palmer, D. Williams, Appl. Opt. **14**, 208-219 (1975)

[69] M.J. Lecours, P.F. Bernath, J.J. Sorensen, C.D. Boone, R.M. Johnson, K. Labelle, J. Quant. Spectrosc. Radiat. Transf. **292**, 108361 (2022)

[70] C.D. Boone, P.F. Bernath, D. Cok, J. Steffen, S.C. Jones, J. Quant. Spectrosc. Radiat. Transf. **247**, 106939 (2020)

[71] P.F. Bernath, J. Steffen, J. Crouse, C.D. Boone, J. Quant. Spectrosc. Radiat. Transf. **253**, 107178 (2020)

[72] M. Lecours, P. Bernath, C. Boone, J. Crouse, J. Quant. Spectrosc. Radiat. Transf. **294**, 108406 (2023)

[73] C.E. Lund Myhre, D.H. Christensen, F.M. Nicolaisen, C.J. Nielsen, J. Phys. Chem. A. **107**, 1979-1991 (2003)

[74] K.S. Carslaw, L. Simon, S.L. Clegg, P. Brimblecombe, J. Phys. Chem. **99**, 11557-11574 (1995)

[75] H.M. Steele, P. Hamill, J. Aerosol Sci. **12**, 517-528 (1981)

[76] D.J. Jacob, *Introduction to Atmospheric Chemistry* (Princeton University Press, Princeton NJ, 1999).

[77] J. Li, X. Zhang, J. Orlando, G. Tyndall, G. Michalski, Atmos. Chem. Phys. **20**, 9805-9819 (2020)

[78] G.M. Begun, W.H. Fletcher, J. Chem. Phys. **25**, 1292-1293 (1956)

[79] E.U. Monse, W. Spindel, M.J. Stern, *Analysis of isotope-effect calculations illustrated with exchange equilibria among oxynitrogen compounds* (Rutgers Univ., Newark NJ, 1969)

[80] P. Bernath, W.D. Cameron, Astrophys. J. **904**, 24 (2020)

[81] W.D. Cameron, Unpublished dissertation intro paper from PhD Oral Exam (2021)

[82] J.J. Bochanski, A.A. West, S.L. Hawley, K.R. Covey, Astron. J. **133**, 151 (2007)

[83] T. Kamiński, H.S.P. Müeller, M.R. Schmidt, et al., Astron. Astrophys. **599**, A59, (2017)

[84] T.M. Evans, D.K. Sing, H.R. Wakeford, et al., Astrophys. J. Lett. **822**, L4 (2016)

[85] L.K. McKemmish, T. Masseron, S. Sheppard, et al., Astrophys. J. Supp. **228**, 15 (2017)

[86] C. Lundevall, J. Mol. Spectrosc. **191**, 93 (1998)

[87] J.T. Rayner, M.C. Cushing, W.D. Vacca, Astophys. J. Supp. **185**, 289 (2009)

[88] N.S. McIntyre, K.R. Thompson, W. Weltner Jr, J. Phys. Chem. **75**, 3243 (1971)

[89] C. Linton, H.P. Broida, J. Mol. Spectrosc. **64**, 382 (1977)

[90] B. Simard, P.A. Hackett, J. Mol. Spectrosc. **148**, 128 (1991)

[91] T.C. Steimle, W. Virgo, Chem. Phys. Lett. **381**, 30 (2003)

[92] K. Kobayashi, G.E. Hall, J.T. Muckerman, T.J. Sears, A.J. Merer, J. Mol. Spectrosc. **212**, 133 (2002)

[93] P.F. Bernath, Astrophys. J. **895**, 87 (2020)

[94] R.S. Ram, P.F. Bernath, M. Dulick, L. Wallace, Astrophys. J. Supp. **122**, 331 (1999)

[95] S.N. Yurchenko, L. Lodi, J. Tennyson, A.V. Stolyarov, Comp. Phys. Comm. **202**, 262 (2016)

[96] K.L. Luhman, J.R. Stauffer, A.A. Muench, et al., Astrophys. J. **593**, 1093 (2003)

[97] W.D. Cameron, P. Bernath, Astrophys. J. **926**, 39 (2022)

[98] L.A. Hillenbrand, G.R. Knapp, D.L. Padgett, L.M. Rebull, P.M. McGehee, Astron. J. **143**, 37 (2012)

[99] T. Kaminski, C. Gottlieb, K. Menten, et al., Astron. & Astrophys. **551**, A113 (2013)

[100] D.M. Bittner, P.F. Bernath, Astrophys. J. Supp. **236**, 46 (2018)

[101] J.N. Hodges, P.F. Bernath, Astrophys. J. **863**, 36 (2018)

[102] W.H. Hocking, M. Gerry, A. Merer, Canadian J. Phys. **57**, 54 (1979)

[103] C. Amiot, E.M. Azaroual, P. Luc, R. Vetter, J. Chem. Phys. **102**, 4375 (1995)

[104] D. Witsch, A.A. Breier, E. Döring, et al., J. Molec. Spectrosc. **377**, 111439 (2021)

[105] C. Amiot, P. Luc, R. Vetter, J. Molec. Spectrosc. **214**, 196 (2002)

[106] T. Steimle, J. Shirley, K. Jung, L. Russon, C. Scurlock, J. Molec. Spectrosc. **144**, 27 (1990)

[107] K.I. Namiki, S. Saito, J.S. Robinson, T.C. Steimle, J. Molec. Spectrosc. **191**, 176 (1998)

[108] J. Meija, T.B. Coplen, M. Berglund, et al., Pure Appl. Chem. **88**, 265 (2016)

[109] S.R. Langhoff, Astrophys. J. **481**, 1007 (1997)

[110] I. Hedgecock, C. Naulin, M. Costes, Astron. Astrophys. **304**, 667 (1995)

[111] P. Bernath, D. Cameron, (draft paper submitted 16 Feb 2023) J. Quant. Spectrosc. Radiat. Transf.

[112] T. Danilovich, C.A. Gottlieb, L. Decin, A.M.S. Richards, et al. Astron.J. **904**, 110 (2020)

[113] G.L. Hughes, B.K. Gibson, L. Carigi, P. Sanchez-Blazquez, J.M. Chavez, D.L. Lambert, Mon. Not. R. Astron. Soc. **390**, 1710-1718 (2008)

[114] D.B. Serindag, I.A. Snellen, P. Molliere, Astron. Astrophys. **655**, A69 (2021)

[115] Y.V. Pavlenko, S.N. Yurchenko, L.K. McKemmish, J. Tennyson, Astron. Astrophys. **642**, A77 (2020)

[116] M. Barnes, A.J. Merer, G.F. Metha, J. Molec. Spectrosc. **180**, 437-440 (1996)

[117] A.P. Lincowski, D.T. Halfen, L.M. Ziurys, Astrophys. J. **833**, 9 (2016)

[118] A.A. Breier, B. Wassmuth, G.W. Fuchs, J. Gauss, T.F. Giessen, J. Molec. Spectrosc. **355**, 46-58 (2019)

[119] J.J. Sorensen, P.F. Bernath, R.M. Johnson, R. Dodangodage, W.D. Cameron, K. Labelle, J. Quant. Spectrosc. Radiat. Transf. **290**, 108284 (2022)

[120] D. Helmig, S. Rossabi, J. Hueber, P. Tans, S.A. Montzka, K. Masarie, et al., Nat. Geosci. **9**, 490-495b(2016)

[121] S. Guerlet, T. Fouchet, B. Bezard, A.A. Simon-Miller, F.M. Flasar, Icarus **203**, 214-232 (2009)

[122] S.M. Hörst, J. Geophys. Res. **122**, 432-482 (2017)

[123] M.G. Trainer, A.A. Pavlov, H.L. DeWitt, J.L. Jiminez, C.P. McKay, O.B. Toon, et al., Proc. Natl. Acad. Sci. **103**, 18035-18042 (2006)

[124] F. Raulin, F. Cerceau, M. Hakdaoui, A. Vargas, Orig. Life Evol. Biosph. **16**, 401 (1986)

[125] S.M. Mackenzie, S.P.D. Birch, S. Hörst, C. Sotin, E. Barth, J. M. Lora, et al., Planet. Sci. J. **2**, 112 (2021)

[126] N.A. Lombardo, C.A. Nixon, T.K. Greathouse, B. Bézard, A. Jolly, S. Vinatier, et al., Astophys. J. **881**, L33 (2019)

[127] C.A. Nixon, A.E. Thelen, M.A. Cordiner, Z. Kisiel, S.B. Charnley, E.M. Molter et al., Astron. J. **160**, 205 (2020)

[128] J.I. Moses, B. Bezard, E. Lellouch, G.R. Gladstone, H. Feuchtgruber, M. Allen, Icarus **143**, 244-298 (2000)

[129] M. Squillacote, R.S. Sheridan, O.L. Chapman, F.A.L. Anet, J. Am. Chem. Soc. **97**, 3244-3246 (1975)

[130] Y.K. Kang, H.S. Park, Chem. Phys. Lett **702** 82-89 (2018)

[131] J.A. de Gouw, A.M. Middlebrook, C. Warneke, P.D. Goldan, W.C. Kuster, J.M. Roberts, et al., Geophys. Res. D. Atmos. **110**, 1-22 (2002)

[132] M. Dobrijevic, J.C. Loison, K.M. Hickson, G. Gronoff, Icarus **268** 313-339 (2016)

[133] G. Herzberg, *Infrared and Raman Spectra of Polyatomic Molecules* (D. Van Nostrand Company, New York, 1945)

[134] K.B. Wilberg, A.A. Shrake, Spectrochim Acta Part A Mol. Spectrosc. **27**, 1139-1151 (1971)

[135] D.A. Dows, J. Mol. Spectrosc. **16**, 302-308 (1965)

[136] H. Takahashi, T. Shimonouchi, K. Kukushima, T. Miyazawa, J. Mol. Spectrosc. **13**, 43-56 (1964)

[137] K. B. Wilberg, V.A. Walters, W.P. Dailey, J. Am. Chem. Soc. **107**, 4860-4867 (1985)

[138] E. Matrai, P. Csaszar, G. Fogarasi, M. Gal, Spectrochim Acta Part A Mol. Spectrosc. **41**, 425-433 (1985)

[139] E. Matrai, M. Gal, G. Keresztury, Spectrochim Acta Part A Mol. Spectrosc. **46**, 29-32 (1990)

[140] J.R. Durig, C. Zheng, A.M. El Defrawy, R.M. Ward, T.K. Gounev, K. Ravindranath, et al., J. Raman. Spectrosc. **40**, 197-204 (2009)

[141] H.J. Chun, E.J. Ocola, J. Laane, J. Phys. Chem. A **120**, 7677-7780 (2016)

[142] P.F. Bernath, E.L. Sibert, J. Phys. Chem A **124**, 9991-10000 (2020)

[143] I.E. Gordon, L.S. Rothman, R.J. Hargreaves, R. Hashemi, E.V. Karlovets, F.M. Skinner, et al. J. Quant. Spectrosc. Radiat. Transf. **277**, 107949 (2022)

[144] S.W. Sharpe, T.J. Johnson, R.L. Sams, P.M. Chu, G.C. Rhoderick, P.A. Johnson, Appl. Spectrosc. **58**, 1452-1461 (2004)

[145] A. Grosch, V. Beushausen, H. Wackerbarth, O Thiele, T. Berg, Appl. Opt. **49**, 196-203 (2010)

APPENDIX A

SUPPLEMENTAL SO_2 VOLCANIC PLUME PLOTS

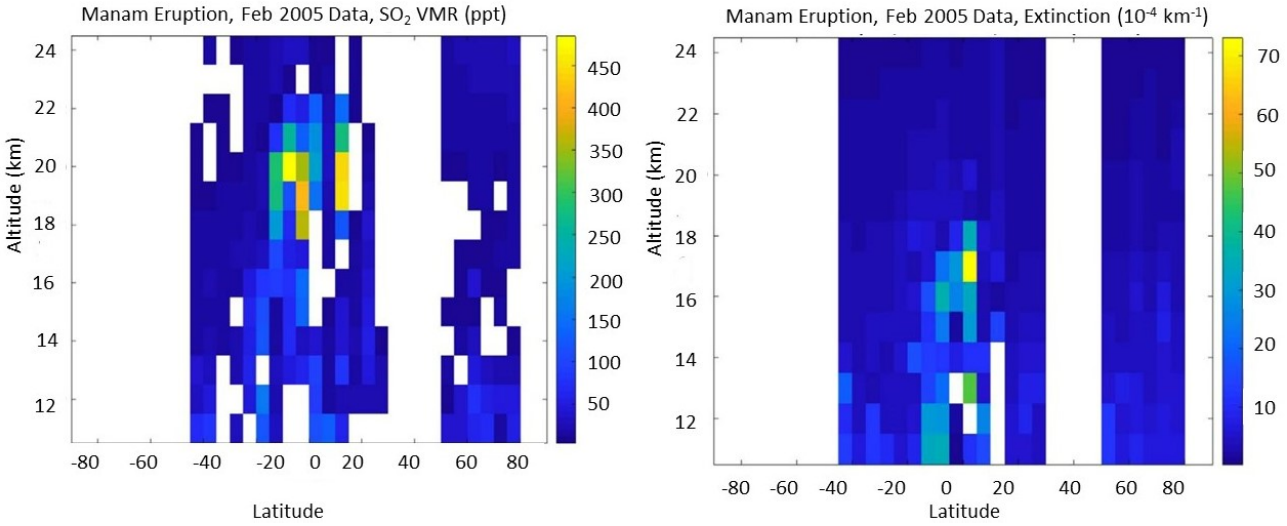

FIG. 53: Manam erupted on 27 Jan 2005 at 4.1°S, 145.0°E; Feb 2005 data shown [33]. Note: Left SO_2 VMR, right aerosol extinction.

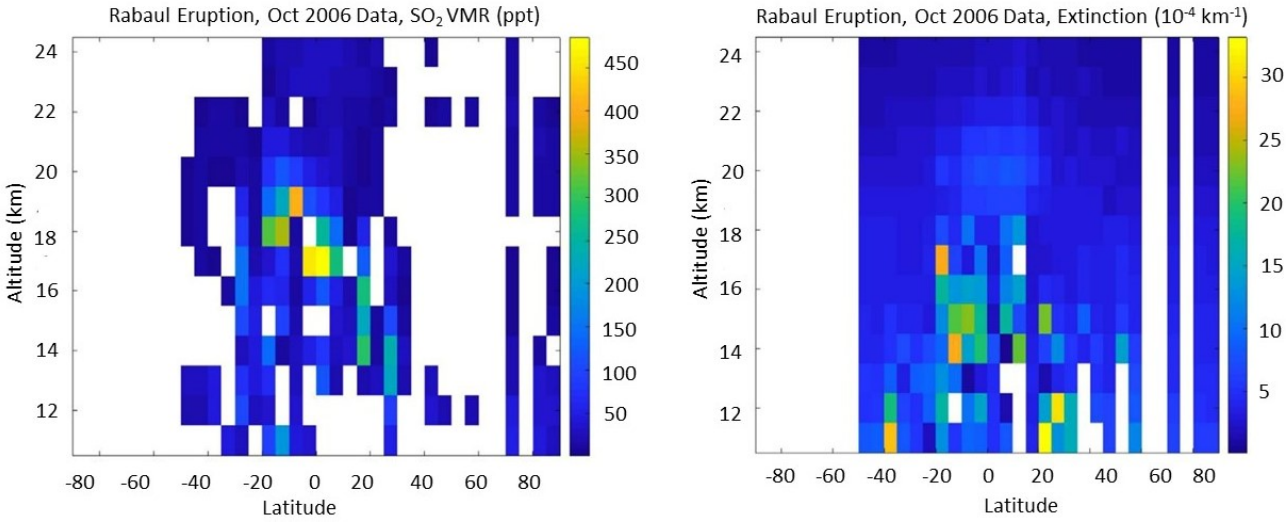

FIG. 54: Rabaul erupted on 7 Oct 2006 at 4.3°S, 152.2°E; Oct 2006 data shown [33]. Note: Left SO_2 VMR, right aerosol extinction.

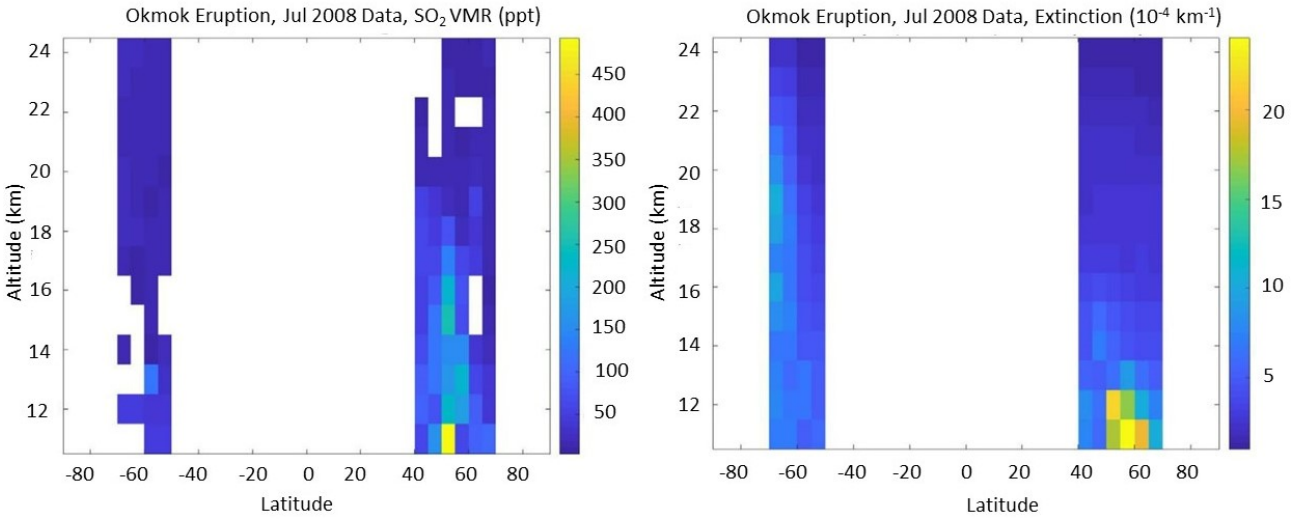

FIG. 55: Okmok erupted on 12 Jul 2008 at 53.4°N, 168.1°W; Jul 2008 data shown [33]. Note: Left SO_2 VMR, right aerosol extinction.

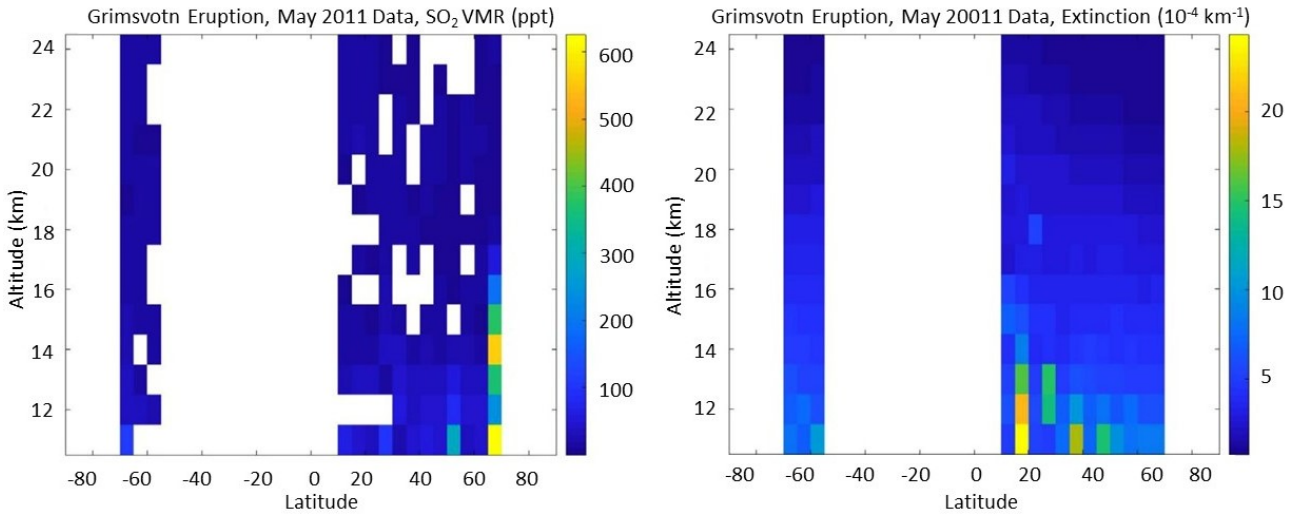

FIG. 56: Grimsvotn erupted on 21 May 2011 at 64.4°N, 17.3°W; May 2011 data shown [33]. Note: Left SO_2 VMR, right aerosol extinction.

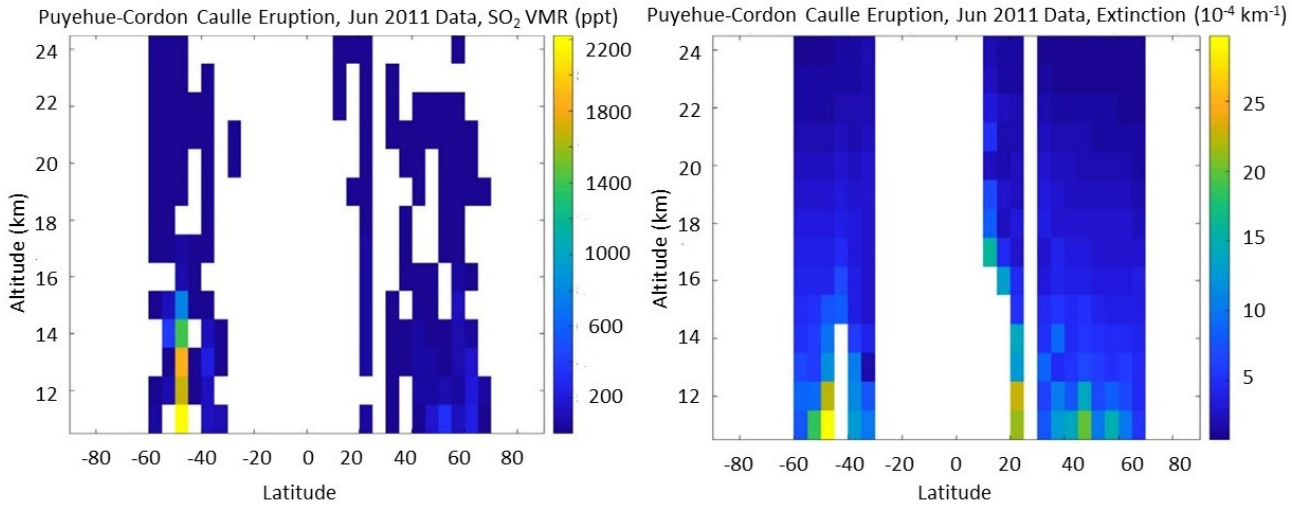

FIG. 57: Puyehue-Cordon Caulle erupted on 4 Jun 2011 at 40.6°S, 72.1°W; Jun 2011 data shown [33].
Note: Left SO_2 VMR, right aerosol extinction. Plume at 20°N is Nabro (Fig 58); partially visible plume in vicinity of 50°N is Grimsvotn (Fig 56).

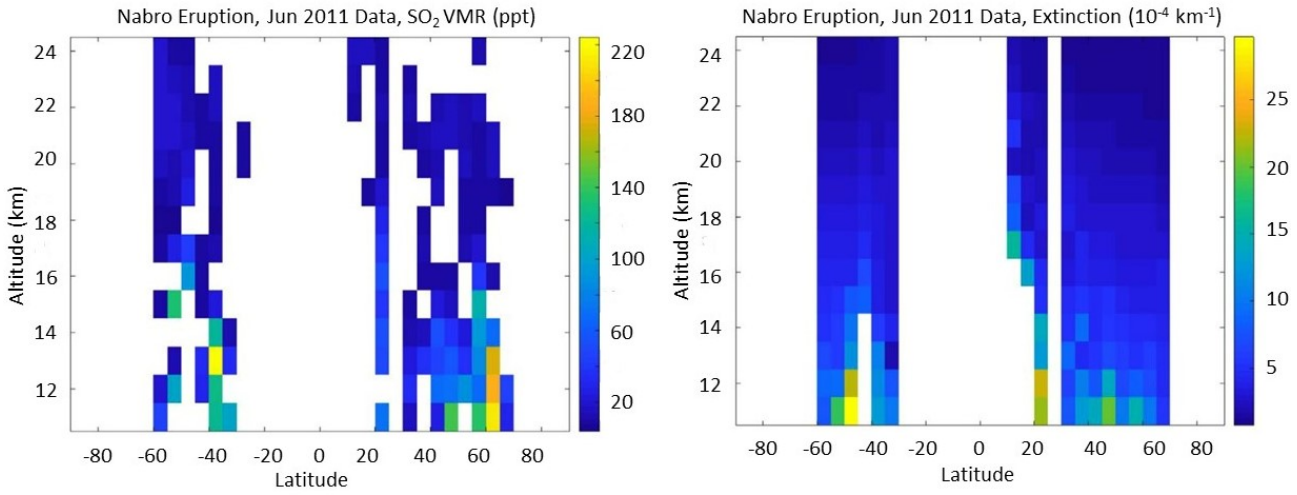

FIG. 58: Nabro erupted on 13 Jun 2011 at 13.4°N, 41.7°W; Jun 2011 data shown [33].
Note: Left SO_2 VMR, right aerosol extinction. The plume is somewhat obscured by Puyehue-Cordon Caulle (Fig 57) and the Grimsvotn eruption (Fig 56). SO_2 VMR data cells beyond 300 ppt have been removed to minimize masking from Puyehue-Cordon Caulle.

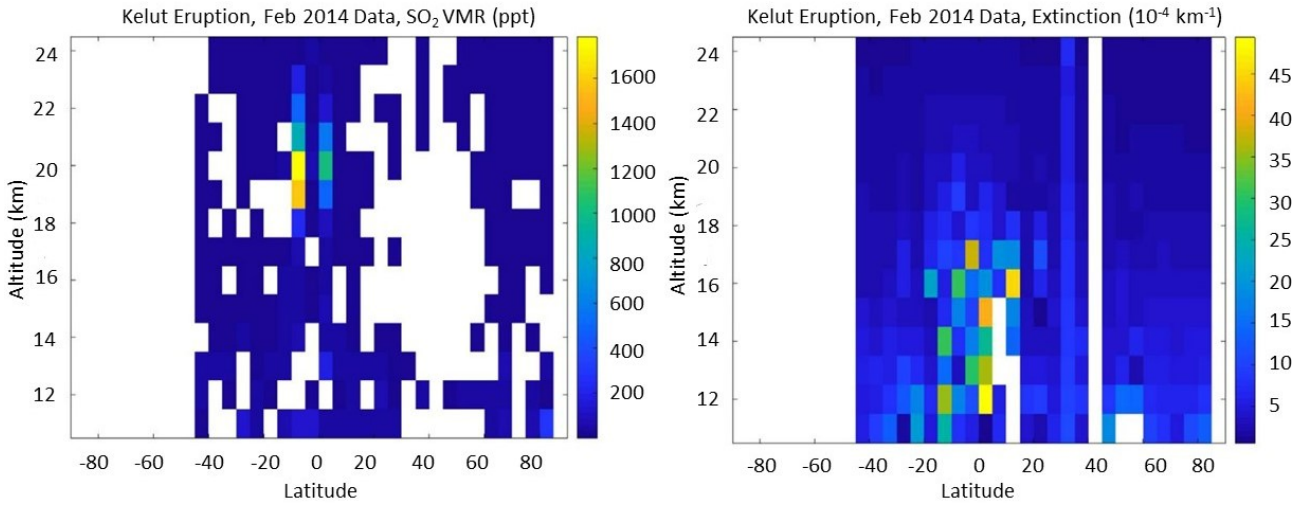

FIG. 59: Kelut erupted on 13 Feb 2014 at 7.9°S, 112.3°E; Feb 2014 data shown [33]. Note: Left SO_2 VMR, right aerosol extinction.

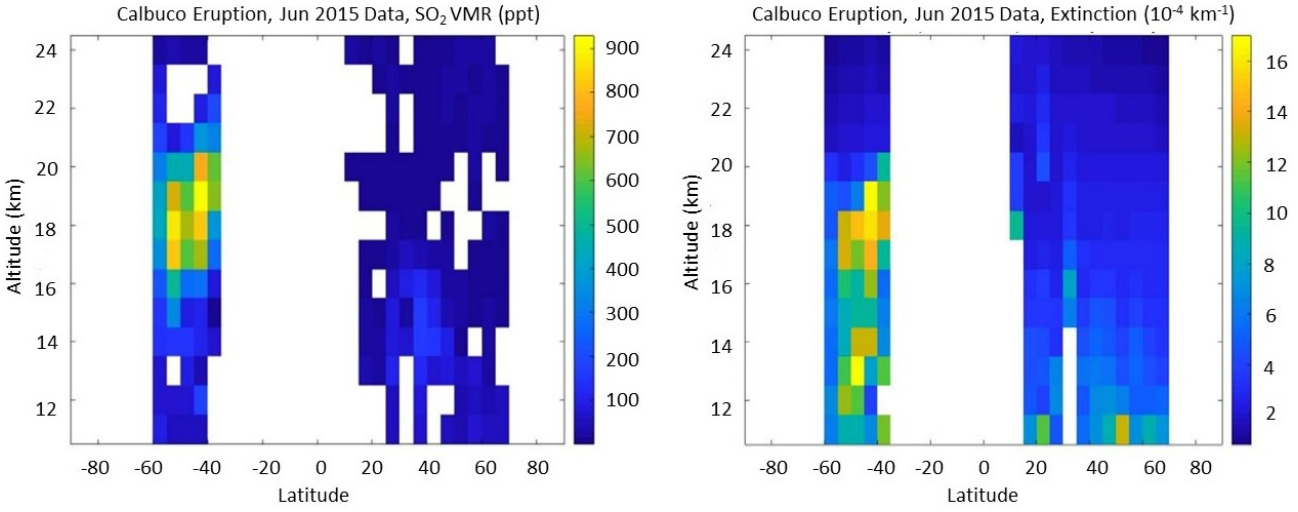

FIG. 60: Calbuco erupted on 22 Apr 2015 at 41.3°S, 72.6°W; Jun 2015 data shown [33]. Note: Left SO_2 VMR, right aerosol extinction.

APPENDIX B

CALCULATED TIO SPECTROSCOPIC CONSTANTS FOR $A^3\Phi$ AND $X^3\Delta$ STATES, $V = 0 - 4$

TABLE 23: Calculated spectroscopic constants in cm^{-1} for $A^3\Phi$ $v = 0 - 4$, $^{46}Ti^{16}O$ and $^{47}Ti^{16}O$. [111]

		$^{46}Ti^{16}O$			
P_v	v=0	v=1	v=2	v=3	v=4
Origin	14092.52421	13951.54364	13811.96293	13673.73372	13536.80768
B_v	0.5111999	0.5079686	0.5047224	0.5014591	0.4981767
D_v	7.089019E-07	7.103810E-07	7.122200E-07	7.144188E-07	7.169775E-07
H_v	1.180650E-13	1.180650E-13	1.180650E-13	1.180650E-13	1.180650E-13
A_v	57.957145	57.853141	57.751565	57.652417	57.555699
A_{Dv}	-4.233427E-05	-4.207023E-05	-4.180618E-05	-4.154214E-05	-4.127809E-05
λ_v	-0.5148741	-0.5123043	-0.5102333	-0.5086610	-0.5075876
λ_{Dv}	-4.436041E-06	-4.239481E-06	-4.042922E-06	-3.846362E-06	-3.649803E-06
		$^{47}Ti^{16}O$			
P_v	v=0	v=1	v=2	v=3	v=4
Origin	14092.71912	13952.12249	13812.91823	13675.05839	13538.49501
B_v	0.50839548	0.505190854	0.50197146	0.498735207	0.495480003
D_v	7.011314E-07	7.025893E-07	7.044011E-07	7.065670E-07	7.090868E-07
H_v	1.161296E-13	1.161296E-13	1.161296E-13	1.161296E-13	1.161296E-13
A_v	57.95729005	57.85356485	57.75225501	57.65336052	57.55688138
A_{Dv}	-4.210203E-05	-4.184016E-05	-4.157828E-05	-4.131641E-05	-4.105454E-05
λ_v	-0.514877958	-0.512313889	-0.510245838	-0.508673805	-0.507597791
λ_{Dv}	-4.411936E-06	-4.216994E-06	-4.022052E-06	-3.827111E-06	-3.632169E-06

TABLE 24: Calculated spectroscopic constants in cm^{-1} for $A^3\Phi$ $v = 0 - 4$, $^{48}Ti^{16}O$ and $^{49}Ti^{16}O$. [111]

		$^{48}Ti^{16}O$			
P_v	v=0	v=1	v=2	v=3	v=4
Origin	14092.90587	13952.67714	13813.83361	13676.32772	13540.11189
B_v	0.5057157	0.502536454	0.499342604	0.496132086	0.492902836
D_v	6.937463E-07	6.951841E-07	6.969703E-07	6.991049E-07	7.015879E-07
H_v	1.143000E-13	1.143000E-13	1.143000E-13	1.143000E-13	1.143000E-13
A_v	57.95742873	57.85397133	57.75291653	57.65426433	57.55801473
A_{Dv}	-4.188010E-05	-4.162030E-05	-4.136050E-05	-4.110070E-05	-4.084090E-05
λ_v	-0.514881675	-0.512323075	-0.510257875	-0.508686075	-0.507607675
λ_{Dv}	-4.388900E-06	-4.195500E-06	-4.002100E-06	-3.808700E-06	-3.615300E-06
		$^{49}Ti^{16}O$			
P_v	v=0	v=1	v=2	v=3	v=4
Origin	14093.08615	13953.21258	13814.71732	13677.55316	13541.67288
B_v	0.503135517	0.499980644	0.496811323	0.493625518	0.49042119
D_v	6.866726E-07	6.880913E-07	6.898530E-07	6.919578E-07	6.944057E-07
H_v	1.125567E-13	1.125567E-13	1.125567E-13	1.125567E-13	1.125567E-13
A_v	57.9575626	57.85436374	57.75355521	57.655137	57.55910911
A_{Dv}	-4.166642E-05	-4.140861E-05	-4.115080E-05	-4.089299E-05	-4.063518E-05
λ_v	-0.514885264	-0.51233195	-0.510269516	-0.50869796	-0.507617282
λ_{Dv}	-4.366719E-06	-4.174799E-06	-3.982880E-06	-3.790960E-06	-3.599041E-06

TABLE 25: Calculated spectroscopic constants in cm^{-1} for $A^3\Phi$ $v = 0 - 4$, $^{50}Ti^{16}O$. [111]

		$^{50}Ti^{16}O$			
P_v	v=0	v=1	v=2	v=3	v=4
Origin	14093.25914	14948.7994	15796.64562	16636.72858	17468.97906
B_v	0.500665902	0.497534298	0.494388396	0.491226182	0.488045646
D_v	6.799362E-07	6.813366E-07	6.830751E-07	6.851516E-07	6.875662E-07
H_v	1.109048E-13	1.109048E-13	1.109048E-13	1.109048E-13	1.109048E-13
A_v	57.95769106	57.85474032	57.75416815	57.65597454	57.56015951
A_{Dv}	-4.146190E-05	-4.120599E-05	-4.095008E-05	-4.069416E-05	-4.043825E-05
λ_v	-0.514888708	-0.512340474	-0.510280704	-0.508709401	-0.507626563
λ_{Dv}	-4.345486E-06	-4.154980E-06	-3.964475E-06	-3.773969E-06	-3.583463E-06

TABLE 26: Calculated spectroscopic constants in cm^{-1} for $X^3\Delta$ $v = 0 - 4$, $^{46}Ti^{16}O$ and $^{47}Ti^{16}O$. [111]

		$^{46}Ti^{16}O$			
P_v	v=0	v=1	v=2	v=3	v=4
B_v	0.5396110	0.5365190	0.5334082	0.5302786	0.5271301
D_v	6.172487E-07	6.208233E-07	6.244640E-07	6.281708E-07	6.319438E-07
H_v	7.106626E-14	7.106626E-14	7.106626E-14	7.106626E-14	7.106626E-14
A_v	50.651165	50.651339	50.649743	50.646376	50.641239
A_{Dv}	-2.675451E-05	-2.787441E-05	-2.899431E-05	-3.011421E-05	-3.123411E-05
λ_v	1.7472621	1.7424191	1.7381823	1.7345519	1.7315278
λ_{Dv}	6.797033E-07	6.797033E-07	6.797033E-07	6.797033E-07	6.797033E-07
		$^{47}Ti^{16}O$			
P_v	v=0	v=1	v=2	v=3	v=4
B_v	0.53665031	0.533583828	0.530498726	0.527395004	0.524272661
D_v	6.104796E-07	6.140051E-07	6.175957E-07	6.212512E-07	6.249718E-07
H_v	6.990126E-14	6.990126E-14	6.990126E-14	6.990126E-14	6.990126E-14
A_v	50.65116348	50.65134191	50.64975964	50.64641668	50.64131302
A_{Dv}	-2.660597E-05	-2.771666E-05	-2.882734E-05	-2.993802E-05	-3.104871E-05
λ_v	1.747269191	1.74243781	1.738209413	1.734583999	1.731561569
λ_{Dv}	6.759687E-07	6.759687E-07	6.759687E-07	6.759687E-07	6.759687E-07

TABLE 27: Calculated spectroscopic constants in cm^{-1} for $X^3\Delta$ $v = 0 - 4$, $^{48}Ti^{16}O$ and $^{49}Ti^{16}O$. [111]

		$^{48}Ti^{16}O$			
P_v	v=0	v=1	v=2	v=3	v=4
B_v	0.533821178	0.530778996	0.52771839	0.52463936	0.521541906
D_v	6.040462E-07	6.075252E-07	6.110682E-07	6.146752E-07	6.183462E-07
H_v	6.880000E-14	6.880000E-14	6.880000E-14	6.880000E-14	6.880000E-14
A_v	50.65116208	50.65134468	50.64977588	50.64645568	50.64138408
A_{Dv}	-2.646405E-05	-2.756595E-05	-2.866785E-05	-2.976975E-05	-3.087165E-05
λ_v	1.747275975	1.742455775	1.738235375	1.734614775	1.731593975
λ_{Dv}	6.724000E-07	6.724000E-07	6.724000E-07	6.724000E-07	6.724000E-07
		$^{49}Ti^{16}O$			
P_v	v=0	v=1	v=2	v=3	v=4
B_v	0.531097198	0.528078352	0.525041269	0.52198595	0.518912395
D_v	5.978842E-07	6.013188E-07	6.048164E-07	6.083770E-07	6.120006E-07
H_v	6.775067E-14	6.775067E-14	6.775067E-14	6.775067E-14	6.775067E-14
A_v	50.65116072	50.65134732	50.64979147	50.64649317	50.64145243
A_{Dv}	-2.632742E-05	-2.742088E-05	-2.851435E-05	-2.960781E-05	-3.070127E-05
λ_v	1.747282525	1.742473126	1.738260462	1.734644533	1.731625339
λ_{Dv}	6.689640E-07	6.689640E-07	6.689640E-07	6.689640E-07	6.689640E-07

TABLE 28: Calculated spectroscopic constants in cm^{-1} for $X^3\Delta$ $v = 0 - 4$, $^{50}Ti^{16}O$. [111]

		$^{50}Ti^{16}O$			
P_v	v=0	v=1	v=2	v=3	v=4
B_v	0.528490	0.525493382	0.522478757	0.519446075	0.516395335
D_v	5.920160E-07	5.954084E-07	5.988628E-07	6.023794E-07	6.059580E-07
H_v	6.675637E-14	6.675637E-14	6.675637E-14	6.675637E-14	6.675637E-14
A_v	50.65115942	50.65134984	50.64980637	50.64652903	50.64151779
A_{Dv}	-2.619665E-05	-2.728206E-05	-2.836747E-05	-2.945288E-05	-3.053829E-05
λ_v	1.747288811	1.742489783	1.738284556	1.734673132	1.731655508
λ_{Dv}	6.656753E-07	6.656753E-07	6.656753E-07	6.656753E-07	6.656753E-07

VITA

W. D. Cameron
Department of Physics
Old Dominion University
Norfolk, VA 23529

Education

BS Fire Protection Engineering, University of Maryland, 1984
MS Mechanical Engineering, University of South Alabama, 2000
MS Physics, Old Dominion University, 2020

Typeset using LaTeX.